DESIGN AND CHARACTERIZATION OF A HAND-HELD, WAVEGUIDE-MEDIATED, OPTOACOUSTIC IMAGING PROBE FOR ANALYZING BURN WOUNDS

A Thesis presented to

the Faculty of the Graduate School

at the University of Missouri

In Partial Fulfillment

of the Requirements for the Degree

Master of Science

---

by

MASON WILLIAM SCHELLENBERG

Heather K. Hunt, PhD., Thesis Supervisor

JULY 2018

Declaration of Approval

The undersigned, appointed by the Dean of the Graduate School, have examined the thesis entitled:

DESIGN AND CHARACTERIZATION OF A HANDHELD, WAVEGUIDE-MEDIATED PHOTOACOUSTIC IMAGING PROBE FOR IMAGING BURN WOUNDS

presented by Mason William Schellenberg,

a candidate for the degree of Master of Science in Bioengineering, and hereby certify that, in their opinion, it is worthy of acceptance.

_____

Dr. Heather K. Hunt

_____

Dr. Gang Yao

_____

Dr. Jeffrey Litt

Dedicated to my parents, who have shown me the value of pursuing passion.

Acknowledgements

First off, I would like to thank my parents, Mark and Cindy Schellenberg, for demonstrating to me the true value of pursing your passion. It was through the example that you set that I was able to push myself to be all that I can. I would also like to thank Madeline Best for her constant support and encouragement.

I also would like to thank Dr. Heather K. Hunt, my principle advisor, for providing a space that encouraged creativity and pushed me to be my absolute best. It was through this experience that I was able to find my passion for engineering. I must also thank Dr. Gang Yao and Dr. Jeffrey Litt, who have provided me with a wealth of support, encouragement, and much-needed advice. I should also thank Dr. Ping Yu. Without his help, this project could have gone astray.

I would like to thank my fellow students who helped me during my time with the Hunt Lab. First, Dr. Paul Whiteside, who guided me throughout my journey as an undergraduate researcher. Also, I would like to thank Jeff Chininis, Emma Bennett, Sharanya Kumar, Jonathan Baumstark, Amanda Sain, Courtney Gooch, Caio Peixoto de Sousa, Eduardo Torres, Phong Nguyen, and Quinn Duncan for the numerous ways, large and small, in which they have all assisted in the completion of this work.

Finally, I would like to thank Dr. Hsinyeh Hsieh and Dr. Chung-Ho Lin. Without their guidance, constant encouragement, and endlessly optimistic attitudes, I would not have become the researcher I am today.

Contents

List of Figures

List of Tables

Abbreviations

ANSI	American National Standards Institute
AR-OMi	Acoustic Resolution Optoacoustic Microscopy
AR-OR-OMi	Acoustic Resolution / Optical Resolution Optoacoustic Microscopy
CF	Coherence Factor
CNR	Contrast to Noise Ratio
CTC	Circulating Tumor Cell
DAS	Delay-and-Sum
DR-81	Direct-Red 81 Dye
FOV	Field of View
FPI	Fabry-Perot Interferometer
FWHM	Full-Width at Half-Max
GPU	Graphics Processing Unit
LED	Light Emitting Diode
LDI	Laser Doppler Imaging
MPE	Maximum Permissible Exposure
MSOM	Multispectral Optoacoustic Mesoscopy
MSOT	Multispectral Optoacoustic Tomography
Nd:YAG	Neodymium doped Yttrium Aluminum Garnet
NIR	Near Infrared
OA	Optoacoustic
OABC	Opto-Acoustic Beam Combiner

OACT	Optoacoustic Computed Tomography
OAI	Optoacoustic Imaging
OCT	Optical Coherence Tomography
OMe	Optoacoustic Mescoscopy
OMi	Optoacoustic Microscopy
OPO	Optical Parametric Oscillator
OR-OMi	Optical Resolution Optoacoustic Microscopy
PAI	Photoacoustic Imaging
PLD	Pulsed Laser Diode
PMMA	Poly(methyl methacrylate)
PSF	Point Spread Function
ROI	Region of Interest
RSOM	Raster-Scanning Optoacoustic Mesoscopy
SLN	Sentinel Lymph Node
SNR	Signal to Noise Ratio
TI	Thermal Imaging
UB	Ultra Broadband
US	Ultrasound
UV-VIS	Ultraviolet–Visible Spectroscopy
WM-OACT	Waveguide-Mediated Optoacoustic Computed Tomography

Biological Terminology

Deep burn	Burn wound extending into the subcutaneous tissue
Deep-partial burn	Burn wound extending into the lower dermis
Dermis	Inner layer of skin, made of connective tissue
Epidermis	Outer layer of skin tissue
Hemoglobin	Oxygen-carrying component found in red blood cells
Hyperperfusion	Increase of perfusion to levels above normal
Inflammation	Physiological response of the body to damage
Microvasculature	Smallest blood vessels in body, distribute blood to tissue
Perfusion	Blood flow within tissue
Subcutaneous tissue	Fatty tissue situated below the skin
Superficial burn	Burn wound extending into the epidermis
Superficial-partial burn	Burn wound extending into the upper dermis
Vasodilation	Dilation of blood vessels
Zone of coagulation	Volume of burn characterized by permanent tissue damage
Zone of hyperemia	Volume of burn characterized by inflammation
Zone of stasis	Volume of burn characterized by decreased blood flow

Symbols

λ_c	Wavelength of the high cut-off frequency of a transducer array	Hz
w	Width of sensor element in transducer array	m
d	Distance from center of curved of spherical array to resolved point	m
r	Radius of curved of spherical array	m
$R_{A,OACT}$	Axial resolution of a OACT platform	m
$R_{L,OACT}$	Lateral resolution of a transducer array, OACT	m
NA	Numerical aperture of a lens	dimensionless
f	Central frequency of the transducer array	Hz
c	Speed of sound	m/s
$R_{L,AR-OMi}$	Lateral resolution of a AR-OMi platform	m
$R_{A,OMi}$	Axial resolution of a OMi platform	m
λ	Optical wavelength	m
$\mathrm{R_{L,OR-OMi}}$	Lateral resolution of a OR-OMi platform	m
n	Refractive Index	dimensionless
θ_c	Critical Angle	°
F	Force	N
p	Pressure	Pa
x	Position, 1D	m
ρ	Density	kg/m^3

u	Velocity	m/s
t	Time	s
$\vec{r}$	Position, 3D	m
ξ	Displacement	m
V	Volume	m^3
κ	Isothermal Compressibility	Pa^{-1}
β	Thermal Coefficient of Volume Expansion	K^{-1}
T	Temperature	K
τ_{th}	Thermal Relaxation Time	s
d_c	Characteristic Dimension of a Heated Region	m
α_{th}	Thermal Diffusivity	m^2/s
τ_s	Stress Relaxation Time	s
C_V	Specific Heat Capacity at Constant Volume	J/(kg K)
η_{th}	Heat Conversion Ratio	dimensionless
μ_a	Optical Absorption Coefficient	cm^{-1}
Φ	Optical Fluence	J/cm^2
C_P	Specific Heat Capacity at Constant Volume	J/(kg K)
d_s	Delay	s
CF	Coherence Factor	dimensionless
CNR	Contrast to Noise Ratio	dimensionless
ΔI	Variation of intensity in ROI	arbitrary
σ_I	Standard Deviation of the background intensity	arbitrary
M	Molarity	M

D_a	Actual Depth of Object	m
D_i	Depth of Object in Image	m

UNIVERSITY OF MISSOURI

Design and Characterization of a Handheld, Waveguide-Mediated Photoacoustic Imaging Probe for Imaging Burn Wounds

Mason William Schellenberg

Heather K. Hunt, Thesis Advisor

Abstract

Clinicians correctly diagnose only ~66% of burn wounds, which may be in part due to the qualitative methods commonly employed for burn assessment. This often results in over diagnoses, which may lead to unnecessary treatments and reduced patient outcomes. Optoacoustic imaging can provide quantitative data about burns, but the methods used present limitations that have prevented the full capability of the modality to be realized.

To overcome this, our presented work used waveguide-mediated optoacoustic imaging. To demonstrate this method, a hand-held, waveguide-mediated optoacoustic imaging platform was developed and characterized by imaging optoacoustic targets within simple tissue phantoms. Unfortunately, enough energy could not be delivered to the hand-held probe to image tissue phantoms that resembled burns because the optical fiber used to deliver light to the waveguide could only handle a small amount of energy. Instead, a forward mode imaging setup was used that approximated the environment of the hand-held probe. This was able to image a burn wound tissue phantom that had a burn depth of 2.18 mm, which can image most burns. Therefore, the results demonstrated that the method has potential for imaging burn wounds *in vivo* if more energy is delivered to the probe.

Chapter 1

Introduction

This chapter is designed to introduce the reader to the clinical problem this project addresses, to optoacoustic imaging (OAI) of burn wounds, and to the specific goals of the project. First, the clinical problem is explored. This includes a review of burn wounds and their prevalence, as well as current methods of diagnosing burns and the limitations of these methods. Then, methods of OAI of burn wounds are reviewed to provide more insight into the scope of this work within the area of OAI of burn wounds. A detailed review of hand-held, OAI is reserved for Chapter 2. Lastly, the specific goals and technical objectives of the project are outlined.

1.1 Limitations in Burn Wound Diagnosis

1.1.1 Background of the Clinical Problem

Burn wounds are the 4th leading global cause of injury, resulting in over 11 million injuries that require care annually [1]. The primary causes for these burns are flames (84%) and scalding due to hot water or steam (8%), with the remaining causes coming from sources such as electrical or chemical burns (8%). Unfortunately, even in developed countries, clinicians only correctly diagnose burn wounds ~66% of the time [2]. In cases of misdiagnoses, clinicians commonly overestimate the extent of the burn, which may lead to unnecessary treatments, wasted resources, and overall reduced patient outcomes [2].

To fully understand this problem, it is instructive to review how burn wounds are diagnosed and the methods currently available to diagnose them. Burns can be classified into four categories based the depth of the damage [3]. These can be seen in Figure 1.1.

The least severe are superficial burns, where only the epidermis is damaged. When the epidermis and a relatively small portion of the dermis is damaged, the burn is classified as superficial-partial. When a significant portion of the dermis is damaged, the burn is classified as deep-partial. Deep burns, used to categorize the worst burns, extend through the dermis and into the subcutaneous tissue.

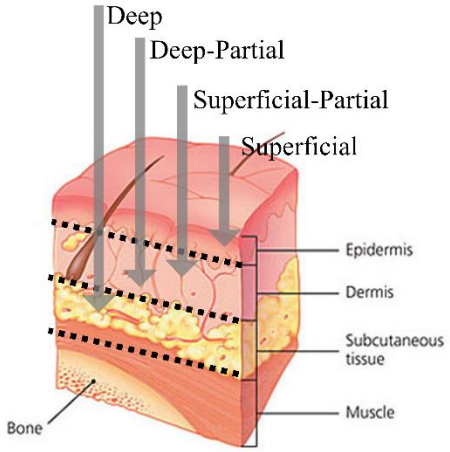

Figure 1.1. The primary metric of burn wound diagnosis is the depth of the damage. There are four categories of classifying burns based on depth. These are, ranging for least to most severe: superficial, superficial-partial, deep-partial, and deep. Adapted from Ref [3].

Burns can also be described by classifying parts of the burn into one of three ‘zones’, which describe portions of the burn not only by damage but by physiological response [4]. These three zones are the zone of coagulation, zone of stasis, and zone of hyperemia (Figure 1.2). The zone of coagulation, the innermost zone, is characterized by permanently damaged tissue, where proteins have become denatured and/or the plasma membranes of cells have been compromised. The second zone is called the zone of stasis, which is characterized by decreased blood flow. The outermost zone is called the zone of

hyperemia, which is undamaged but inflamed tissue that has a characteristically high blood volume content.

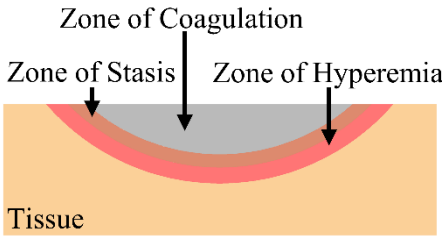

Figure 1.2. Schematic of the three zones that form in a burn wound. At the center of the burn is the zone of coagulation, where the tissue is permanently damaged. Next is the zone of stasis, where blood flow is decreased. The outermost zone is the zone of hyperemia, which is characterized by inflammation and a high blood volume content.

The most widely used method for diagnosing burn wounds is 'visual inspection' by a clinician [2]. Here, the clinician will observe the burn and, using their experience and best judgment, give an estimate of the severity of the wound. Due to its qualitative nature, it is difficult to accurately diagnose a burn with this method, particularly intermediate burns; while it is relatively easy to diagnose superficial and deep burns, superficial-partial and deep-partial burns are more challenging.

The second most common method of diagnosis is the punch biopsy [2]. Here, a needle is used to remove a column of the burned tissue, followed by histological analysis. The boundary of the wound can be visualized, thus determining wound depth. The primary concerns for this method are sampling error and invasiveness, so it is not commonly used in the clinic [2].

1.1.2 Recent Advancements in Diagnosing Burn Wounds

Thus far, several alternative methods of characterizing burn wounds have been seriously explored [5]. The three most common methods that have been used are thermal imaging (TI), laser doppler imaging (LDI), and the use of vital dyes [2]. All of these methods are based on characterizing blood perfusion within the burned tissue, which is an indirect

method of determining wound depth [2].

1.1.2.1 Thermal Imaging

Thermal Imaging (TI), also called thermography, analyzes burned tissue by mapping its surface temperature [2, 5]. Deeper burns are cooler than more shallow ones due to the lack of perfusion, and this can be visualized with TI. The modality has been shown to have an accuracy of up to 90%, and it is relatively fast and cost-effective [2]. Unfortunately, measurements using TI can be compromised due to variables such as evaporative heat loss, and only provides optimal results within 3 days of the burn injury [2, 5].

1.1.2.2 Laser Doppler Imaging

Laser Doppler Imaging (LDI) indirectly measures tissue perfusion by measuring the frequency shift imparted on light by blood cells flowing in tissue [2, 5]. This is based upon the principle that moving red blood cells causes light reflected off of them to undergo a Doppler shift due to the Doppler principle. LDI is a non-contact method and has been shown to provide assessments of burn depth with an accuracy of >90%. It remains the only method approved by the FDA of diagnosing burn wounds [5]. However, its accuracy is limited during the first two days post-burn [5]. The accuracy of the measurement may also be affected by otherwise beneficial topical ointments. Lastly, the clinical adoption of LDI has been slow due to the high cost of LDI systems.

1.1.2.3 Vital Dyes

To use vital dyes as a diagnostic tool to assess burn wounds, the dye must be injected into the burn wound patient intravenously and then the wound is inspected [2]. The method in which the wound is inspected is based upon which class of dye is used, and there are two classes: fluorescent and nonfluorescent. For fluorescent dyes, the tissue is illuminated by

light that excites the fluorescent dye. In healthy tissue, where the microvasculature is intact, the fluorescent images appear brighter [5]. As the tissue becomes more damaged, the fluorescent signals decrease due to lack of perfusion, which carries the dye. In order to provide an accurate picture, the wound must be cleared of any topical ointments, which poses some limitations on the technology. Also, the dyes used, although generally considered non-toxic, are known to have side effects [5]. Nonfluorescent dyes aid in diagnosing burn wounds by making the microvasculature more visible, but have not been demonstrated to be capable of distinguishing between deep-partial burns and full thickness burns [5].

The current methods of burn wound depth assessment pose many limitations that have slowed their adoption in clinical settings. Because of this, visual inspection still remains the most commonly used form of assessment, even with its low success rate [2]. It is therefore of great clinical interest that new methods of burn wound assessment be explored in order to improve the rate of successful diagnosis, leading to improved patient outcomes. Recently, OAI has been explored to diagnose burn wounds, and has been quite successful in animal studies [6-9]. In the following section we will explore these studies in detail.

1.2 Optoacoustic Imaging in Burn Wound Diagnosis

OAI is an imaging modality that utilizes the generation of mechanical waves due to light absorption, known as the optoacoustic effect (Figure 1.3) [10]. The premise of using optoacoustics in medical imaging is straightforward. First, the tissue of interest is illuminated by a pulse of light [11]. This light is absorbed by chromophores within the tissue, generating an optoacoustic wave within the range of ultrasound. These signals can

be detected by an ultrasound sensor, or array of sensors, and the signals can be used to make an image [12]. The contrast in this image is based upon the distribution of absorbed light, which is related to the wavelength of light used and the optical properties of the tissue under study [11]. A more detailed overview of hand-held OAI can be found in Chapter 2.

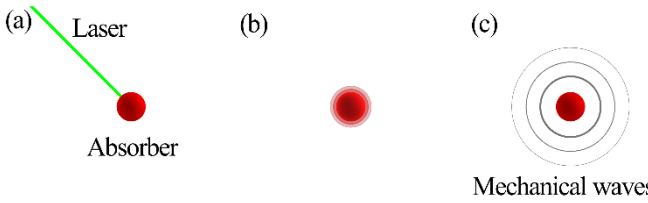

Figure 1.3. A schematic showing the optoacoustic effect. **(a)** First, a pulse of light is absorbed by an absorber. **(b)** The absorber undergoes thermoselastic expansion **(c)** Mechanical waves are produced.

Recent advancements in the OAI of burn wounds have been founded on the principle of illuminating the burn tissue with a wavelength of light that is strongly absorbed by hemoglobin in the hyperemic zone (Figure 1.4) [6, 7, 13]. This causes strong signals to be formed in the hyperemic zone, often termed the hyperemic bowl, which forms around burn wounds and is characterized by vasodilation and increased blood flow [6, 7, 13, 14]. By visualizing the boundary, the depth of the burn wound can be determined.

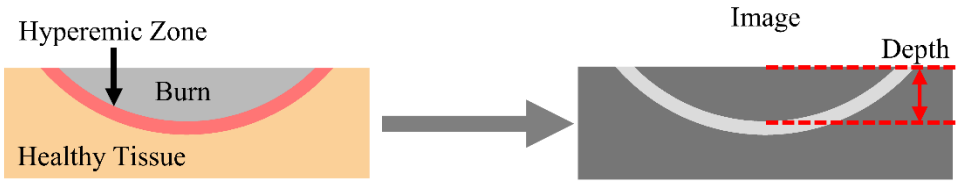

Figure 1.4. **[Left]** Basic schematic of a burn wound showing the healthy tissue, the damaged burn tissue (comprising of the zone of coagulation and zone of stasis), and the hyperemic zone. **[Right]** Schematic of an optoacoustic image of the burn wound. The high blood volume content of the hyperemic zone gives it contrast, allowing for the depth of the burn to be visualized.

Thus far, a few OAI platforms have been used to assist in burn wound diagnosis. The earliest was demonstrated in 2005 by Yamazaki *et al.*, in which rat burn models were imaged [9]. Cross-sectional images of the injury were acquired 12 hours post-burn, and the

platform was able to visualize the zone of hyperemia. Unfortunately, the platform was not demonstrated to be able to image beyond 1 mm, which would be necessary for a clinically viable platform. Another platform was demonstrated a year later by Zhang *et al.*, which used swine deep partial-thickness burn models, which are considered a better model for human tissue than murine models [8]. The platform was able to produce 3D images of burns up to a depth of ~1.7 mm. The first hand-held, real time imaging platform was demonstrated in 2014 by Ida *et al.*, in which murine burn models were used [7]. The system was able to image burns up to ~1.7 mm deep with a frame rate of up to 30 frames per second. The team also tested their platforms performance against LDI, showing that their platform could predict burn depth with greater accuracy [6]. The incorporation of OAI into a held-held platform is seen as an important mile-stone, as it is generally regarded that hand-held methods show greater promise in the clinic than benchtop ones [15].

Several methods of OAI have been explored for imaging burn wounds (a review of methods used in hand-held OAI can be found in Chapter 2), but the most successful method appears to be 2D optoacoustic computed tomography (OACT). In this method of OAI, an array of sensors is used, and the data gathered can be used to generate 2D images. The success of 2D OACT in imaging burn wounds over other methods may be attributed to the relative ease of implementing real-time imaging over a large field-of-view (FOV), which describes the size of the imaging plane.

1.3 Limitations of Light Delivery in Hand-Held Optoacoustic Computed Tomography

The primary limitation for hand-held OACT is that the ultrasound sensors currently used, piezoelectric transducers, are opaque [16]. This complicates light delivery to the tissue

because light cannot be delivered directly to the tissue underneath the transducer, where it is most sensitive, while the transducer is in contact with the tissue. Other methods of optoacoustic signal acquisition exist, but have not been adapted into hand-held OACT platforms. These include Fabry-Perot Interferometers [15, 17], as well as some noncontact methods [18, 19].

Several 2D OACT platforms have been developed to overcome this limitation (Figure 1.5). These include (1) illuminating the tissue from the sides of a linear array, (2) offsetting a linear array from the tissue using a transparent spacer, and (3) using a curved array which allows for space between the array and the tissue for illumination. In illuminating a linear array from the side, scattering of the light within the tissue is relied upon to deliver the light to tissue underneath the array [20-23]. The main limitation of illuminating the tissue from the sides of the array is that the majority of the optoacoustic signals will originate outside of the acoustic detection column of the array, degrading image quality [24]. The tissue directly underneath a linear array can be illuminated if the array is offset from the tissue, but moving the array away from the tissue leads to a decrease in image quality [16, 25]. This is because the optoacoustic waves must travel further to reach the sensors, decreasing the intensity of the recorded signal. The third solution is the use of curved arrays. While linear arrays are most sensitive to sources close to their surface, curved arrays of most sensitive to sources at the center of the circle which they encompass (Figure 1.6) [26, 27]. This allows for space between the array and the tissue in which light can be delivered to the tissue where the array is most sensitive. The primary drawback for curved arrays is their size. For most hand-held platforms, the FOV of a curved array is limited to a circle with a radius of ~¼ of the radius of the sensor array [28-34]. For linear

arrays, the FOV runs the entire length of the array and extends outward. This means for a curved array to have a FOV of the same size as a linear array, it must be ~4 times as big.

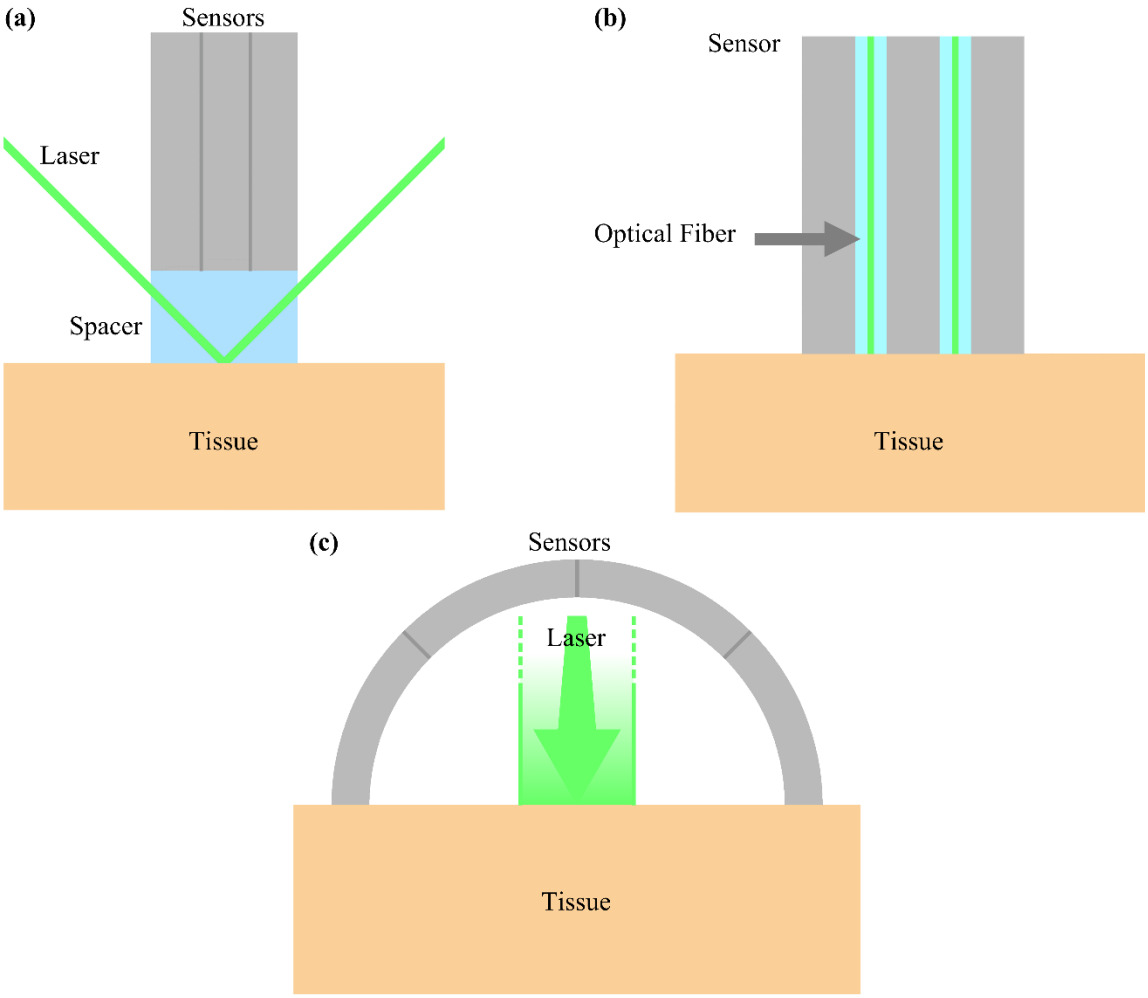

Figure 1.5 **(a)** A linear sensor array is offset from the tissue, and an optically transparent spacer is placed between them, allowing for direct illumination of the tissue underneath the array. **(b)** An alternating array of sensors and optical fibers, where the scattering of light within the tissue is used to deliver light to the tissue underneath the sensors. **(c)** A curved array, where the tissue is illuminated from the side of the array.

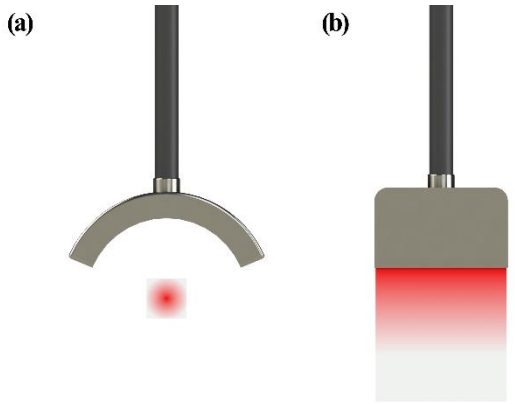

Figure 1.6. **(a)** The FOV of a curved array is at the center of the circle which the array encompasses. The FOV has a radius of ~¼ of the radius of the array. **(b)** The FOV of a linear array begins at the surface of the array and extends outward.

1.4 Project Proposal

The intention of this thesis is to address limitations of light delivery in hand-held, 2D, OACT and to adapt this solution to burn wound imaging, where it may be most beneficial. As described in the last section, there are three methods of light delivery in 2D OACT, each with their own costs and benefits. Of these, the use of curved arrays may be the least suitable for imaging burn wounds. Curved arrays offer improved resolution and the ability to image curved structures, but these benefits come at the cost of a greatly increased array size [27, 31, 35]. Reducing the array size is highly desirable when imaging burn wounds, as any contact between the imaging probe and the tissue can cause patient discomfort. Therefore, linear arrays are the best choice due to their smaller size, but these impose constraints on tissue illumination. This thesis proposes using optical waveguides to effectively deliver light to the tissue underneath the array while minimizing the distance between the array and the tissue surface, maximizing the strength of the received signal. This method is named ‘Handheld, Waveguide-Mediated, Optoacoustic Computed Tomography’, or WM-OACT for short.

WM-OACT builds upon the two well-founded concepts: OACT and the use of waveguides for light delivery to tissues. OACT is an established imaging technique used in both laboratory and pre-clinical imaging, which has been previously applied to imaging burn wounds with success in murine models [6, 7]. In these platforms, light was delivered to the sides the transducers, which results in much of the light being absorbed outside of the detection columns of the transducer elements (This is demonstrated in Chapter 4). This can cause most of signals to be generated outside of where the transducers are most sensitive. Unlike side illumination, WM-OACT allows for light to be delivered to the tissue where the array is most sensitive, improving image quality. We have previously shown that 1D optoacoustic images can be acquired using waveguides to deliver light [36]. In demonstrating that this method can be successfully adapted to hand-held 2D imaging, the potential of this method is shown not only for imaging burn wounds, but many other clinical applications as well.

1.5 Technical Objectives

In order to develop a more effective and useful imaging method for analyzing burn wounds, the viability of hand-held, 2D WM-OACT must be established. The work presented in this thesis intends to demonstrate that by characterizing a hand-held WM-OACT imaging method, and using it to image synthetic tissue that mimics a burn wound. The general technical objectives of this work are:

- to develop a synthetic tissue model that mimics the optical and acoustic properties of a burn wound
- to design and construct a hand-held platform that is capable of WM-OACT
- to characterizing the imaging capabilities of the platform

- and demonstrate its utility in burn wound diagnosis by imaging synthetic burn tissue

1.6 Bibliography

[1] M.D. Peck, Epidemiology of burns throughout the world. Part I: Distribution and risk factors, Burns 37(7) (2011) 1087-1100.

[2] S. Monstrey, H. Hoeksema, J. Verbelen, A. Pirayesh, P. Blondeel, Assessment of burn depth and burn wound healing potential, Burns 34(6) (2008) 761-769.

[3] E.D. Morgan, S.C. Bledsoe, J. Barker, Ambulatory Management of Burns, Am Fam Physician 62(9) (2000) 2015-2026.

[4] E.L. H., B. Dhaval, M. Peter, The biology of burn injury, Experimental Dermatology 19(9) (2010) 777-783.

[5] H. Ye, S. De, Thermal injury of skin and subcutaneous tissues: A review of experimental approaches and numerical models, Burns 43(5) (2017) 909-932.

[6] T. Ida, H. Iwazaki, Y. Kawaguchi, S. Kawauchi, T. Ohkura, K. Iwaya, H. Tsuda, D. Saitoh, S. Sato, T. Iwai, Burn depth assessments by photoacoustic imaging and laser Doppler imaging, Wound Repair and Regeneration 24(2) (2015) 349-355.

[7] T. Ida, Y. Kawaguchi, S. Kawauchi, K. Iwaya, H. Tsuda, D. Saitoh, S. Sato, T. Iwai, Real-time photoacoustic imaging system for burn diagnosis, J. of Biomedical Optics, SPIE, 2014, p. 7.

[8] H.F. Zhang, K. Maslov, G. Stoica, L.V. Wang, Imaging acute thermal burns by

photoacoustic microscopy, J. of Biomedical Optics, SPIE, 2006, p. 5.

[9] M.Y.S.S.H.A.D.S.Y.O.M. Obara, Measurement of burn depths in rats using multiwavelength photoacoustic depth profiling, J. of Biomedical Optics 10(6) (2005).

[10] L. Wang, J. Yao, A Practical Guide to Photoacoustic Tomography in the Life Sciences, Nature Methods 13(8) (2016) 11.

[11] Y. Zhou, J. Yao, L.V. Wang, Tutorial on photoacoustic tomography, J. of Biomedical Optics 21(6) (2016) 14.

[12] P.K. Upputuri, M. Pramanik, Recent advances toward preclinical and clinical translation of photoacoustic tomography: a review, J. of Biomedical Optics 22(4) (2016) 041006.

[13] J.A. Viator, S.L. Jacques, Limitations of Photoacoustic Measurement of Burn Depth, (47314) (2005) 849-854.

[14] J.D. MacG., The diagnosis of the depth of burning, British Journal of Surgery 40(164) (1953) 588-596.

[15] B. Zabihian, J. Weingast, M. Liu, E. Zhang, P. Beard, H. Pehamberger, W. Drexler, B. Hermann, In vivo dual-modality photoacoustic and optical coherence tomography imaging of human dermatological pathologies, Biomedical Optics Express 6(9) (2015) 3163-3178.

[16] E. Zhang, J. Laufer, P. Beard, Backward-mode multiwavelength photoacoustic scanner using a planar Fabry-Perot polymer film ultrasound sensor for high-resolution

three-dimensional imaging of biological tissues, Appl. Opt. 47(4) (2008) 561-577.

[17] A.P. Jathoul, J. Laufer, O. Ogunlade, B. Treeby, B. Cox, E. Zhang, P. Johnson, A.R. Pizzey, B. Philip, T. Marafioti, M.F. Lythgoe, R.B. Pedley, M.A. Pule, P. Beard, Deep in vivo photoacoustic imaging of mammalian tissues using a tyrosinase-based genetic reporter, Nature Photonics 9 (2015) 239.

[18] C. Buj, M. Münter, B. Schmarbeck, J. Horstmann, G. Hüttmann, R. Brinkmann, Noncontact holographic detection for photoacoustic tomography, J. of Biomedical Optics 22(10) (2017) 106007.

[19] Y. Wang, C. Li, R.K. Wang, Noncontact photoacoustic imaging achieved by using a low-coherence interferometer as the acoustic detector, Opt. Lett. 36(20) (2011) 3975-3977.

[20] Y. Zhou, S.V. Tripathi, I. Rosman, J. Ma, P. Hai, G.P. Linette, M.L. Council, R.C. Fields, L.V. Wang, L.A. Cornelius, Noninvasive Determination of Melanoma Depth using a Handheld Photoacoustic Probe, Journal of Investigative Dermatology 137(6) (2017) 1370-1372.

[21] Y. Zhou, G. Li, L. Zhu, C. Li, L.A. Cornelius, L.V. Wang, Handheld photoacoustic probe to detect both melanoma depth and volume at high speed in vivo, Journal of Biophotonics 8(11-12) (2015) 961-967.

[22] A. Needles, A. Heinmiller, J. Sun, C. Theodoropoulos, D. Bates, D. Hirson, M. Yin, F.S. Foster, Development and initial application of a fully integrated photoacoustic micro-ultrasound system, IEEE Transactions on Ultrasonics, Ferroelectrics, and

Frequency Control 60(5) (2013) 888-897.

[23] A. Garcia-Uribe, T.N. Erpelding, A. Krumholz, H. Ke, K. Maslov, C. Appleton, J.A. Margenthaler, L.V. Wang, Dual-Modality Photoacoustic and Ultrasound Imaging System for Noninvasive Sentinel Lymph Node Detection in Patients with Breast Cancer, Scientific Reports 5 (2015) 15748.

[24] K. Daoudi, P.J.v.d. Berg, O. Rabot, A. Kohl, S. Tisserand, P.J. Brands, W. Steenbergen, Handheld probe integrating laser diode and ultrasound transducer array for ultrasound/photoacoustic dual modality imaging, Optics Express 22(21) (2014).

[25] P. Beard, Biomedical photoacoustic imaging, Interface Focus 1(4) (2011) 602-631.

[26] A. Dima, N.C. Burton, V. Ntziachristos, Multispectral optoacoustic tomography at 64, 128, and 256 channels, J. of Biomedical Optics 19(3) (2014) 036021.

[27] A. Dima, V. Ntziachristos, Non-invasive carotid imaging using optoacoustic tomography, Optics Express 20(22) (2012) 25044-25057.

[28] A. Karlas, J. Reber, G. Diot, D. Bozhko, M. Anastasopoulou, T. Ibrahim, M. Schwaiger, F. Hyafil, V. Ntziachristos, Flow-mediated dilatation test using optoacoustic imaging: a proof-of-concept, Biomedical Optics Express 8(7) (2017) 3395-3403.

[29] V. Neuschmelting, N.C. Burton, H. Lockau, A. Urich, S. Harmsen, V. Ntziachristos, M.F. Kircher, Performance of a Multispectral Optoacoustic Tomography (MSOT) System equipped with 2D vs. 3D Handheld Probes for Potential Clinical Translation, Photoacoustics 4(1) (2016) 1-10.

[30] A. Dima, V. Ntziachristos, In-vivo handheld optoacoustic tomography of the human thyroid, Photoacoustics 4(2) (2016) 65-69.

[31] A. Taruttis, A.C. Timmermans, P.C. Wouters, M. Kacprowicz, G.M.v. Dam, V. Ntziachristos, Optoacoustic Imaging of Human Vasculature: Feasibility by Using a Handheld Probe, Radiology 281(1) (2016) 256-263.

[32] A. Buehler, M. Kacprowicz, A. Taruttis, V. Ntziachristos, Real-time handheld multispectral optoacoustic imaging, Opt. Lett. 38(9) (2013) 1404-1406.

[33] A. Becker, M. Masthoff, J. Claussen, S.J. Ford, W. Roll, M. Burg, P.J. Barth, W. Heindel, M. Schäfers, M. Eisenblätter, M. Wildgruber, Multispectral optoacoustic tomography of the human breast: characterisation of healthy tissue and malignant lesions using a hybrid ultrasound-optoacoustic approach, European Radiology 28(2) (2017) 602-609.

[34] G. Diot, S. Metz, A. Noske, E. Liapis, B. Schroeder, S.V. Ovsepian, R. Meier, E. Rummeny, V. Ntziachristos, Multispectral Optoacoustic Tomography (MSOT) of Human Breast Cancer, Clinical Cancer Research 23(22) (2017) 6912-6922.

[35] X.L. Deán-Ben, D. Razansky, Portable spherical array probe for volumetric real-time optoacoustic imaging at centimeter-scale depths, Optics Express 21(23) (2013) 28062-28071.

[36] M.W. Schellenberg, P.J.D. Whiteside, H.K. Hunt, Planar waveguide light transmission modality for backward-mode photoacoustic tomography, SPIE BiOS, SPIE, 2016, p. 97083O.

Chapter 2

Review of Hand-Held Optoacoustic Imaging

This section is meant to give an overview of hand-held OAI to provide context to how the presented project fits into the broader field of hand-held OAI. Reprinted with permission from Photoacoustics.

2.1 Introduction

Optoacoustic Imaging (OAI), also known as *Photoacoustic Imaging* (PAI), is a method of imaging that utilizes the generation of mechanical waves due to light absorption by chromophores within tissue (**Figure 2.1**) [1]. More specifically, the terminology of OAI is used to describe the light-induced sound phenomena that occurs when the excitation light is within the visible and near-infrared portion of the electromagnetic spectrum [2]. If the excitation energy is within the radio-frequency or microwave region, the imaging technique is instead referred to as *Thermoacoustic Imaging*. These two mechanisms of signal generation have been exploited for a wide range of applications over the past several decades, from gas spectroscopy, [3] to thin film characterization, [4] to studies of photosynthesis [5]. In 1982, Olsen published the first paper reporting successful 2D imaging with biomedical potential [2]. In the 1990s, optoacoustics (OA) began to be more seriously explored for applications in medical imaging due to advances in both laser light sources and acoustic detection equipment [6]; this was followed soon after by the first report of an *in vivo* imaging system in 1993 by Chen *et al*. [2].

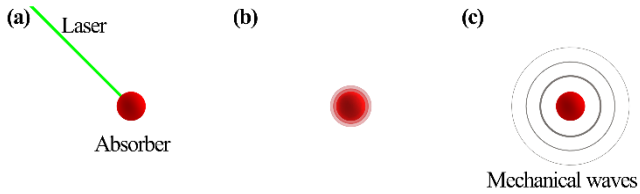

Fig. 2.1. The process of signal generation in optoacoustic imaging. (a) Light is absorbed. (b) The absorber undergoes thermoelastic expansion. (c) A mechanical wave is generated.

The premise of using OAs in medical imaging is straightforward. First, the tissue of interest is illuminated by a sufficiently short pulse of light, such that the pulse length satisfies both the thermal and stress confinement conditions [7]. This light is absorbed by specific components within the tissue, such as hemoglobin or lipids, generating a mechanical wave whose frequency is in the ultrasound regime. These signals can be detected by an ultrasound sensor, or array of ultrasound sensors, and the signals can be used to form an image with any of a variety of image reconstruction algorithms currently available in the literature [8]. The resulting contrast of the image is based upon the distribution of absorbed optical energy within the tissue, which is related to the wavelength of light used and the optical properties of the tissue under study [7].

The primary safety concern in OAI is the damage to tissue due to light exposure [9]. Most studies use the maximum permissible exposure (MPE) limits set forth by the American National Standards Institute (ANSI), which has written guidelines for the use of lasers in medicine [9, 10]. The limits described by the ANSI define the MPE for a single, short pulse of laser light (1-100 ns pulse length) with a wavelength between 400 to 700 nm to be 20 mJ/cm^2, and 100 mJ/cm^2 for wavelengths between 700 and 1400 nm. The ANSI also provides MPEs for applications that used repeated pulsed light. Other safety concerns for OAI include damage to the eyes of patients and practitioners. This may be addressed using common safety controls for lasers, which includes appropriate eye protection and engineering controls such as curtains.

Because OAI relies upon the absorption of light for signal generation and the detection of

ultrasound waves for signal acquisition, it presents several advantages over other medical imaging modalities, such as optical microscopy and ultrasound imaging. For example, typical high resolution, light-based imaging, such as optical microscopy or optical coherence tomography (OCT), have limited penetration depths in tissue due to the significant scattering of light within the tissue, making it difficult to clearly image fine structures beyond ~1 mm [6, 11, 12]. Ultrasound-based imaging systems, on the other hand, have a greater imaging depth than light-based systems, but are hampered in their ability to differentiate between soft tissue structures because of their similar mechanical properties. The modality relies on the acoustic mismatch between tissues to generate contrast, which is associated with their mechanical properties; soft tissues do not generate a substantial amount of acoustic differences [13]. In contrast, OAI combines the excellence of structure differentiation of light-based imaging with the imaging depth of ultrasound-based imaging: generation of optoacoustic signals is dependent on light absorption, making it possible to target specific biological compounds, such as hemoglobin and lipids, depending on the wavelength used [1]. The incident light, then, only needs to reach the target and be absorbed in order to generate the acoustic signal. Moreover, unlike light, ultrasound waves experience relatively little scattering in tissue, allowing for signals that are generated deep within the tissue to be reliably detected, pushing the OAI modality far beyond the limits of either light-based or ultrasound-based modalities [14].

In addition to the aforementioned advantages, OAI is scalable in terms of the resolution at which it can image: it can be used for macroscopic (75-3500 μm) [15, 16], mesoscopic (4.5-30 μm) [17, 18], and microscopic imaging (15-50 μm) [19]. Macroscopic imaging via the OAI modality, which is frequently accomplished using Optoacoustic Computed Tomography (OACT), is, for instance, capable of imaging entire organs [20]. Optoacoustic Microscopy (OMi), on the other

hand, can be used to image small sections of tissue, such as capillary beds and sub-cellular structures. This OAI method can be divided further into two classes based on how resolution is achieved: acoustic resolution (AR-OMi) and optical resolution (OR-OMi). In AR-OMi, the resolution of the system is determined by the acoustic detection components, whereas in OR-OMi, the resolution is determined by the properties of the excitation light. In order to capture the continuous scalability of OAI, so-called 'switchable' or 'hybrid' AR- and OR-OMi systems have been developed [21, 22]. These systems can employ either AR- or OR-OMi methods by simply adjusting some of their components, demonstrating the power of OAI scalability. Lastly, Optoacoustic Mesoscopy (OMe) fills the gap between OACT and OMi, and has recently emerged as a valuable addition to the OAI suite [23-26]. Different OAI methods relevant to *hand-held* platforms are discussed in detail in Section 2.2. Hand-held optoacoustic imaging platforms are typically defined as platforms that contain either a 'free' imaging head, i.e., are not rigidly attached to some supporting structure and whose position is able to be manipulated by the user, *or* are connected to an articulated arm and easy to manipulate by the user. **Figure 2.2** shows the different OAI methods and the relationships among the methods.

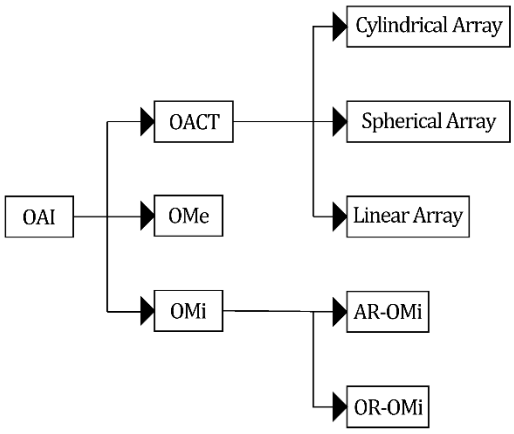

Fig. 2.2. A diagram showing the different methods of the OAI modality that are currently used in hand-held platforms, based on published literature. In this figure, we have separated the OAI modality into three general methods, based on the instrumentation and image forming methods used. Some of these methods can be further classified by the specifics of their instrumentation or their operation. We note that all of these methods can use both single wavelength excitation and multiple wavelength excitation (multispectral aka spectroscopic OAI), which provides another layer of functionality for the OAI modality.

As previously mentioned, specific targets can be singled out using different wavelengths for optoacoustic signal generation. This is known as multispectral or spectroscopic OAI and has been used to selectively image compounds such as oxy-/deoxygenated hemoglobin or lipids [27, 28]. In this technique, at least two separate wavelengths are used to interrogate the tissue, and the magnitude of the resulting optoacoustic response at each wavelength is used to determine the prevalence of the target of interest. This can become complicated, however, by the need to account for the wavelength-dependent nature of light propagation in tissue when analyzing the amplitude of optoacoustic signals that originate from a particular volume of tissue [29]. Multispectral or spectroscopic OAI can be used with all of the aforementioned OAI methods. For instance, spectroscopic OACT, often termed multispectral optoacoustic tomography (MSOT), has found much success in applications such as visualizing oxygen saturation in the vasculature around tumors, imaging tumors in breast tissue, visualizing sentinel lymph nodes (SLNs), and visualizing

vasculature deep in tissues, among others [30-39]. Additionally, spectroscopic OMe, often termed multispectral optoacoustic mesoscopy (MSOM), has been used for selectively imaging melanin and blood, as well as visualizing the structure of skin in patients with psoriasis [18, 40]. Lastly, quantitative OAI, a technique that uses multispectral OAI, seeks to quantitatively determine the concentration of a target; Quantitative OAI has proven more challenging because the fluence must be accurately modeled throughout the tissue so that it may be accounted for during signal processing [8]. Interested readers are referred to references [41] and [42] to learn more about spectroscopic OAI methods.

There are several metrics for evaluating OAI platforms. The first three are the axial, lateral, and elevational resolutions, analogous to ultrasound imaging [43-45]. These describe the spatial resolution of the platform along the imaging axis (axial), perpendicular to the imaging axis on the image plane (lateral), and between image planes (elevational). Other metrics include temporal resolution, contrast, and sensitivity. Temporal resolution is a measurement of how quickly a platform can acquire and generate images; high temporal resolution platforms are critical for improving the utility of OAI and reducing image artifacts [1, 46]. Contrast is typically measured as either the signal-to-noise ratio (SNR) or the contrast-to-noise ratio (CNR). SNR is defined as the average background signal over the standard deviation of the background signal [47], whereas CNR is defined as the intensity of signal that arises from the region of interest minus the average noise, divided by the standard deviation of the background signal. Lastly, sensitivity describes the minimum concentration of a target compound that the platform can detect [12].

Over the last two decades, OAI has been used in numerous studies, some of which we will list here to showcase its clinical applications. Common applications include imaging melanoma [19, 48-50], imaging vasculature in various organs to indicate the presence of tumors [49-52],

studying the vasculature around tumors [15, 53-56], studying brain activity [46, 57-61], and imaging lymph nodes to study tumor metastasis [62, 63]. Other applications include imaging the vasculature of the retina for diagnosing diabetic retinopathy [64], imaging intestinal inflammation due to Crohn's disease [32], imaging whole bodies of small animals [65], and imaging lipid plaque in the aorta [66]. While no clinical OAI platforms are currently available commercially, there are several platforms undergoing clinical trials [8]. As these clinical trials finish, we should expect to see commercially-available, clinical OAI platforms emerge.

Since OAI imaging was first proposed and demonstrated, the OAI research community has significantly refined the technology that supports OAI methods. As described by Taruttis and Ntziachristos, OAI has evolved in six dimensions [29]. The first three were spatial dimensions, referring to 1D (A-line scans), 2D (B-line scans), and 3D (volumetric) imaging. The next dimensional advancement was time-resolved imaging, allowing researchers to study dynamic processes in real time. This was achieved in large part due to the implementation of parallel signal detection methods from sensor arrays. Later, as laser technology advanced, the fifth dimension was established: spectroscopic imaging. Newly developed laser systems that could rapidly output different wavelengths were used to provide real-time OAI that could, for instance, determine the relative concentration of different compounds via spectroscopy [29]. This technique was first demonstrated in a hand-held MSOT platform in 2013, producing 2D images of oxy-/deoxyhemoglobin and melanin in human skin [67]. MSOT is a powerful technique that has greatly expanded the utility of OAI. The sixth and final dimension described was multi-scale imaging. This was realized recently at the benchtop level by Moothanchery and Pramanik (2017) [21], whose team developed a switchable acoustic resolution and optical resolution OMi (AR-OR-OMi) platform. Beyond these dimensions, OAI methods have benefited from technological advances

such as GPU-accelerated image reconstruction [68], specially designed ultrasound arrays [69], and advances in laser repetition rate, all of which increased imaging speed [70]. Finally, researchers have recognized that the translation of existing benchtop platforms, regardless of the OAI method employed, into *hand-held* OAI platforms could greatly expand OAI's potential applications in clinical settings [71].

In recent years, much energy has been devoted to researching and developing hand-held OAI platforms across the spectrum of OAI methods [14, 16, 21, 33, 34, 36-38, 46, 62, 67-69, 72-99]. These efforts are summarized in Table 2.1. However, despite the recent explosion of literature reporting hand-held OAI platforms and their uses (Figure 2.3), no comprehensive review of such hand-held platforms has yet been published. Therefore, this article attempts to fill this gap to provide readers with a sense of the current state-of-the-art of *hand-held* OAI platforms and the direction in which the *hand-held* OAI field is headed; however, we note that this is not meant to be a review of all OAI technology with clinical potential, nor is it meant to be a comprehensive review of benchtop platforms.

Table 2.1. List of select reported hand-held OAI platforms[a]. Methods in parenthesis indicate the nomenclature that was used by the authors of the referenced paper for the reported hand-held OAI platform. Under the 'Resolution' section, 'A' stands for axial resolution and 'L' stands for lateral resolution. Depth is maximum imaging depth reported. Speed is the time required to produce one image. DNR stands for 'Did Not Report'.

Subject	Target Tissue	Method	Resolution	Max Depth	Speed	SNR	Sensitivity	Ref.
Murine	Melanoma metastases in brain	2D OACT (MSOT) 3D OACT (MSOT)	A, L: 200 μm A, L: 240 μm	16.5 mm 14 mm	486 s 60 s	DNR DNR	137 cells/μL [b] 412 cells/μL [c]	[37]
	Melanoma	2D OMe (AR-PAM)	A: 59 μm L: 230 μm	3.7 mm	10 s	DNR DNR	Phantom tumor thicknesses 0.7 mm – 4.1 mm [d]	[14]
		2D OACT (PAT)	A: 86 μm L: 119 μm	DNR	0.2 s	DNR	DNR	[85]
	Detection of circulation melanoma tumor cells	2D OACT (PAT)	A: 86 μm L: 119 μm	DNR	0.2 s	DNR	6-10 clustered cells [e]	[82]
	Blood vessels in ear	3D OR-OMi (OR-PAM)	A: 26 μm L: 5 μm	0.54 mm [f]	0.5 s	DNR	DNR	[80]
		3D OR-OMi (OR-PAM)	A: DNR L: 7 μm	DNR	0.5 s	DNR	DNR	[95]
	Sentinel lymph nodes	2D OACT (PAI)	A: 207 μm L: 300 μm	15 mm	0.2 s	2.15 [g]	DNR	[99]
	Hemoglobin in burn wounds	2D OACT (PAI)	DNR	5 mm [h]	0.2 s	DNR	DNR	[81]
		2D OACT (PAI)	DNR	3 mm [h]	0.125 s	DNR	DNR	[100]
	Subcutaneous vasculature	2D OACT	DNR	DNR	0.2 s	DNR	DNR	[92]
Human	Vascular structure in thyroid	2D OACT (MSOT)	A: 250 μm L: 730 μm	5-20 mm below surface	0.1s	DNR	DNR	[38]

Human	Radial artery	2D OACT (MSOT)	A, L: 170 μm	DNR	0.02 s	DNR	DNR	[77]
	Deep vasculature in hand and forearm	3D OACT	A, L: 200 μm	DNR	0.1 s	DNR	DNR	[68]
		3D OACT	A, L: 200 μm	15 mm	0.1 s	DNR	DNR	[94]
	Vasculature in palm	3D OACT (MSOT)	A, L: 200 μm	6 mm	DNR	DNR	DNR	[89]
	Hemoglobin and melanin in breast tissue	3D OACT (MSOT)	A, L: 200 μm	22 mm	0.1 s	5 [i]	DNR	[83]
	Hemoglobin, melanin, and lipid structures around hair follicles	3D OACT (MSOT)	A, L: 75 μm	4.7 mm	0.05 s	DNR	DNR	[16]
	Hemoglobin and melanin in non-melanoma skin cancer lesions	2D OACT (MSOT)	A, L: 150 μm	DNR	DNR	DNR	DNR	[78]
		3D OACT (MSOT)	A, L: 80 μm	DNR	DNR	DNR	DNR	[78]
	Hemoglobin in breast tissue	2D OACT (MSOT)	A, L: 250 μm	30 mm	0.2 s	DNR	DNR	[34]
		2D OACT (PAI)	DNR	20 mm	DNR	DNR	DNR	[74]
	Hemoglobin, lipids, and water content in breast tissue	2D OACT (MSOT)	A, L: 115 μm	DNR	0.5 s	DNR	DNR	[33]
	Radial artery and vein	2D OACT (PAT)	A: 86 μm L: 119 μm	DNR	0.1 s	DNR	DNR	[79]
	Melanoma tumor	2D OACT (PAT)	A: 86 μm L: 119 μm	10 mm	DNR	DNR	DNR	[73]
	Mole on finger	3D OR-OMi (OR-PAM)	A: 30 μm L: 12 μm	DNR	20 s	DNR	DNR	[98]
	Hemoglobin in intestinal walls	OACT (MSOT)	DNR	DNR	DNR	DNR	DNR	[32]

Human	Vasculature in prostate	2D OACT (PAI)	DNR	15 mm	0.2 s	DNR	DNR	[101]
	Sentinel lymph nodes in melanoma patients	2D OACT (MSOT)	A, L: 300 μm	50 mm [j]	1.33 s	DNR	400 cells/μL [k]	[102]
	Sentinel lymph nodes tagged with dye	2D OACT (PAT)	DNR	DNR	0.2 s	DNR	DNR	[87]
	Arteries and veins in wrist	OACT (MSOT)	A, L: 115 μm	8 mm	0.02 s	20 dB [l]	DNR	[67]
	Red mole on leg	3D OR-OMi (OR-PAM)	A: 26 μm L: 5 μm	0.54 mm [f]	0.5 s	20 dB [m]	DNR	[80]
	Vasculature in cuticle	3D OR-OMi (OR-PAM)	A: 26 μm L: 5 μm	0.54 mm [f]	0.5 s	26 dB [n]	DNR	[80]
	Vasculature in patients with psoriasis	3D OMe (RSOM)	A: 4.5 μm L: 18.4 μm	1.5 mm	DNR	DNR	DNR	[18]
	Vasculature in nailfold of patients with systematic sclerosis	3D OMe (RSOM)	A: 8 μm L: 30 μm	1.5 mm	DNR	DNR	DNR	[17]
	Vasculature in foot	2D OACT (MSOT)	A, L: 100 μm	10 mm	0.1 s	14.3 [o]	DNR	[36]

[b, c] Sensitivity determined using cell suspension in phosphate-buffered saline 3 mm deep in tissue mimicking phantom.

[d] Phantom tumors were placed in gelatin and intralipid tissue phantom.

[e] Determined by monitoring circulating cell tumors injected into rat.

[f] Value was determined by imaging a hair in an optically scattering tissue phantom.

[g] Values taken from image of sentinel lymph nodes where indocyanine green was used as a contrast agent.

[h] Determined using burn mimicking tissue phantoms.

[i] Reported as CNR of one image at maximum imaging depth.

[j] Sentinel lymph nodes were tagged with indocyanine green a contrast agent.

[k] Measured using murine melanoma cells in agar phantom.

[l] Value taken from vein at a depth of 6 mm, excitation wavelength 720 nm, and surface fluence of 10 mJ/cm^2.

[m] Value taken from C-scan of red mole on volunteer's leg.

[n] Value taken from the average of 20 images.

[o] CNR reported for mean of large arteries.

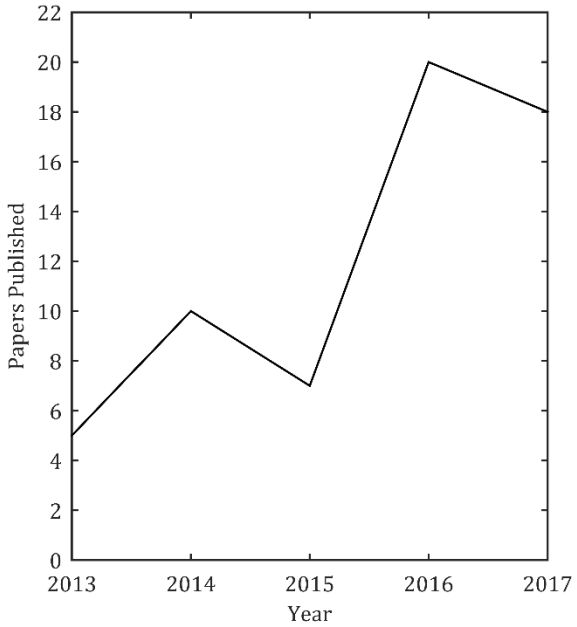

Figure 2.3. The number of peer-reviewed papers reporting hand-held OAI platforms, excluding conference proceedings, published per year from 2013 to 2017, showing the recent growth in the field. Data was obtained from Web of Science.

2.2 Instrumentation for Hand-held Methods of Optoacoustic Imaging

In OAI, cross-sectional or volumetric images of tissue are built by analyzing recorded optoacoustic signals that are generated within the tissue. Techniques vary between OAI methods.

OACT image formation remains relatively complicated, becoming in many ways a field of its own, with a multitude of image reconstruciton methods and algorithms that have been reported in the literature [8]. Each of these have their own advantages and limitations, and it is up to the discretion of the research team to decide which to use on the basis of their specific device and application. Typically, cross-sectional OACT images are made by using a two-dimensional array of ultrasound sensors [6]. Volumetric images, on the other

hand, typically are produced using a three-dimensional array of sensors or by scanning a two-dimensional array of sensors [1, 45]. Interested readers who would like to know more about image formation in OACT are referred to reference [103] for more details.

In OMe, an "out of focus" scanning method is typically used [23]. This involves using a focused transducer; the focal point is placed just above the tissue surface and treated it as a virtual detector. This is in contrast to other methods, where the focal point, if there is one, of the sensor or sensor array is inside the tissue. The single transducer is raster-scanned across the sample, and then tomographic image forming methods, similar to OACT, are used to create a cross-sectional or volumetric image [17, 18]. This method of OMe is termed raster-scanning optoacoustic mesoscopy (RSOM).

With OMi, imaging is more straightforward: a single sensor and/or excitation source is rastered across a sample. At each point, a one-dimensional image is created in the axial direction, as either one or both of the excitation light and/or the acoustic detection column are focused along this direction [1, 7]. These one-dimensional images are then stitched together to form a two-dimensional or three-dimensional image. In any imaging method, however, the quality of the image formed – as well as the overall performance of the platform - depends on both the equipment used for optoacoustic signal excitation and the equipment used to detect the resulting optoacoustic signals.

2.2.1. Light Sources

Light sources in OAI are often chosen based on their pulse length, pulse repetition rate, and the wavelength, or range of wavelengths, they produce. It is crucial to incorporate components with sufficiently short pulse lengths because pulse length is related to resolution; as the pulse length increases, the maximum imaging resolution a platform can

achieve decreases [70]. For OACT, typical pulse lengths range from 10-20 nanoseconds. For high-resolution methods (OR-OMi, AR-OMi, and OMe), pulse lengths are typically a few nanoseconds or less.

Pulse repetition rate describes how quickly a light source can fire successive pulses of light. High pulse repetition rates are not typically necessary for OACT because just one pulse is needed per image due to the use of sensor arrays which gather multiple signals simultaneously. Typical repetition rates in OACT range from 10-25 Hz. In OMe, AR-OMi, and OR-OMi, where raster scanning it used, high repetition rates are needed for quick imaging. This is because a laser pulse is needed at each raster scan point, so repetition rates in the kilohertz range are desirable for fast imaging.

The wavelengths that the light source can produce is crucial for any OAI platform. The light wavelength, or range of wavelengths, ideally is only absorbed by the target compound. For multispectral OAI, how quickly the light source can alternate between wavelengths is also taken into account. This is because fast wavelength tuning is necessary to allow for quick, accurate spectroscopic imaging [89]. A common complication that often arises in multispectral OAI is the motion artifacts that result from, for example, the patient's pulse. This necessitates that multispectral imaging be performed in short enough time spans that these motion effects become negligible [89]. This necessitates quick wavelength tuning and pulse repetition rates.

Lasers are traditionally used as light sources for OAI due to their spectral purity and short pulse lengths. As light-emitting diode (LED) technology has become more advanced, LEDs have become common in OAI [1, 72]. The principle drawback of using LEDs is that their pulse lengths are much longer than traditional laser sources, which

degrades the quality of the resulting image [104]. This occurs because image resolution is related to the pulse length of the light source used; as the pulse length increases, the maximum imaging resolution a platform can achieve decreases [70].

Alternatively, pulsed laser diodes (PLDs) have been used in OAI platforms; however, their low energy output has limited their functionality [1, 86]. The effect of optical energy is intuitive: increasing the energy increases the strength of the optoacoustic response, so high energies are desirable when choosing a light source for an OAI platform.

2.2.2. Sensors

There are two main classes of ultrasound sensors commonly used in OAI: the traditional ultrasound transducer, which uses piezoelectric elements [105], and Fabry-Perot Interferometers (FPIs) [6, 71, 106]. The primary limitation of piezoelectric transducers is that they are opaque, which creates complications in delivering light to the tissue. The principle advantage of FPIs over piezoelectric transducers is that the sensitivity of FPIs does not decrease with decreasing element size, as is the case with piezoelectric elements. This allows FPIs to be approximated as point receivers, which in turn allows for more accurate imaging [6, 105]. FPIs can also be made to be transparent, simplifying the delivery of light to the tissue [6, 105]. The main drawback of FPIs, however, is that the sample must be raster-scanned, which slows data acquisition in comparison to piezoelectric transducers [107]. Due to these drawbacks, while FPI sensors have great utility and potential in OAI, they have not yet been incorporated into any hand-held devices described in the literature.

Beyond these two classes, some non-contact methods of detecting optoacoustic waves have also emerged. For example, one such method measures the displacement of the sample tissue surface due to optoacoustic waves using low-coherence interferometry; it is

limited, however, by the necessity of coating the sample in a layer of mineral oil [108]. Another non-contact method of detecting optoacoustic waves is performed by measuring the change in the refractive index of the sample surface caused by optoacoustic waves [48], while yet another method uses holography [109]. However, while non-contact methods have intriguing potential, their primary limitation is that they have not yet demonstrated the ability to image anything deeper than several millimeters in tissue [48, 108, 109]. In the following sections, we will explore common combinations of light sources and sensors for each OAI method that has been adapted for hand-held imaging, beginning with OACT.

As mentioned previously, the resolution of an OAI platform can be limited by the properties of the excitation light used, but resolution can also be limited by the characteristics of the ultrasound detection equipment employed. So far, all reported hand-held OAI platforms use piezoelectric transducers, and the maximum theoretical resolution that can be achieved by a transducer or transducer array is dependent of the geometry of the array and its central frequency. When selecting or designing a transducer, or transducer array, for a particular application, these constraints need to be taken into consideration.

For OACT, arrays of piezoelectric ultrasound transducer elements are used, of which there are three geometries: linear, cylindrical, and spherical. Linear and cylindrical piezoelectric ultrasound transducer arrays are typically used for two-dimensional imaging, and spherical piezoelectric ultrasound transducer arrays are used for three-dimensional imaging [73, 77, 78]. The axial resolution of each array type is a function of the frequency response of the array. This can be described using Equation 2.1, where λ_c is the wavelength of high cut-off frequency of the array [70]. The lateral resolution of a linear array can be described using Equation 2.2, where w is the width of each sensor element. The lateral

resolution of cylindrical and spherical arrays can be described using Equation 2.3, where d is the distance from the center of the scanned area to the resolved point, r is the radius of the array.

$$R_{A,OACT} = 0.6\lambda_c \tag{2.1}$$

$$R_{L,OACT} = \sqrt{{R_{A,OACT}}^2 + w^2} \tag{2.2}$$

$$R_{L,OACT} = \sqrt{{R_{A,OACT}}^2 + \left((d/r)w\right)^2} \tag{2.3}$$

In AR-OMi, a single ultrasound transducer is used to detect optoacoustic signals [6]. The lateral resolution of AR-OMi is a function the numerical aperture of the lens used to focus the acoustic beam (NA), the photoacoustic center frequency (f), and the speed of sound in the tissue (c) [20]. This can be described using Equation 2.4. The axial resolution of AR-OMi can be described using Equation 2.5.

$$R_{L,AR-OMi} = \frac{0.71c}{NAf} \tag{2.4}$$

$$R_{A,OMi} = \frac{0.88c}{f} \tag{2.5}$$

Like AR-OMi, the OR-OMi method also uses one ultrasound transducer to detect optoacoustic signals. The transducer may either be focused or unfocused. The lateral resolution of OR-OMi is a function of the numerical aperture of the lens used to focus the light (NA) as well as the wavelength of light used (λ) [20]. The relationship can be expressed mathematically using Equation 2.6. The axial resolution can also be described using Equation 2.5, as it depends on the ultrasound transducer.

$$\mathrm{R_{L,OR-OMi}} = \frac{0.51\lambda}{\mathrm{NA}} \tag{2.6}$$

Another key limitation that is imposed upon OAI is the nature of acoustic wave

attenuation is tissue. Higher frequency ultrasound waves are attenuated more than lower frequency ultrasound waves over the same distance. This causes limitations on achieving both high resolution and deep imaging depths, with tradeoffs between both. As a result of this, OACT platforms, which have relatively low resolutions, typically use transducers with central frequencies between 5-20 MHz, and can achieve relatively deep imaging depths. Higher resolution platforms (OMe, AR-OMi, and OR-OMi) typically use transducers with central frequencies between 10-50 MHz, with some extending up to 180 MHz, but have shallower imaging depths [18].

In the following sections, we will explore common combinations of light sources and sensors for each OAI method that has been adapted for hand-held imaging, beginning with OACT.

2.2.3. Optoacoustic Computed Tomography

In conventional hand-held OACT, two-dimensional and three-dimensional images are made using unfocused light and an array of US transducers [1, 20]. To the authors' knowledge, there are two companies producing hand-held OACT platforms that have appeared in published research: iThera Medical and VisualSonics [37, 73, 78, 82, 85]. The hand-held OACT platforms produced by these companies are summarized in Table 2.2. The first hand-held OACT platform that utilized a linear array was developed by Niederhauser *et al.* (2005) and has been used to image blood vessels in human skin [92, 97]. Since then, the technique has been used by VisualSonics to develop a fully-fledged, commercialized, line of hand-held OACT platforms for research use. These have been used in a multitude of studies, although none are approved by the FDA for clinical diagnostics [73, 79, 82, 85, 92]. Other research teams have developed their own systems independently

[74, 99] or in collaboration with industry partners [87, 88].

Table 2.2. List of commercially available OAI systems[b]. Under the 'Resolution' section, 'A' stands for axial resolution and 'L' stands for lateral resolution. Depth is maximum imaging depth reported. Speed is the time required to produce one image. DNR stands for 'Did Not Report'.

Company	System	Method	Resolution	Depth	Max Speed	SNR	Sensitivity
Visualsonics	Vevo LAZR-X MX201 Transducer	2D/3D US-OACT/ US-MSOT	A: 110 μm L: 220 μm	10-20 mm	0.05 s	30 dB +/- 10 dB	< 100 nM (dynes, nanostructures)
	Vevo LAZR-X MX250 Transducer		A: 75 μm L: 165 μm				
	Vevo LAZR-X MX400 Transducer		A: 50 μm L: 110 μm				
	Vevo LAZR-X MX550 Transducer		A: 40 μm L: 80 μm				
iThera Medical	Acuity/ Acuity Echo	2D/3D US-OACT/ US-MSOT	A, L: 80 μm	DNR	0.02 s	DNR	DNR
	Explorer C50	RSOM/ MSOM	A: 10 μm L: 40 μm	3.5 mm	DNR	DNR	DNR

2.2.3.1. Linear Piezoelectric Ultrasound Transducer Arrays

Linear, piezoelectric, ultrasound transducer arrays were first introduced because conventional US imaging platforms could be easily modified for OACT imaging, simplifying the development process for OACT platforms [92]. This also allowed for easy implementation of dual modality US-OACT imaging platforms. In these platforms, the linear arrays were commonly focused in the elevation direction, known as cylindrical focusing, onto the imaging plane to reduce the strength of signals arising from outside the imaging plane. However, the piezoelectric ultrasound transducers and transducer arrays were opaque, so light could not be delivered to the tissue directly under the transducer when it was in direct contact with the tissue. In order to work around this complication, several compensating light delivery approaches have been developed.

The first approach to overcome the opacity of the piezoelectric ultrasound

transducers / transducer arrays is to simply deliver light to the sides of the transducer / transducer array and to rely on the scattering of light in the tissue to deliver light to tissue that is directly underneath the transducer / transducer array [73, 85, 87, 92]. A schematic of this approach can be seen in Figure 2.4. For the purpose of this review, we shall explore the studies mentioned previously in this subsection as an illustrative sample of the work done using this method to overcome the opacity of the transducers / transducer arrays.

Needles *et al.* (2013) reported the use of a linear array with 256 elements and a central frequency of 21 MHz in a dual-modality ultrasound-OACT (aka US-OACT) imaging platform [92]. The transducer used was acquired from VisualSonics. Light was provided by a tunable Nd:YAG laser operating between 750 and 850 nm with a 20 Hz repetition rate. This platform was used to generate 2D and 3D images that were used to visualize the oxygenation of blood within the jugular vein in mice, as well as within murine tumors. The authors noted that this device may be useful in pre-clinical monitoring of changes in tumor oxygenation during therapy or studying tumor hypoxia.

Garcia-Uribe *et al.* (2015) used an ultrasound imaging platform modified for US-OACT for imaging SLNs tagged with methylene blue dye [87]. A Q-switched Nd:YAG laser was used to pump a tunable dye laser operating at 10 Hz and 667 nm, chosen for its selective absorption by the dye relative to surrounding compounds. The team used the platform to assist surgical placement of a titanium marker clip on a SLN. The authors noted that this work paves the way for the use of this platform in guiding SLN biopsies.

Zhou *et al.* (2015) used an OACT platform from Visualsonics Inc. to generate 2D and 3D images of melanoma tumors in mice [85]. The transducer had a central frequency of 21 MHz and was made up of 256 elements. The array was focused cylindrically with a

focal length of 15 mm. Laser light was supplied by a tunable optical parametric oscillator (OPO), which provided light at 20 Hz pulse repetition rate, at a wavelength of 689 nm, which is strongly absorbed by melanin. An imaging speed of 5 Hz was achieved. Scanning of the 2D array allowed for volumetric imaging of the tumor. The authors noted that this platform could be applied in the clinic to assist in diagnosing melanomas because volume, which the platform can measure, is a better metric for tumor diagnosis than the current metric of tumor thickness. This imaging platform was also applied to imaging melanoma tumors in patients in a clinical trial [73]. The authors noted that the platform was able to image tumors at depths up to 10 mm and that the resulting depth measurements were in good agreement with depths measured via biopsy. The authors noted that this device could be applied to assist in surgical intervention. The principle drawback of this approach, however, was that many acoustic signals will originate near the sides of the transducer, outside of the acoustic detection column, which can result in a decrease in the quality of the resulting image [88].

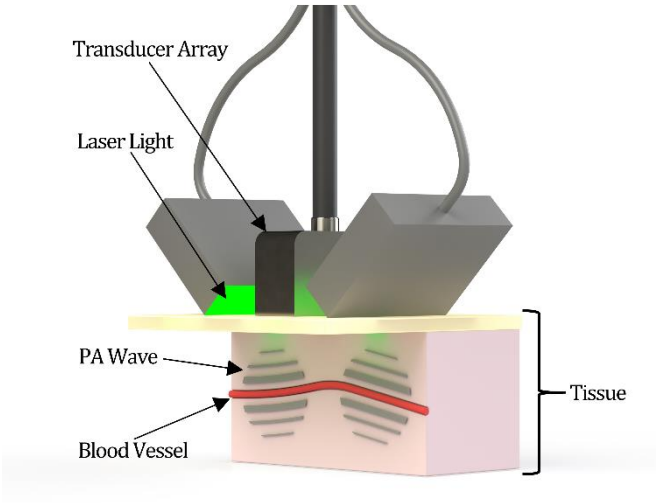

Figure 2.4. Schematic of OACT an imaging device that consists of a linear transducer array pressed against the tissue while light is delivered obliquely from the side. Adapted from [82].

The second approach used to overcome the opacity of piezoelectric ultrasound transducers / transducer arrays is to place an optically transparent spacer between the tissue and the transducer / transducer array, allowing room to direct laser light to tissue underneath the transducer / transducer array [74, 79, 88]. A depiction of this configuration is shown in Figure 2.5. Again, we will explore these representative studies to illustrate this method.

Daoudi *et al.* (2014), working with industry partners, developed a US-OACT platform and demonstrated its capabilities by imaging a human finger joint [88]. The authors of the study noted that in order to effectively deliver light deep into the tissue of the imaging plane, space must be allowed between the sensor array and the tissue surface. Using Monte Carlo simulations, the team found that, due to heavy scattering, the angle at which light was injected into the tissue had less of an effect on increasing fluence at depths ranging from 5 to 10 mm in the region of interest than decreasing the distance between the injection point and the imaging plane. To optimize fluence, the team distanced the sensor array 4 to 5 mm from the tissue surface in order to facilitate optimal fluence at the region of interest. The sensor array consisted of 128 elements with a central frequency of 7.5 MHz. A laser diode was used to provide light with a wavelength of 805 nm, which is absorbed primarily by the skin and blood vessels, and a pulse repetition rate of 10 kHz. Using this platform, the team was able to image the knuckle of one of the authors at a speed of 10 Hz.

Zhao *et al.* (2017) demonstrated a US-OACT probe for imaging the human breast [74]. To do this, the team modified a commercially available, ultrasound imaging platform

that used a piezoelectric ultrasound transducer array with 192 elements and that had a central frequency of 5.8 MHz. A Q-switched Nd:YAG laser was used to provide light, which operated at 1064 nm and a pulse repetition rate of 10 Hz. A transparent gel pad with a thickness of 4 mm was placed between the probe and the tissue. The team demonstrated their system by imaging the breast of a 47-year-old patient as a case study. The platform was shown to be able to image the vasculature in the breast and was able to demonstrate the importance of proper optical fluence compensation in optoacoustic image formation. The main drawback of using a spacer is that in moving the sensor array away from the target tissue, the SNR is reduced due to the increased distance the acoustic waves must travel to reach the sensor. [6, 105].

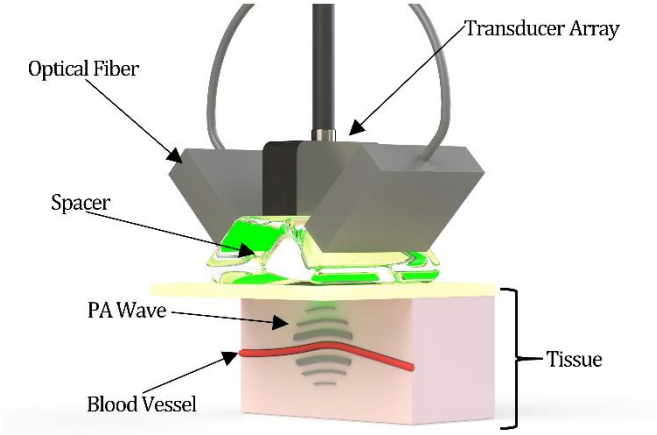

Figure 2.5. Depiction of an OACT imaging device that uses an optically transparent spacer to offset the transducer from the tissue. Laser light, delivered by an optical fiber, can then be directed to tissue underneath the transducer. Adapted from [74].

The third approach for overcoming the opacity of piezoelectric ultrasound transducers / transducer arrays is to manufacture transducer arrays so that optical fibers can be placed between the individual elements. This approach is utilized in the report by Ida *et al.* (2015) to image burn wounds in rats [81]. A schematic of this can be seen in Figure 2.6. The intent of this approach is to cause the platform to function much like platforms where

the transducer array is illuminated from the side. In this report, the transducer array consists of eight elements and has a central frequency of 10 MHz. The light source is a fiber laser that outputs light with a wavelength of 532 nm at a reputation rate of 500 Hz. The platform is able to image burns at a rate of 5 Hz, and the burn depths determined by the platform are reported to be in good agreement with those determined by histology. While the idea is novel, it still suffers from light illuminating tissue from the sides of the elements, which causes many signals to originate outside of where the ultrasound array is most sensitive, which in turn decreases the resulting quality of the image.

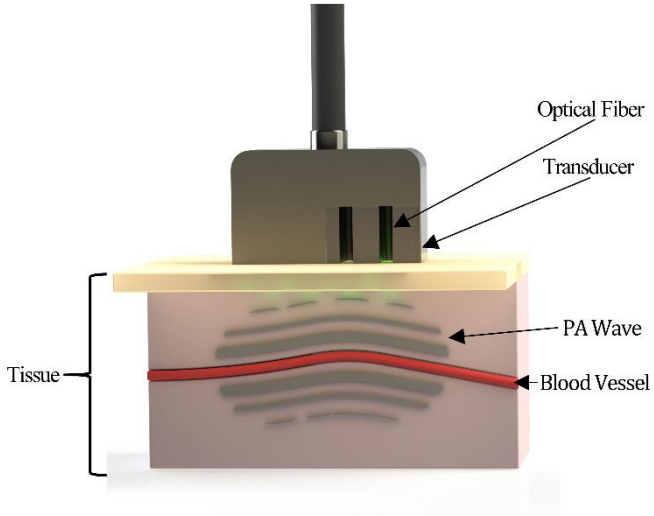

Figure 2.6. A simplified representation of the system used by Ida *et al.*, (2015), described in [81]. Here, part of the transducer-optical fiber housing is cut away to show the internal organization. The transducer elements and optical fibers are arranged linearly, alternating between transducers and fibers.

While OACT platforms that use linear arrays have some advantages, such as relatively small array size and ease of implementation, over other transducer array geometries, their major drawback is their resulting image quality [69]. The viewing angle of linear arrays is inherently limited, reducing the overall resolution of the system as well as being reducing their ability to image sloped surfaces.

2.2.3.2. Curved (Cylindrical) Piezoelectric Ultrasound Transducer Arrays

Fortunately, curved arrays provide excellent resolution by increasing the viewing angle of the array in comparison to linear transducer arrays [94]. Additionally, curved arrays can also reduce image artifacts and have greater ability in imaging sloped surfaces [36, 69, 94]. Moreover, while the sensitivity of a linear array is greatest closest to the array surface, curved arrays have greatest sensitivity at the center of the circle they encompass [69, 110]. This space between the surface of the array and where it is most sensitive, called the field of view (FOV), allows for light be to be delivered directly to tissue within the FOV. Most curved arrays used in hand-held OACT platforms provide 180-degree coverage or less [33, 34, 36-38, 67, 77]. As a rule of thumb, this limits the FOV to a volume with a radius that is about one quarter of the radius of the curved array, so these advantages come at the expense of array size [69, 110]. This is in contrast with linear arrays, where the FOV runs the entire length of the array (Figure 2.7).

The first hand-held OACT (MSOT) platform that used a curved array was reported by Buehler *et al.* (2013) and was demonstrated using a platform that was developed in-house [67]. The system used a tunable OPO with an output range of 680 to 980 nm pumped by an Nd:YAG laser with a repetition rate of 50 Hz. The piezoelectric ultrasound transducer array consisted of a curved array of 128 elements with a central frequency of ~8 MHz. The team demonstrated the imaging capabilities of the platform by imaging the wrist of a volunteer, using blood as the primary endogenous contrast agent. The team also observed changes in blood oxygenation and total blood volume in a volunteer's finger when blood flow to the finger was obstructed. The team noted they hoped to apply this technology to clinical applications related to cardiovascular disease.

Since then, multiple studies have been conducted using similar configurations [36,

38, 77]; these platform configurations have been frequently used in OACT (MSOT) studies [32-34, 37, 67, 102]. Much of this work has been done as a collaboration between iThera Medical and the Helmholtz Zentrum München. A basic schematic of the operation of a curved array can be seen in Figure 2.8. In order to facilitate acoustic coupling between the tissue and the transducer array, the cavity is often filled with water and sealed with a transparent membrane. In order to explore the capabilities of OACT (MSOT) platforms using curved array transducers, we will review several selected studies that have been recently published below.

Dima and Ntziachristos (2016) demonstrated the use of an OACT (MSOT) platform that utilized a curved array to image the thyroids in two female volunteers [38]. The curved array was made of 64 elements encompassing a circle with a radius of 40 mm and an angular coverage of 172°. The array had a central frequency of 7.5 MHz. 800 nm light was delivered by a pulsed laser system that operated at a repetition rate of 10 Hz. The team was able to visualize the outline of the thyroid as well as vasculature structures 20 mm deep within the tissue. The authors noted that the device could possibly be applied to assist in the diagnosis of thyroid disease as well as guiding fine needle aspiration.

Taruttis *et al.* (2016) used a platform with a curved array for OACT (MSOT) imaging of vasculature in the feet of healthy volunteers [36]. The curved array consisted of 128 elements with a central frequency of 8 MHz and a focal length of 20 mm. The angular coverage of the array was 135°. Light was supplied by a diode-pumped Nd:YAG laser pumping an OPO that output light at wavelengths of 730 nm, 750 nm, 800 nm, and 830 nm. Additionally, the platform was capable of performing multispectral imaging at an imaging speed of 2.5 Hz. The team was able to demonstrate the platforms' ability to image

both large and small vessels. The authors noted that potential clinical applications of the platform include assessing diseases as well as visualizing the results of stent placement.

Diot *et al.* (2017) used an OACT (MSOT) platform with a curved array to identify OA-resolvable features of breast cancer [33]. The curved array consisted of 265 elements with a central frequency of 5 MHz. The radius of the curved array was 60 mm and had an angular coverage of 174°. A tunable pulsed laser was used for illumination, operating at repetition rate of 50 Hz and 28 wavelengths between 700 and 970 nm. The team reported achieving an imaging speed of 2 Hz. The platform was able to resolve four separate target compounds: oxygenated hemoglobin, deoxygenated hemoglobin, lipids, and water. The team found that they were able to visualize vascular patterns and the disruption of tissue layers associated with tumors with this platform. The researchers further explained that this platform could be used to assess tumor function and the effects of neoadjuvant chemotherapy.

Knieling *et al.* (2017) used a commercially available OACT (MSOT) platform with a curved array to assess Crohn's disease activity in the bowels in a clinical trial [32]. The platform used near infrared (NIR) light to target hemoglobin as an endogenous contrast agent because tissue perfusion is associated with Crohn's disease activity. Six wavelengths were used in imaging, ranging from 700 to 900 nm, and were used to spectrally determine total hemoglobin, oxygenated hemoglobin, and deoxygenated hemoglobin within the target tissue. The clinical study recruited 91 patients. Endoscopic scoring, histologic scouring, and ultrasonography were all used as reference tests. Using data obtained from the platform, the team was able to distinguish between active and non-active forms of Crohn's disease with a p-value less than 0.001. The team noted that the results of the study were

encouraging and indicated that MSOT could be used to distinguish active forms of Crohn's disease from non-active forms.

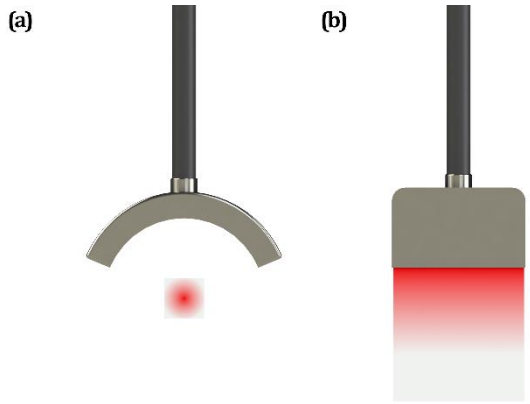

Figure 2.7. (a) A curved array transducer with 180-degree coverage of the FOV. The FOV, where imaging quality will be best, is highlighted in red. (b) A linear array transducer with its FOV highlighted in red.

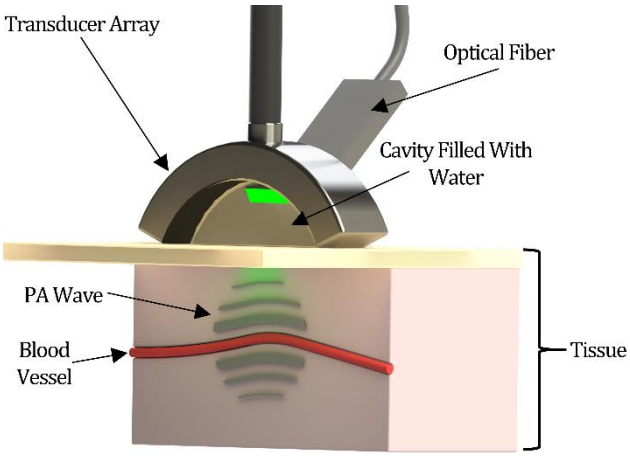

Figure 2.8. Partial cut-away view of a curved ultrasound transducer array is used to image flat tissue. The cavity between the array and the tissue is filled with water and sealed to facilitate acoustic coupling. Laser light is delivered obliquely from the side of the array. Adapted from [67].

2.2.3.3. Spherical Piezoelectric Ultrasound Transducer Arrays

When compared to curved arrays, the advantage of using a spherical array is its ability to

perform rapid volumetric imaging, which is crucial for studying certain dynamic physiological phenomena, such as visualizing blood oxygenation for diagnostic purposes [16, 46, 68]. Unfortunately, this comes with certain disadvantages. A comprehensive comparative study of the performance of spherical and curved arrays demonstrated that a major weakness of current spherical arrays is their reliance on light scattering to deliver light to the entire imaging volume [37]. In highly absorbing tissues, this limits the ability of the spherical array to image the entire volume accurately. The authors of that study explained that, until a solution is developed, OACT platforms that utilize spherical arrays may best suited for imaging superficial tissues, while OACT platforms that utilized curved arrays are better for targets located deeper in the tissue.

Spherical arrays were first implemented in a hand-held OACT platform by Deán-Ben, Ozbek, and Razansky (2013), using a custom-made spherical array that was then modified by the team to improve its performance [94]. The configuration consisted of a hemispherical transducer array that had an optical fiber placed in the middle of the array (Figure 2.9). Light scattering was used to deliver light throughout the imaging volume [37]. The cavity between the array and the tissue was filled with water and sealed with a transparent film to facilitate acoustic coupling. The spherical array consisted of 256 elements, an angular coverage of 90°, and a central frequency of 4 MHz. An OPO with a repetition rate of 10 Hz and wavelength of 800 nm was used for illumination. Light with a wavelength 800 nm was chosen because it is the isosbestic point of the hemoglobin, which was used as the endogenous contrast agent in the study. The platform was able to image vasculature in the arm and forearm of a healthy volunteer at a rate of 10 Hz. The authors noted that this device could be used in dynamic tracking of hemodynamic events and

circulating cells. This innovation spurred multiple other studies [37, 68, 78, 83, 93] and has been integrated with a number of OACT platforms to good effect [16, 89, 102]. Some of the most recent and compelling work was conducted as a collaboration between iThera Medical and the Helmholtz Zentrum München [16, 78], which will be reviewed here.

Fort *et al.* (2016), used an OACT (MSOT) platform with a spherical array to assess morphometric parameters of hair follicles, surrounding lipids, and associated capillary beds [16]. The transducer array consisted of 512 elements that had a central frequency of 10 MHz and a solid angle coverage of 140°. Light was supplied by the pulsed laser system, which was capable of operating at a repetition frequency of 100 Hz and was tunable between wavelengths ranging from 660 to 1300 nm. Heavy water was used to fill the cavity between the sensor and the tissue because it absorbs less light than water in the wavelength range used. The system was able to image an entire hair follicle, resolving four separate compounds: melanin, lipids, oxygenated hemoglobin, and deoxygenated hemoglobin. The authors state that while the results of the study are encouraging, they were not confirmed using a different method of measurement. The authors noted that histopathology could be a valuable method of analysis, but other methods would be needed to validate longitudinal studies. The authors hoped to apply this technology to further study hair follicles and to visualize the effects of various treatments of disorders such as hair loss.

Attia *et al.* (2017), utilized an OACT (MSOT) platform with a spherical array to characterize non-melanoma skin cancers [78]. The team recruited 21 patients and used the platform to determine tumor dimensions in the patients. Illumination was provided by a tunable OPO laser that operated at a repetition rate of 10 Hz and wavelengths ranging from 700 to 900 nm. The platform was able to provide multispectral images, differentiating

between the optoacoustic targets (melanin, oxygenated hemoglobin, and deoxygenated hemoglobin) in real time. The authors concluded that while the study included only a limited number of patients, they were confident the platform could be applied to mapping skin cancers and could be used to guide surgical interventions.

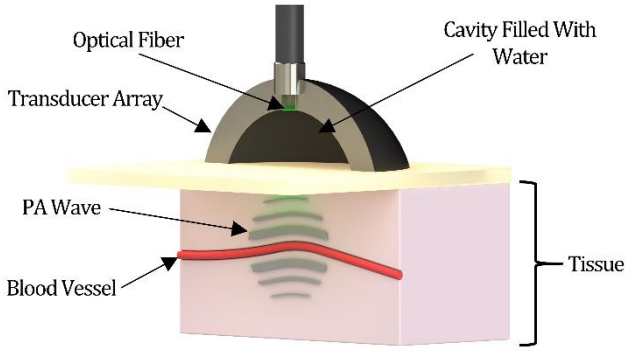

Figure 2.9. A partial cut-away view of three-dimensional hemispherical transducer array being used to image tissue. The volume between the array and the tissue is filled with water and sealed to provide acoustic coupling. Laser light is delivered using an optical fiber placed in the center of the hemisphere. Adapted from [94].

2.2.4 OMe

In OMe, a single transducer is used for signal acquisition, along with broad illumination of the tissue surface [23, 26, 40]. The instrumentation in OMe is unique in that the focal point of the array is placed just above the tissue surface, treating the focal point as a point detector. By offsetting the transducer from the surface, there is enough space to directly illuminate the target tissue. Hand-held OMe has taken the form of RSOM and was first demonstrated by Aguirre *et al.* (2017); RSOM technology is relatively new, and no commercial systems exist at this time. [18].

In Aguirre *et al.'s* study, the team developed a scanning head attached to an articulated arm that allowed for easy placement of the platform on the target tissue (Figure 2.10). The scanning head consisted of a spherically-focused, piezoelectric ultrasound

transducer with an ultra-broadband (UB) detection range that extended from 10 to 180 MHz. The transducer had a diameter and focal distance of 3 mm. To enable raster scanning, the spherical array was fixed to motorized stages. The bottom of the scanning head was sealed with an optically and acoustically transparent plastic, and the space between the transducer and the plastic was filled with water to provide acoustic coupling. The team employed a laser system with a pulse length of less than 2 ns, allowing the generation of ultrasound waves across a broad frequency spectrum. Illumination of the tissue was accomplished using two rectangular bundles of optical fibers placed on opposite sides of the spherical array. The received signals were separated into two groups based on frequency. These two groups of data were reconstructed and normalized separately to account for the attenuation of relatively low intensity of high-frequency sources. The two images were then co-registered to allow the visualization of high intensity, low frequency, low resolution targets alongside low intensity, high frequency, high resolution targets. Using this method, the team was able to image a 4 mm X 2 mm area in 70 seconds with a lateral resolution of 18.4 μm, an axial resolution of 4.5 μm, and an imaging depth of 1.5 mm. The team used the device to visualize changes in skin features in patients with psoriasis.

A similar platform was also demonstrated in a study by J. Aguirre *et al.* in 2018 [17]. The difference between this platform and the one previously described was that the 2018 platform used an ultrasound transducer with a central frequency of 55 MHz and an ultra-broadband (UB) detection range that extended from 10 MHz to 120 MHz. This transducer was chosen because the lower central frequency allowed signals from deeper in the tissue, where the region of interest was located, to be received. This transducer provided

a lateral resolution of 30 μm and an axial resolution of 8 μm. The team demonstrated the utility of the device by visualizing vascular biomarkers in nailfold capillaries in patients with systemic sclerosis.

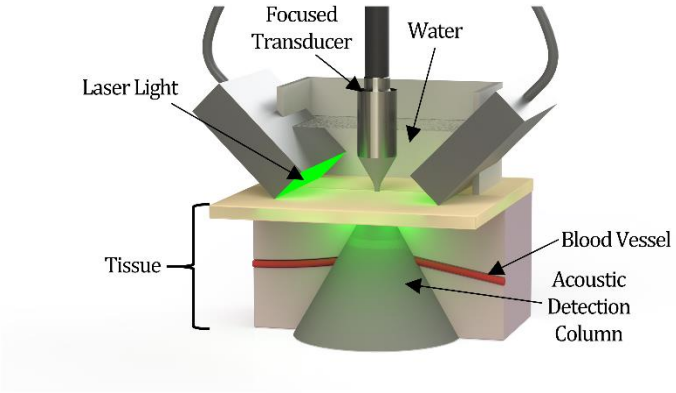

Figure 2.10. Schematic of a RSOM device. A single focused transducer is placed above the tissue with the focal point just above the tissue surface. The transducer is fixed to two translational stages to facilitate raster scanning. Light is provided by two optical fibers on opposite sides of the transducer. A transparent membrane is used to seal the bottom of the device, and water is used to facilitate acoustic coupling between the tissue and the transducer. Image adapted from Ref. [18].

2.2.5 OMi

As mentioned previously, Optoacoustic Microscopy (OMi) is used to image small sections of tissue, such as capillary beds. This OAI method can be divided further into two classes based on how resolution is achieved: acoustic resolution (AR-OMi) and optical resolution (OR-OMi). In AR-OMi, the resolution of the system is determined by the acoustic detection components, whereas in OR-OMi, the resolution is determined by the properties of the excitation light. In order to capture the continuous scalability of OAI, so-called ‘switchable’ or ‘hybrid’ AR- and OR-OMi systems have been developed [21, 22]. These systems can employ either AR- or OR-OMi resolution methods by simply adjusting some of their components, demonstrating the power of OAI scalability.

2.2.5.1. AR-OMi

Dark-field illumination is one of the most common configurations for AR-OMi, and has recently been integrated into a hand-held probe (Figure 2.11) [6, 14, 111]. In dark-field illumination, a piezoelectric ultrasound transducer is offset from the tissue, and acoustic coupling is accomplished using water. Laser light is fired around the transducer, obliquely illuminating the tissue under the transducer. If the transducer is small enough, laser light can be delivered normal to the tissue, and light scattering is used to deliver light to tissue that is underneath the transducer (Figure 2.12) [14]. Images are made by either scanning the transducer in a straight line, to produce a cross-sectional image, or raster scanned, to produce a volumetric image.

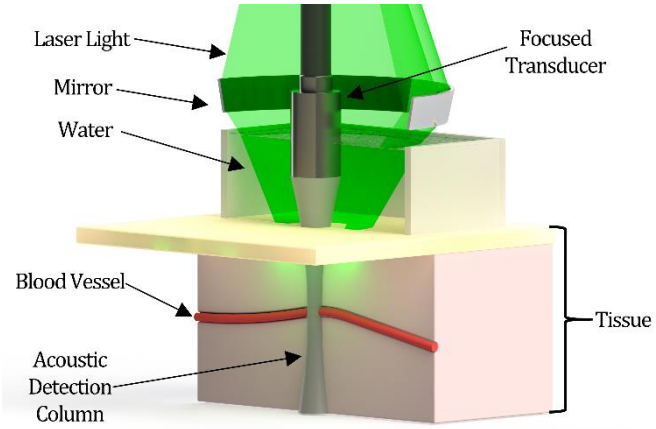

Figure 2.11. Partial, cut-away view of dark-field illumination for AR-OMi. Laser light is directed around the transducer, which is offset from the tissue. Adapted from [111].

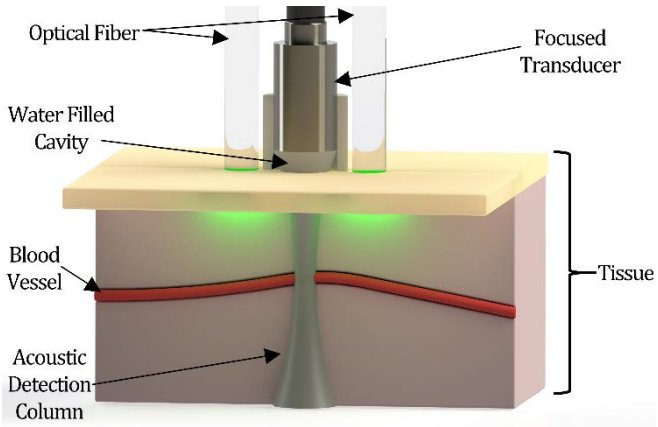

Figure 2.12. Partial, cut-away view of direct illumination of tissue in AR-OMi. Laser light is delivered to the tissue next to the transducer and a normal incidence angle using optical fibers. Illumination of acoustic targets beneath the transducer is facilitated by the scattering of light. Adapted from [14].

To the authors' knowledge, no hand-held platform has been developed that harnesses the resolving power of AR-OMi, which has been demonstrated to be able to achieve 15 μm axial resolution and 45 μm lateral resolution in benchtop setups [19, 63]. One hand-held platform has been developed, by Zhou *et al.* (2014); this platform had a lateral resolution of 230 μm and an axial resolution of 59 μm [14]. Due to this relatively low resolution, it may be more appropriate to designate this as a mesoscopic imaging platform, despite its configuration as an AR-OMi platform [12]. In Zhou's design, a small, 25 MHz piezoelectric ultrasound transducer was used to image melanoma tumors in mice. The light was delivered to the hand-piece using an optical fiber that illuminated the area around the transducer at a normal incidence angle. Monte-Carlo simulations were performed to demonstrate the diffusion of light from the side of the transducer to the target underneath it. This configuration was chosen because previous iterations of the design, which delivered light directly to the melanoma tumor, were unable to illuminate the entire tumor volume due to strong optical attenuation within the melanoma itself. This limited the platform's ability to image deep melanomas because light could not be delivered to the

base of the melanoma. By delivering light to the side of the region of interest, the base of the melanoma could be illuminated by the light scattered around it. The transducer and optical fiber were connected to a motorized translational stage and used to produce cross-sectional images. Excitation light with a wavelength of 650 nm was chosen because it is strongly absorbed by melanoma, but not hemoglobin or water. The authors noted that the practical limitation of the platform was the scanning speed, which was limited by the laser's repetition rate.

2.5.2 OR-OMi

The most common configuration for an OR-OMi platform uses a so-called 'opto-acoustic beam combiner' (OABC), also called an 'opto-ultrasound combiner', to coaxially align the laser with the detection column of the transducer [21, 98]. One manifestation of this configuration can be seen in Figure 2.13 [80]. The principle of an OABC is to use an object that has either an optical or acoustic reflective layer to align the incident laser light with the acoustic detection column. The incident laser beam is orientated orthogonally to the acoustic detection column, and the two are combined at the reflecting layer. Volumetric imaging is achieved by rastering the laser point and, if the transducer is focused, the acoustic detection column across the tissue surface.

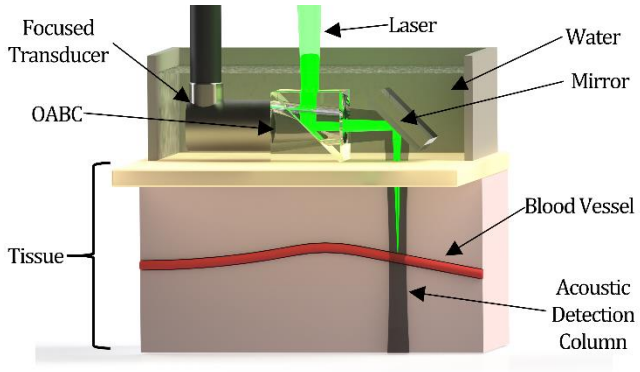

Figure 2.13. Depiction of an optoacoustic beam combiner (OABC) used in OR-OMi. This OABC contains an optically reflective layer that does not affect acoustic wave propagation. Incident laser light is placed orthogonally to the acoustic detection column of the transducer, and the two are combined in the OABC. The laser is raster scanned by a MEMS mirror. Adapted from [80].

To the authors' knowledge, three hand-held OR-OMi platforms have been developed, but none are currently commercially available [80, 95, 98]. The first platform to be reported, by Hajireza, Shi, and Zemp (2011), consisted of a 10 MHz focused transducer coupled to an OABC that contained an acoustically reflective surface [95]. Laser light was delivered using an image guide fiber, and scanning of laser light occurred as light was being coupled into the fiber. Fast imaging of microvasculature in the ear of a mouse was accomplished by utilizing a scanning mirror to raster scan the acoustic detection column and excitation light over the region of interest. The excitation light source, a pulsed fiber laser producing 532 nm light with a repetition rate of 160 kHz, was likely chosen to target hemoglobin and to facilitate quick imaging. The system was able to achieve images with a lateral resolution of 7 μm scanned over a 0.4 mm X 0.4 mm surface at a rate of 2 Hz and was limited by the scanning speed of the mirror. The authors noted the platforms' potential uses in clinical and pre-clinical applications included assessing melanoma sectioning and imaging angiogenesis, among others.

The second platform was reported by Lin *et al.* (2016) (similar to Figure 2.13) [80]. A 50 MHz transducer was used to detect the optoacoustic signal, and a mirror was used to scan the laser light across the sample. A fiber laser with a pulse repetition rate of 88 kHz that output light with a wavelength of 532 nm was used as the light source. Similar to the previous study, this light source was likely chosen to provide fast imaging as well as provide a wavelength that is primary absorbed by hemoglobin. The fast scanning mirror allowed a relatively large area, 2.5 mm X 2 mm, to be scanned and allowed an imaging speed of 2 Hz. The researchers reported achieving a lateral resolution of 5 μm and a maximum imaging depth of 540 μm. The research team demonstrated the abilities of this platform by imaging the blood vessels under a cuticle in human skin, and a red mole on a healthy volunteer's leg. The authors noted that this device could be used for intraoperative assessment of cancer margins.

The third platform, reported by Park *et al*. (2017), consisted of a similar setup, using a scanner to raster the excitation light and acoustic detection column across the sample [98]. They were able to produce a small probe, which was circular in shape and had a diameter of 17 mm and length of 31 mm. The team constructed a waterproof, compact scanning mirror, which allowed for its integration into a small probe. The ultrasound transducer used had a central frequency of 50 MHz, and the platform had an axial resolution of 12 μm and lateral resolution of 30 μm. The probe has a maximum field of view of 2.8 mm X 2 mm. Light was supplied using a Q-switched diode-pumped solid-state laser operating at 532 nm and a repetition rate of 50 kHz. The authors noted that the slow imaging speed, 20 s per volumetric frame, could be improved by using a laser with a faster repetition rate and by redesigning the mirror to allow faster scanning. To demonstrate the

utility of their platform in human imaging, the team imaged a mole on a volunteer's finger. The authors explain that this imaging platform could be best applied to imaging and diagnosing melanomas.

2.3 Discussion

Recently published papers on hand-held OAI platforms show that OACT has, by far, become the most advanced technology in the OAI modality suite. Multiple off-the-shelf systems are available from iThera Medical and VisualSonics, with many being used in research and clinical studies. The utility of OACT platforms has been further broadened by the development of dual-modality US-OACT imaging systems [75]. There are, however, ways that current platforms could be improved. As previously described, the main limitation with OACT platforms is that piezoelectric transducers used are opaque, blocking any path of laser light to tissue directly underneath the transducer while the transducer is in direct contact with the tissue. While some modifications have been developed to overcome this problem, they do not allow for the full imaging capabilities of the linear transducer arrays to be realized. Some preliminary work has been conducted that uses waveguides to deliver light to samples directly underneath the transducer, minimizing the size of the spacer [112]. This minimizes the reduction of the transducers' FOV when a spacer is included, therefore improving the resulting image quality. Alternatively, bench-top OACT platforms utilizing FPI have been developed, demonstrating transparent acoustic detectors, but these have yet to be translated into a hand-held platform [107, 113]. Existing OAI platforms are also limited by the need for many transducer elements to create real-time, two-dimensional and three-dimensional images, complicating instrumentation [1]. In order to simplify platforms, acoustic delay lines are being investigated to allow one

transducer to detect ultrasound signals from several positions in the tissue [84, 90]. This allows for OACT to be accomplished using much simpler setups.

With regards to OMi platforms, OR-OMi has received more attention than AR-OMi based on literature counts of published studies. Authors of recently published papers in OR-OMi note that the chief limitation in the method is the speed of the scanning mirror [80]. As further improvements are made to OR-OMi platforms, clinical application is just around the corner.

Lastly, OMe (RSOM) is a relatively recent addition to the OAI modality suite, but presents a powerful method of imaging structures on the micron scale, rivaling the resolving power of hand-held OR-OMi while producing images from greater depths within tissue. So far, only two hand-held platforms have been developed, but as other applications are explored, more are sure to come.

A major current limitation in OAI is compensating for variable light fluence throughout the region of interest. optoacoustic signal strength is proportional to the optical absorption of the tissue and the local fluence. In tissue, fluence can vary greatly, making signals originating from deep in the tissue appear weak [74]. This can obscure deep structures. Zhao *et al.* (2017) used a finite element method to model fluence within breast tissue, and used this to compensate for fluence in optoacoustic images of breast vasculature. The weakness of this solution is that if the optical properties of the tissue deviate from the assumed properties in the model, the measured values could be inaccurate. This problem becomes even more complicated in spectroscopic imaging. This is due to the dependence of fluence on both depth and the wavelength of light used. Incorrectly compensated signals can greatly affect the accuracy of spectrally resolved components [35]. Recently, Tzoumas

et al. (2015) demonstrated the use of 'eigenspectra MSOT', a previously unexplored method, which is based upon the idea that a few base spectra can be used to predict fluence in tissues with arbitrarily varying optical properties [35]. They demonstrated that this technique can be used to reduce the error in measuring oxygen saturation in deep tissues by 3-8 fold in comparison with more common linear fitting models.

Another limitation for OAI platforms is device cost. Many OAI devices use OPOs, dye-based lasers, or Nd:YAG lasers, all of which are expensive [8]. Commercial systems can cost close to one million dollars [114].

Despite these current limitations, OAI is continuously being applied in new areas. For example, Zhou, Liang, and Wang (2016) demonstrated the use of a hand-held OACT platform in *in vivo* blood flowmetry in humans [79]. The authors note that this information can be used in the diagnoses and treatment of diseases such as stroke and atherosclerosis. Another exciting front in OAs is the detection of circulating tumor cells (CTCs). Labeled CTCs have been successfully detected *in vivo* in mice, as well as melanoma CTCs, whose melanin content serves as an endogenous contrast agent [29]. There have also been studies that have detected and captured *in vitro* CTCs [115]. Here, human blood was mixed with breast cancer cells, tagged using an exogenous agent, and isolated using a benchtop setup.

Intraoperative imaging is another emerging area where OAI is being applied. For instance, it has been noted that OAI could be used to assess blood perfusion in the colon or esophagus during surgery [29, 116]. This information could be used to fix anastomotic leakage while surgery is being performed. Additionally, a pilot study demonstrated the use of OAI during surgery on the prostate [101]. The results of the study indicate that a dual modality US-OACT platform could be used during prostrate surgery to help surgeons

visualize critical tissues. In other applications, US-OACT (US-MSOT) was used to image, *in vivo*, sentinel lymph nodes marked with a contrast agent [102]. The pilot study, which involved 20 patients, demonstrated for the first time that the method could identify metastasis of melanoma in lymph nodes with 100% sensitivity, which demonstrated the significant impact such a device could have on diagnosis and treatment.

The use of dual-modality hybrid AR-OR-OAMi platforms has also been explored, and was used to visualize changes in tissue caused by low level laser radiation [117]. The authors note that this system could be incorporated into feedback control system of medical procedures, making them safer and more effective. The use of dual modality OACT-OCT is also being demonstrated [71]. Zabihian *et al.* (2015) used a portable OACT-OCT system to visualize several skin pathologies.

Lastly, although many endogenous contrast agents can be used in OAI studies, the use of exogenous contrast agents is an area of important study. Common examples include gold and carbon nanoparticles, small molecule dyes, and organic nanostructures [118]. 'Smart' contrast agents, whose optical properties are altered by biological processes *in vivo* and can be used to monitor such processes, and are an exciting area of growth. Jathoul *et al.* (2015) demonstrated the use of generating an optoacoustic contrast agent *in vivo* using the enzyme tyrosinase (Tyr) [106]. In the cell, Tyr forms eumelanin from tyrosine, which is a broadband absorber well suited as a optoacoustic contrast agent. In the study, the team imaged the growth of genetically engineered cells, which expressed Tyr and were injected into nude mice, using a FPI system. This is just one illustrative example [118].

Clearly, the potential impact of hand-held OAI platforms in the clinic is high. OAI can provide a wealth of diagnostic information when treating diseases and conditions such

as melanoma tumors [73], breast cancer [33], thyroid cancer [75], and burns [81]. This information could improve the accuracy of diagnoses, aid in early detection of disease, assist surgeons, and improve patient outcomes. In translating OAI methods from benchtop platforms to hand-held platforms, this technology becomes a much more practical clinical tool that will be able to be more widely used for research and patient care [37, 71].

2.4 Bibliography

[1] L. Wang, J. Yao, A Practical Guide to Photoacoustic Tomography in the Life Sciences, Nature Methods 13(8) (2016) 11.

[2] S. Manohar, D. Razansky, Photoacoustics: a historical review, Adv. Opt. Photon. 8(4) (2016) 586-617.

[3] A. Miklós, P. Hess, Z. Bozóki, Application of acoustic resonators in photoacoustic trace gas analysis and metrology, Review of Scientific Instruments 72(4) (2001) 1937-1955.

[4] J.A. Rogers, A.A.M. and, M.J. Banet, K.A. Nelson, Optical Generation and Characterization of Acoustic Waves in Thin Films: Fundamentals and Applications, Annual Review of Materials Science 30(1) (2000) 117-157.

[5] a. S Malkin, O. Canaani, The Use and Characteristics of the Photoacoustic Method in the Study of Photosynthesis, Annual Review of Plant Physiology and Plant Molecular Biology 45(1) (1994) 493-526.

[6] P. Beard, Biomedical photoacoustic imaging, Interface Focus 1(4) (2011) 602-631.

[7] Y. Zhou, J. Yao, L.V. Wang, Tutorial on photoacoustic tomography, J. of Biomedical

Optics 21(6) (2016) 14.

[8] P.K. Upputuri, M. Pramanik, Recent advances toward preclinical and clinical translation of photoacoustic tomography: a review, J. of Biomedical Optics 22(4) (2016) 041006.

[9] M. Xu, L.V. Wang, Photoacoustic imaging in biomedicine, Review of Scientific Instruments 77(4) (2006) 041101.

[10] A.N.S. Institute, American National Standard for the Safe Use of Lasers in Health Care Facilities: Standard Z136.1-2000, ANSI, Inc., New York, 2000.

[11] L.V. Wang, Prospects of photoacoustic tomography, Medical Physics 35(12) (2008) 5758-5767.

[12] V. Ntziachristos, Going deeper than microscopy: the optical imaging frontier in biology, Nature Methods 7 (2010) 603.

[13] Jerry L. Prince, J.M. Links, Medical Imaging Signals and Systems, Person Prentice Hall, USA, 2006.

[14] Y. Zhou, W. Xing, K.I. Maslov, L.A. Cornelius, L.V. Wang, Handheld photoacoustic microscopy to detect melanoma depth in vivo, Opt. Lett. 39(16) (2014) 4731-4734.

[15] M. Heijblom, D. Piras, M. Brinkhuis, J.C.G. van Hespen, F.M. van den Engh, M. van der Schaaf, J.M. Klaase, T.G. van Leeuwen, W. Steenbergen, S. Manohar, Photoacoustic image patterns of breast carcinoma and comparisons with Magnetic Resonance Imaging and vascular stained histopathology, Scientific Reports 5 (2015) 11778.

[16] S.J. Ford, P.L. Bigliardi, T.C.P. Sardella, A. Urich, N.C. Burton, M. Kacprowicz, M. Bigliardi, M. Olivo, D. Razansky, Structural and Functional Analysis of Intact Hair Follicles and Pilosebaceous Units by Volumetric Multispectral Optoacoustic Tomography, Journal of Investigative Dermatology 136(4) (2016) 753-761.

[17] J. Aguirre, B. Hindelang, A. Bereznhoi, U. Darsow, F. Lauffer, K. Eyerich, T. Biedermann, V. Ntziachristos, Assessing nailfold microvascular structure with ultra-wideband raster-scan optoacoustic mesoscopy, Photoacoustics 10 (2018) 31-37.

[18] J. Aguirre, M. Schwarz, N. Garzorz, M. Omar, A. Buehler, K. Eyerich, V. Ntziachristos, Precision assessment of label-free psoriasis biomarkers with ultra-broadband optoacoustic mesoscopy, Nature Biomedical Engineering 1 (2017) 0068.

[19] C. Kim, E.C. Cho, J. Chen, K.H. Song, L. Au, C. Favazza, Q. Zhang, C.M. Cobley, F. Gao, Y. Xia, L.V. Wang, In vivo molecular photoacoustic tomography of melanomas targeted by bio-conjugated gold nanocages, ACS nano 4(8) (2010) 4559-4564.

[20] L.V. Wang, S. Hu, Photoacoustic Tomography: In Vivo Imaging from Organelles to Organs, Science 335(6075) (2012) 1458-1462.

[21] M. Moothanchery, M. Pramanik, Performance Characterization of a Switchable Acoustic Resolution and Optical Resolution Photoacoustic Microscopy System, Sensors 17(2) (2017) 357.

[22] E. Héctor, T. Jake, K. Moritz, R. Daniel, Real-time optoacoustic brain microscopy with hybrid optical and acoustic resolution, Laser Physics Letters 11(4) (2014) 045601.

[23] M. Omar, J. Gateau, V. Ntziachristos, Raster-scan optoacoustic mesoscopy in the 25-125 MHz range, Opt. Lett. 38(14) (2013) 2472-2474.

[24] M. Omar, M. Schwarz, D. Soliman, P. Symvoulidis, V. Ntziachristos, Pushing the Optical Imaging Limits of Cancer with Multi-Frequency-Band Raster-Scan Optoacoustic Mesoscopy (RSOM), Neoplasia (New York, N.Y.) 17(2) (2015) 208-214.

[25] M. Omar, D. Soliman, J. Gateau, V. Ntziachristos, Ultrawideband reflection-mode optoacoustic mesoscopy, Opt. Lett. 39(13) (2014) 3911-3914.

[26] J. Aguirre, M. Schwarz, D. Soliman, A. Buehler, M. Omar, V. Ntziachristos, Broadband mesoscopic optoacoustic tomography reveals skin layers, Opt. Lett. 39(21) (2014) 6297-6300.

[27] X.X. Xueding Wang, Geng Ku, Lihong V. Wang, George Stoica, Noninvasive imaging of hemoglobin concentration and oxygenation in the rat brain using high-resolution photoacoustic tomography, J. of Biomedical Optics 11(2) (2006) 024015.

[28] S. Sethuraman, J.H. Amirian, S.H. Litovsky, R.W. Smalling, S.Y. Emelianov, Spectroscopic intravascular photoacoustic imaging to differentiate atherosclerotic plaques, Optics Express 16(5) (2008) 3362-3367.

[29] A. Taruttis, V. Ntziachristos, Advances in real-time multispectral optoacoustic imaging and its applications, Nature Photonics 9 (2015) 219.

[30] B. Xie, M.R. Tomaszewski, A.A. Neves, S. Ros, D.-E. Hu, S. McGuire, S.R. Mullins, D. Tice, R.C.A. Sainson, S.E. Bohndiek, R.W. Wilkinson, K.M. Brindle, Optoacoustic

Detection of Early Therapy-Induced Tumor Cell Death Using a Targeted Imaging Agent, Clinical Cancer Research 23(22) (2017) 6893-6903.

[31] M. Tomaszewski, I. Gonzalez, J. O'Connor, O. Abeyakoon, G. Parker, K. Williams, F. Gilbert, S. Bohndiek, Oxygen Enhanced Optoacoustic Tomography (OE-OT) Reveals Vascular Dynamics in Murine Models of Prostate Cancer, Theranostics 7(11) (2017) 2900-2913.

[32] F. Knieling, C. Neufert, A. Hartmann, J. Claussen, A. Urich, C. Egger, M. Vetter, S. Fischer, L. Pfeifer, A. Hagel, C. Kielisch, R.S. Görtz, D. Wildner, M. Engel, J. Röther, W. Uter, J. Siebler, R. Atreya, W. Rascher, D. Strobel, M.F. Neurath, M.J. Waldner, Multispectral Optoacoustic Tomography for Assessment of Crohn's Disease Activity, New England Journal of Medicine 376(13) (2017) 1292-1294.

[33] G. Diot, S. Metz, A. Noske, E. Liapis, B. Schroeder, S.V. Ovsepian, R. Meier, E. Rummeny, V. Ntziachristos, Multispectral Optoacoustic Tomography (MSOT) of Human Breast Cancer, Clinical Cancer Research 23(22) (2017) 6912-6922.

[34] A. Becker, M. Masthoff, J. Claussen, S.J. Ford, W. Roll, M. Burg, P.J. Barth, W. Heindel, M. Schäfers, M. Eisenblätter, M. Wildgruber, Multispectral optoacoustic tomography of the human breast: characterisation of healthy tissue and malignant lesions using a hybrid ultrasound-optoacoustic approach, European Radiology 28(2) (2017) 602-609.

[35] S. Tzoumas, A. Nunes, I. Olefir, S. Stangl, P. Symvoulidis, S. Glasl, C. Bayer, G. Multhoff, V. Ntziachristos, Eigenspectra optoacoustic tomography achieves quantitative

blood oxygenation imaging deep in tissues, Nature Communications 7 (2016) 12121.

[36] A. Taruttis, A.C. Timmermans, P.C. Wouters, M. Kacprowicz, G.M.v. Dam, V. Ntziachristos, Optoacoustic Imaging of Human Vasculature: Feasibility by Using a Handheld Probe, Radiology 281(1) (2016) 256-263.

[37] V. Neuschmelting, N.C. Burton, H. Lockau, A. Urich, S. Harmsen, V. Ntziachristos, M.F. Kircher, Performance of a Multispectral Optoacoustic Tomography (MSOT) System equipped with 2D vs. 3D Handheld Probes for Potential Clinical Translation, Photoacoustics 4(1) (2016) 1-10.

[38] A. Dima, V. Ntziachristos, In-vivo handheld optoacoustic tomography of the human thyroid, Photoacoustics 4(2) (2016) 65-69.

[39] I. Stoffels, M. Petri, S. Morscher, N. Burton, D. Schadendorf, M. Gunzer, J. Klode, Clinical application of noninvasive and nonradioactive determination of microscopic lymph node tumor status by multispectral optoacoustic imaging, J Nucl Med 57(no. supplement 2) (2016).

[40] M. Schwarz, A. Buehler, J. Aguirre, V. Ntziachristos, Three-dimensional multispectral optoacoustic mesoscopy reveals melanin and blood oxygenation in human skin in vivo, Journal of Biophotonics 9(1-2) (2016) 55-60.

[41] B.T. Cox, J.G. Laufer, P.C. Beard, S.R. Arridge, Quantitative spectroscopic photoacoustic imaging: a review, J. of Biomedical Optics, SPIE, 2012.

[42] X.L. Dean-Ben, S. Gottschalk, B. Mc Larney, S. Shoham, D. Razansky, Advanced

optoacoustic methods for multiscale imaging of in vivo dynamics, Chemical Society Reviews 46(8) (2017) 2158-2198.

[43] K.J. Francis, B. Chinni, S.S. Channappayya, R. Pachamuthu, V.S. Dogra, N. Rao, Characterization of lens based photoacoustic imaging system, Photoacoustics 8 (2017) 37-47.

[44] Diagnostic Ultrasound Physics and Equipment, Second ed., Cambridge University Press, USA, 2010.

[45] Y. Wang, D. Wang, Y. Zhang, J. Geng, J.F. Lovell, J. Xia, Slit-enabled linear-array photoacoustic tomography with near isotropic spatial resolution in three dimensions, Opt. Lett. 41(1) (2016) 127-130.

[46] X. Luís Deán-Ben, D. Razansky, Adding fifth dimension to optoacoustic imaging: volumetric time-resolved spectrally enriched tomography, Light: Science & Applications 3 (2014) e137.

[47] L.V. Wang, H. Wu, Biomedical Optics: Principles and Imaging, Wiley2007.

[48] P. Hajireza, W. Shi, K. Bell, R.J. Paproski, R.J. Zemp, Non-interferometric photoacoustic remote sensing microscopy, Light: Science & Applications 6 (2017) e16278.

[49] J. Yao, K.I. Maslov, Y. Zhang, Y. Xia, L.V. Wang, Label-free oxygen-metabolic photoacoustic microscopy in vivo, J. of Biomedical Optics 16(7) (2011) 076003.

[50] C. Zhang, K. Maslov, L.V. Wang, Subwavelength-resolution label-free photoacoustic microscopy of optical absorption in vivo, Opt. Lett. 35(19) (2010) 3195-3197.

[51] R.A. Kruger, C.M. Kuzmiak, R.B. Lam, D.R. Reinecke, S.P. Del Rio, D. Steed, Dedicated 3D photoacoustic breast imaging, Medical Physics 40(11) (2013) 113301.

[52] R.A. Kruger, R.B. Lam, D.R. Reinecke, S.P. Del Rio, R.P. Doyle, Photoacoustic angiography of the breast, Medical Physics 37(11) (2010) 6096-6100.

[53] L. Nie, S. Wang, X. Wang, P. Rong, Y. Ma, G. Liu, P. Huang, G. Lu, X. Chen, In Vivo Volumetric Photoacoustic Molecular Angiography and Therapeutic Monitoring with Targeted Plasmonic Nanostars, Small 10(8) (2014) 1585-1593.

[54] L. Xiang, B. Wang, L. Ji, H. Jiang, 4-D Photoacoustic Tomography, Scientific Reports 3 (2013) 1113.

[55] J.G. Laufer, E.Z. Zhang, B.E. Treeby, B.T. Cox, P.C. Beard, P. Johnson, B. Pedley, In vivo preclinical photoacoustic imaging of tumor vasculature development and therapy, J. of Biomedical Optics 17(5) (2012) 056016.

[56] E. Herzog, A. Taruttis, N. Beziere, A.A. Lutich, D. Razansky, V. Ntziachristos, Optical Imaging of Cancer Heterogeneity with Multispectral Optoacoustic Tomography, Radiology 263(2) (2012) 461-468.

[57] J. Tang, J.E. Coleman, X. Dai, H. Jiang, Wearable 3-D Photoacoustic Tomography for Functional Brain Imaging in Behaving Rats, Scientific Reports 6 (2016) 25470.

[58] X.L. Deán-Ben, G. Sela, A. Lauri, M. Kneipp, V. Ntziachristos, G.G. Westmeyer, S. Shoham, D. Razansky, Functional optoacoustic neuro-tomography for scalable whole-brain monitoring of calcium indicators, Light: Science & Applications 5 (2016) e16201.

[59] J. Yao, L. Wang, J.-M. Yang, K.I. Maslov, T.T.W. Wong, L. Li, C.-H. Huang, J. Zou, L.V. Wang, High-speed label-free functional photoacoustic microscopy of mouse brain in action, Nature Methods 12 (2015) 407.

[60] J. Yao, J. Xia, K.I. Maslov, M. Nasiriavanaki, V. Tsytsarev, A.V. Demchenko, L.V. Wang, Noninvasive photoacoustic computed tomography of mouse brain metabolism in vivo, NeuroImage 64(Supplement C) (2013) 257-266.

[61] P. Hai, J. Yao, K.I. Maslov, Y. Zhou, L.V. Wang, Near-infrared optical-resolution photoacoustic microscopy, Opt. Lett. 39(17) (2014) 5192-5195.

[62] C. Kim, T.N. Erpelding, L. Jankovic, L.V. Wang, Performance benchmarks of an array-based hand-held photoacoustic probe adapted from a clinical ultrasound system for non-invasive sentinel lymph node imaging, Philosophical Transactions: Mathematical, Physical and Engineering Sciences 369(1955) (2011) 4644-4650.

[63] W.J. Akers, C. Kim, M. Berezin, K. Guo, R. Fuhrhop, G.M. Lanza, G.M. Fischer, E. Daltrozzo, A. Zumbusch, X. Cai, L.V. Wang, S. Achilefu, Non-invasive Photoacoustic and Fluorescence Sentinel Lymph Node Identification using Dye-loaded Perfluorocarbon Nanoparticles, ACS nano 5(1) (2011) 173-182.

[64] S. Jiao, M. Jiang, J. Hu, A. Fawzi, Q. Zhou, K.K. Shung, C.A. Puliafito, H.F. Zhang, Photoacoustic ophthalmoscopy for in vivo retinal imaging, Optics Express 18(4) (2010) 3967-3972.

[65] J. Xia, M.R. Chatni, K.I. Maslov, Z. Guo, K. Wang, M.A. Anastasio, L.V. Wang, Whole-body ring-shaped confocal photoacoustic computed tomography of small animals

in vivo, J. of Biomedical Optics 17(5) (2012) 050506.

[66] J. Zhang, S. Yang, X. Ji, Q. Zhou, D. Xing, Characterization of Lipid-Rich Aortic Plaques by Intravascular Photoacoustic Tomography: Ex Vivo and In Vivo Validation in a Rabbit Atherosclerosis Model With Histologic Correlation, Journal of the American College of Cardiology 64(4) (2014) 385-390.

[67] A. Buehler, M. Kacprowicz, A. Taruttis, V. Ntziachristos, Real-time handheld multispectral optoacoustic imaging, Opt. Lett. 38(9) (2013) 1404-1406.

[68] X.L. Dean-Ben, A. Ozbek, D. Razansky, Volumetric Real-Time Tracking of Peripheral Human Vasculature With GPU-Accelerated Three-Dimensional Optoacoustic Tomography, IEEE Transactions on Medical Imaging 32(11) (2013) 2050-2055.

[69] A. Dima, V. Ntziachristos, Non-invasive carotid imaging using optoacoustic tomography, Optics Express 20(22) (2012) 25044-25057.

[70] J. Xia, J. Yao, L.V. Wang, Photoacoustic tomography: principles and advances, Electromagnetic waves 147 (2014) 1-22.

[71] B. Zabihian, J. Weingast, M. Liu, E. Zhang, P. Beard, H. Pehamberger, W. Drexler, B. Hermann, In vivo dual-modality photoacoustic and optical coherence tomography imaging of human dermatological pathologies, Biomedical Optics Express 6(9) (2015) 3163-3178.

[72] A. Hariri, J. Lemaster, J. Wang, A. Jeevarathinam, K. S., D.L. Chao, J.V. Jokerst, The characterization of an economic and portable LED-based photoacoustic imaging system to

facilitate molecular imaging, Photoacoustics 9 (2018) 10-20.

[73] Y. Zhou, S.V. Tripathi, I. Rosman, J. Ma, P. Hai, G.P. Linette, M.L. Council, R.C. Fields, L.V. Wang, L.A. Cornelius, Noninvasive Determination of Melanoma Depth using a Handheld Photoacoustic Probe, Journal of Investigative Dermatology 137(6) (2017) 1370-1372.

[74] L. Zhao, M. Yang, Y. Jiang, C. Li, Optical fluence compensation for handheld photoacoustic probe: An in vivo human study case, Journal of Innovative Optical Health Sciences 10(4) (2017) 1740002.

[75] M. Yang, L. Zhao, X. He, N. Su, C. Zhao, H. Tang, T. Hong, W. Li, F. Yang, L. Lin, B. Zhang, R. Zhang, Y. Jiang, C. Li, Photoacoustic/ultrasound dual imaging of human thyroid cancers: an initial clinical study, Biomedical Optics Express 8(7) (2017) 3449-3457.

[76] K. Park, J.Y. Kim, C. Lee, G. Lim, C. Kim, Development of a photoacoustic handheld probe using 2-axis MEMS scanner, SPIE BiOS, SPIE, San Francisco, California, United States, 2017, p. 100641N.

[77] A. Karlas, J. Reber, G. Diot, D. Bozhko, M. Anastasopoulou, T. Ibrahim, M. Schwaiger, F. Hyafil, V. Ntziachristos, Flow-mediated dilatation test using optoacoustic imaging: a proof-of-concept, Biomedical Optics Express 8(7) (2017) 3395-3403.

[78] A.B.E. Attia, S.Y. Chuah, D. Razansky, C.J.H. Ho, P. Malempati, U.S. Dinish, R. Bi, C.Y. Fu, S.J. Ford, J.S.-S. Lee, M.W.P. Tan, M. Olivo, S.T.G. Thng, Noninvasive real-time characterization of non-melanoma skin cancers with handheld optoacoustic probes,

Photoacoustics 7 (2017) 20-26.

[79] Y. Zhou, J. Liang, L.V. Wang, Cuffing-based photoacoustic flowmetry in humans in the optical diffusive regime, Journal of Biophotonics 9(3) (2016) 208-212.

[80] L. Lin, P. Zhang, S. Xu, J. Shi, L. Li, J. Yao, L. Wang, J. Zou, L.V. Wang, Handheld optical-resolution photoacoustic microscopy, J. of Biomedical Optics 22(4) (2016) 041002.

[81] T. Ida, H. Iwazaki, Y. Kawaguchi, S. Kawauchi, T. Ohkura, K. Iwaya, H. Tsuda, D. Saitoh, S. Sato, T. Iwai, Burn depth assessments by photoacoustic imaging and laser Doppler imaging, Wound Repair and Regeneration 24(2) (2015) 349-355.

[82] P. Hai, Y. Zhou, R. Zhang, J. Ma, Y. Li, J.-Y. Shao, L.V. Wang, Label-free high-throughput detection and quantification of circulating melanoma tumor cell clusters by linear-array-based photoacoustic tomography, J. of Biomedical Optics 22(4) (2016) 041004.

[83] X.L. Deán-Ben, T.F. Fehm, M. Gostic, D. Razansky, Volumetric hand-held optoacoustic angiography as a tool for real-time screening of dense breast, Journal of Biophotonics 9(3) (2016) 253-259.

[84] Y. Cho, C.C. Chang, L.V. Wang, J. Zou, Micromachined silicon parallel acoustic delay lines as time-delayed ultrasound detector array for real-time photoacoustic tomography, Journal of Optics 18(2) (2016) 024003.

[85] Y. Zhou, G. Li, L. Zhu, C. Li, L.A. Cornelius, L.V. Wang, Handheld photoacoustic probe to detect both melanoma depth and volume at high speed in vivo, Journal of

Biophotonics 8(11-12) (2015) 961-967.

[86] P.K. Upputuri, M. Pramanik, Performance characterization of low-cost, high-speed, portable pulsed laser diode photoacoustic tomography (PLD-PAT) system, Biomedical Optics Express 6(10) (2015) 4118-4129.

[87] A. Garcia-Uribe, T.N. Erpelding, A. Krumholz, H. Ke, K. Maslov, C. Appleton, J.A. Margenthaler, L.V. Wang, Dual-Modality Photoacoustic and Ultrasound Imaging System for Noninvasive Sentinel Lymph Node Detection in Patients with Breast Cancer, Scientific Reports 5 (2015) 15748.

[88] K. Daoudi, P.J.v.d. Berg, O. Rabot, A. Kohl, S. Tisserand, P.J. Brands, W. Steenbergen, Handheld probe integrating laser diode and ultrasound transducer array for ultrasound/photoacoustic dual modality imaging, Optics Express 22(21) (2014).

[89] X.L. Deán-Ben, E. Bay, D. Razansky, Functional optoacoustic imaging of moving objects using microsecond-delay acquisition of multispectral three-dimensional tomographic data, Scientific Reports 4 (2014) 5878.

[90] Y. Cho, C.-C. Chang, J. Yu, M. Jeon, C. Kim, L.V. Wang, J. Zou, Handheld photoacoustic tomography probe built using optical-fiber parallel acoustic delay lines, Journal of Biomedical Optics 19(8) (2014) 086007.

[91] H. Yang, L. Xi, S. Samuelson, H. Xie, L. Yang, H. Jiang, Handheld miniature probe integrating diffuse optical tomography with photoacoustic imaging through a MEMS scanning mirror, Biomedical Optics Express 4(3) (2013) 427-432.

[92] A. Needles, A. Heinmiller, J. Sun, C. Theodoropoulos, D. Bates, D. Hirson, M. Yin, F.S. Foster, Development and initial application of a fully integrated photoacoustic micro-ultrasound system, IEEE Transactions on Ultrasonics, Ferroelectrics, and Frequency Control 60(5) (2013) 888-897.

[93] X.L. Deán-Ben, D. Razansky, Functional optoacoustic human angiography with handheld video rate three dimensional scanner, Photoacoustics 1(3-4) (2013) 68-73.

[94] X.L. Deán-Ben, D. Razansky, Portable spherical array probe for volumetric real-time optoacoustic imaging at centimeter-scale depths, Optics Express 21(23) (2013) 28062-28071.

[95] P. Hajireza, W. Shi, R.J. Zemp, Real-time handheld optical-resolution photoacoustic microscopy, Optics Express 19(21) (2011) 20097-20102.

[96] L. Xi, J. Sun, Y. Zhu, L. Wu, H. Xie, H. Jiang, Photoacoustic imaging based on MEMS mirror scanning, Biomedical Optics Express 1(5) (2010) 1278-1283.

[97] J.J. Niederhauser, M. Jaeger, R. Lemor, P. Weber, M. Frenz, Combined ultrasound and optoacoustic system for real-time high-contrast vascular imaging in vivo, IEEE Transactions on Medical Imaging 24(4) (2005) 436-440.

[98] K. Park, J.Y. Kim, C. Lee, S. Jeon, G. Lim, C. Kim, Handheld Photoacoustic Microscopy Probe, Scientific Reports 7(1) (2017) 13359.

[99] K. Sivasubramanian, V. Periyasamy, M. Pramanik, Non-invasive sentinel lymph node mapping and needle guidance using clinical handheld photoacoustic imaging system in

small animal, Journal of Biophotonics (2017) 201700061.

[100] T. Ida, Y. Kawaguchi, S. Kawauchi, K. Iwaya, H. Tsuda, D. Saitoh, S. Sato, T. Iwai, Real-time photoacoustic imaging system for burn diagnosis, J. of Biomedical Optics, SPIE, 2014, p. 7.

[101] A. Horiguchi, K. Tsujita, K. Irisawa, T. Kasamatsu, K. Hirota, M. Kawaguchi, M. Shinchi, K. Ito, T. Asano, H. Shinmoto, H. Tsuda, M. Ishihara, A pilot study of photoacoustic imaging system for improved real-time visualization of neurovascular bundle during radical prostatectomy, The Prostate 76(3) (2016) 307-315.

[102] I. Stoffels, S. Morscher, I. Helfrich, U. Hillen, J. Leyh, N.C. Burton, T.C.P. Sardella, J. Claussen, T.D. Poeppel, H.S. Bachmann, A. Roesch, K. Griewank, D. Schadendorf, M. Gunzer, J. Klode, Metastatic status of sentinel lymph nodes in melanoma determined noninvasively with multispectral optoacoustic imaging, Science Translational Medicine 7(317) (2015) 317ra199-317ra199.

[103] A. Rosenthal, V. Ntziachristos, D. Razansky, Acoustic Inversion in Optoacoustic Tomography: A Review, Current Medical Imaging Reviews 9(4) (2013) 318-336.

[104] N.A. Rejesh, H. Pullagurla, M. Pramanik, Deconvolution-based deblurring of reconstructed images in photoacoustic/thermoacoustic tomography, Journal of the Optical Society of America A 30(10) (2013) 1994-2001.

[105] E. Zhang, J. Laufer, P. Beard, Backward-mode multiwavelength photoacoustic scanner using a planar Fabry-Perot polymer film ultrasound sensor for high-resolution three-dimensional imaging of biological tissues, Appl. Opt. 47(4) (2008) 561-577.

[106] A.P. Jathoul, J. Laufer, O. Ogunlade, B. Treeby, B. Cox, E. Zhang, P. Johnson, A.R. Pizzey, B. Philip, T. Marafioti, M.F. Lythgoe, R.B. Pedley, M.A. Pule, P. Beard, Deep in vivo photoacoustic imaging of mammalian tissues using a tyrosinase-based genetic reporter, Nature Photonics 9 (2015) 239.

[107] N. Huynh, O. Ogunlade, E. Zhang, B. Cox, P. Beard, Photoacoustic imaging using an 8-beam Fabry-Perot scanner, SPIE BiOS, SPIE, 2016, p. 97082L.

[108] Y. Wang, C. Li, R.K. Wang, Noncontact photoacoustic imaging achieved by using a low-coherence interferometer as the acoustic detector, Opt. Lett. 36(20) (2011) 3975-3977.

[109] C. Buj, M. Münter, B. Schmarbeck, J. Horstmann, G. Hüttmann, R. Brinkmann, Noncontact holographic detection for photoacoustic tomography, J. of Biomedical Optics 22(10) (2017) 106007.

[110] A. Dima, N.C. Burton, V. Ntziachristos, Multispectral optoacoustic tomography at 64, 128, and 256 channels, J. of Biomedical Optics 19(3) (2014) 036021.

[111] J.-T. Oh, M.-L. Li, H.F. Zhang, K.I. Maslov, L.V. Wang, Three-dimensional imaging of skin melanoma in vivo by dual-wavelength photoacoustic microscopy, J. of Biomedical Optics 11(3) (2006) 034032.

[112] M.W. Schellenberg, P.J.D. Whiteside, H.K. Hunt, Planar waveguide light transmission modality for backward-mode photoacoustic tomography, SPIE BiOS, SPIE, 2016, p. 97083O.

[113] R. Ellwood, O. Ogunlade, E. Zhang, P. Beard, B. Cox, Photoacoustic tomography

using orthogonal Fabry–Pérot sensors, J. of Biomedical Optics 22(4) (2016) 041009.

[114] B. Hawkins, Vevo LAZR-X, in: M.W. Schellenberg (Ed.) 2018.

[115] K. Bhattacharyya, B.S. Goldschmidt, J.A. Viator, Detection and capture of breast cancer cells with photoacoustic flow cytometry, J. of Biomedical Optics, SPIE, 2016, p. 9.

[116] A. Taruttis, G.M. van Dam, V. Ntziachristos, Mesoscopic and Macroscopic Optoacoustic Imaging of Cancer, Cancer Res. 75(8) (2015) 1548-1559.

[117] E. Héctor, S. Emil, B. Olga, R. Daniel, Hybrid optoacoustic and ultrasound biomicroscopy monitors' laser-induced tissue modifications and magnetite nanoparticle impregnation, Laser Physics Letters 11(12) (2014) 125601.

[118] J. Weber, P.C. Beard, S.E. Bohndiek, Contrast agents for molecular photoacoustic imaging, Nature Methods 13 (2016) 639.

Chapter 3

Technical Discussion

This chapter is meant to provide insight into the technical aspects of the project. These include optical waveguides, the optoacoustic effect, the imaging method used, and how images were analyzed.

3.1 Optical Waveguides

To understand how light is confined within a waveguide, is it important to understand how light acts at an interface between two optically different materials. At a boundary between two materials with different refractive indexes, light can either refract, travel along the boundary, or reflect from the interface. These three basic interactions can be seen in Figure 3.1.

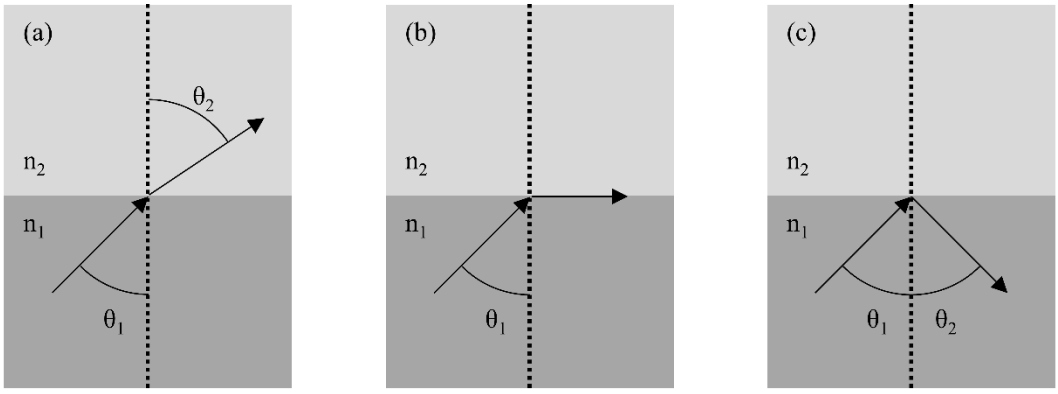

Figure 3.1. The three basic interactions light can have at the boundary of two materials with different refractive indices. **(a)** Refraction, where light is refracted into the second medium. **(b)** Light travels along the boundary between the two materials **(c)** Reflection, where light is reflected back into the first medium.

Waveguides are designed to confine light within their boundaries by causing light within them to reflect of their boundaries. Confinement within an optical waveguide can

be described using Snell's Law, seen in Equation 3.1.

$$n_1 \sin\theta_1 = n_2 \sin\theta_2 \tag{3.1}$$

Here, n_1 is the refractive index of the media from which the light originates, and θ_1 is the incidence angle of the light upon the boundary. This incidence angle is defined as the angle between the boundary normal and the ray of incident light. Similarly, n_2 is the refractive index of the second media at the interface, and θ_2 is the angle of refraction. The angle of refraction is defined as the angle of the refracted beam relative the interface normal. The incident beam is reflected when $\theta_2 = 1$, and the incidence angle at which is happens in known as the critical angle θ_c. The critical angle, which is characteristic of the two materials which make up the interface, can be calculated by Equation 3.2 if the refractive indexes of both media are known.

$$\theta_c = \sin^{-1}\left({}^{n_2}/_{n_1}\right) \tag{3.2}$$

The material chosen for the waveguides, poly(methyl methacrylate) (PMMA), has a refractive index of 1.49 for light with a wavelength of 532 nm [1]. In order to ensure that light wound be confined over a large range of incidence angles, silver was chosen as the cladding material, which has a refractive index of 0.05 for light with a wavelength of 532 nm [2]. This results in a critical angle of 1.92°, which means any incidence angle greater than 1.92° will result in reflection. As mentioned earlier, the waveguide confines light until the light reaches the active area, which is devoid of silver cladding. A typical value for the refractive index of epidermis tissue, the topmost layer of the skin, is 1.44, leading to a critical angle at the active area interface of 75.11° when it is in contact with skin tissue [3]. The waveguides were designed so that light entering them had a 45° incidence angle upon the cladding. This allowed for easy fabrication, reflection at the PMMA-silver boundary,

and refraction at the PMMA-tissue boundary. A more rigorous derivation of the equations that govern waveguides can be found in Ref. [4].

Optical waveguides were used for light delivery because they allowed for the space between the sensor and the tissue being imaged to be minimized while illuminating the sample directly underneath the sensor. This was desirable because it allows for direct illumination of the imaging plane, reducing image artifacts, while keeping the sensor close to the signal sources, improving imaging depth and image contrast. These optical waveguides were engineered to confine light within their boundaries until the light had reached a designated point, hereafter referred to as the 'active area'.

3.2 The Optoacoustic Effect

The optoacoustic effect describes the phenomena of mechanical wave (sound) generation due to light absorption. When light is absorbed, it is partially converted into heat, and this causes the absorber to thermoelastically expand. This relationship between thermal expansion and pressure generation can be derived using the following method [5-7].

First, an equation describing force within the medium is derived. This starts with a 1-dimensional equation describing the force exerted on some volume, given in Equation 3.3.

$$F = -\left(\partial p / \partial x\right) dx\, dy\, dz \tag{3.3}$$

Here, F is force, p is pressure, and x is the position. Using Newton's Second Law, this can be described using Equation 3.4.

$$-\left(\partial p / \partial x\right) = \rho\left(\partial u / \partial t\right) \tag{3.4}$$

Here, ρ is density of the medium, u is the velocity of the medium, and t is time.

The change in velocity with respect to time can be rewritten to describe the change in position, resulting in Equation 3.5.

$$-\left({}^{\partial p}/_{\partial x}\right) = \rho\left({}^{\partial^2 x}/_{\partial t^2}\right) \tag{3.5}$$

Equation 3.5 can be generalized for 3-dimensional space, and replacing position with displacement, to yield Equation 3.6.

$$-\nabla p(\vec{r},t) = \rho\left({}^{\partial^2}/_{\partial t^2}\right)\vec{\xi}(\vec{r},t) \tag{3.6}$$

Here, ξ is displacement. We now turn to the fractional volume thermal expansion (Equation 3.7), which relates heating of a medium to some volume change.

$${}^{dV}/_{V} = -\kappa p + \beta T \tag{\#.7}$$

Here V represents volume, κ is the isothermal compressibility, p is the change of pressure within the medium, β is the thermal coefficient of volume expansion, and T is the change of temperature within the medium. This can be generalized for spherical space, also with respect to time, resulting in Equation 3.8.

$$\nabla \cdot \vec{\xi}(\vec{r},t) = -\kappa p(\vec{r},t) + \beta T(\vec{r},t) \tag{3.8}$$

We now have two equations describing displacement. One describes it in terms of pressure change, the other in temperature change. In order to combine these, the divergence of Equation 3.6 is taken:

$$-\nabla^2 p(\vec{r},t) = \rho\left({}^{\partial^2}/_{\partial t^2}\right)\left[\nabla \cdot \vec{\xi}(\vec{r},t)\right] \tag{3.9}$$

We can substitute Equation 3.8 into Equation 9, resulting in the general optoacoustic equations, Equations 3.10 and 3.11. Equation 3.11 is most commonly used.

$$-\nabla^2 p(\vec{r},t) = \rho\left({}^{\partial^2}/_{\partial t^2}\right)\left[-\kappa p(\vec{r},t) + \beta T(\vec{r},t)\right] \tag{3.10}$$

$$\left(-\nabla^2 + \rho\kappa\, {\partial^2}/{\partial t^2}\right) p(\vec{r},t) = \rho\beta\, {\partial^2 T(\vec{r},t)}/{\partial t^2} \qquad \text{(Rearrange)}$$

$$\rho = {1}/{c^2\kappa} \qquad \text{(Definition of } \rho\text{)}$$

$$\left(-\nabla^2 + \rho\kappa\, {\partial^2}/{\partial t^2}\right) p(\vec{r},t) = \left({\beta}/{c^2\kappa}\right)\left({\partial^2 T(\vec{r},t)}/{\partial t^2}\right) \qquad \text{(Sub. in, 3.11)}$$

In the general equation, the left-hand side describes optoacoustic wave propagation, and the right-hand side describes optoacoustic wave generation. Here, c is the speed of sound. We now turn to the constraints of optoacoustic wave generation, which are the thermal relaxation time and stress relaxation time. Thermal relaxation describes thermal diffusion from the absorbing particle due to light absorption, and for optoacoustic wave generation thermal diffusion must be negligible. Therefore, heat deposition must happen on a time scale in which thermal diffusion is negligible, called thermal confinement. The time in which heat deposition must occur can be calculated using Equation 3.12.

$$\tau_{th} = {d_c^2}/{\alpha_{th}} \qquad (3.12)$$

Here, τ_{th} is the thermal relaxation time, d_c is the characteristic dimension of the heated region, and α_{th} is the thermal diffusivity of the medium. Stress relaxation describes the propagation pressure, and for optoacoustic wave generation, pressure prorogation must be negligible. This is termed stress confinement. The time in while heat deposition, which causes a pressure rise, must occur can be described using Equation 3.13.

$$\tau_s = {d_c}/{c} \qquad (3.13)$$

Here, τ_s is the stress relaxation time and c is the speed of sound in the medium. These confinement times have implications on the resolution of an optoacoustic imaging system. The light source used provides a limit on the resolution of the system based on its pulse length. The finest resolvable feature can be calculated by solving for d_c in both

equations, where the largest value for d_c is taken as the resolution, and substituting pulse length for τ_s and τ_{th}.

We now turn back to the general optoacoustic equation. In thermal confinement, heating due to light absorption can be described using Equation 3.14.

$$\rho C_V \, {\partial T(\vec{r},t)}/{\partial t} = H(\vec{r},t) \tag{3.14}$$

$${\partial T(\vec{r},t)}/{\partial t} = {H(\vec{r},t)}/{\rho C_V} \tag{Rearrange}$$

Here, C_V is the specific heat capacity at constant volume, and H describes heating as a function of optical absorption and fluence, defined as heat per unit volume per unit time. H can be described using Equation 3.15.

$$H = \eta_{th}\mu_a\Phi \tag{3.15}$$

Here, Φ is the optical fluence, μ_a is the optical absorption, and η_{th} is the ratio of absorbed energy converted into heat. We can substitute Equation 3.14. into Equation 3.11. to yield a less-general optoacoustic equation (Equation 3.16,), which can be simplified into Equation 3.17.

$$\left(-\nabla^2 + \rho\kappa\, {\partial^2}/{\partial t^2}\right) p(\vec{r},t) = \left({\beta}/{c^2\kappa}\right)\left({1}/{C_V}\right)\left({\partial H(\vec{r},t)}/{\partial t}\right) \tag{3.16}$$

$$\kappa = {C_P}/{\rho c^2 C_V} \tag{Definition of } \kappa)$$

$$\left(-\nabla^2 + \rho\kappa\, {\partial^2}/{\partial t^2}\right) p(\vec{r},t) = \left({\beta}/{C_P}\right)\left({\partial H(\vec{r},t)}/{\partial t}\right) \tag{Sub. in, 3.17}$$

Here, C_P is the specific heat capacity at constant pressure.

3.3 Delay-And-Sum Image Formation

The image-forming algorithm used in the study is based upon the concept of Delay-And-Sum (DAS) beamforming. In DAS, a delay is applied to each sensor of an array to 'focus'

the array to a point within the imaging plane (Figure 3.2) [8, 9].

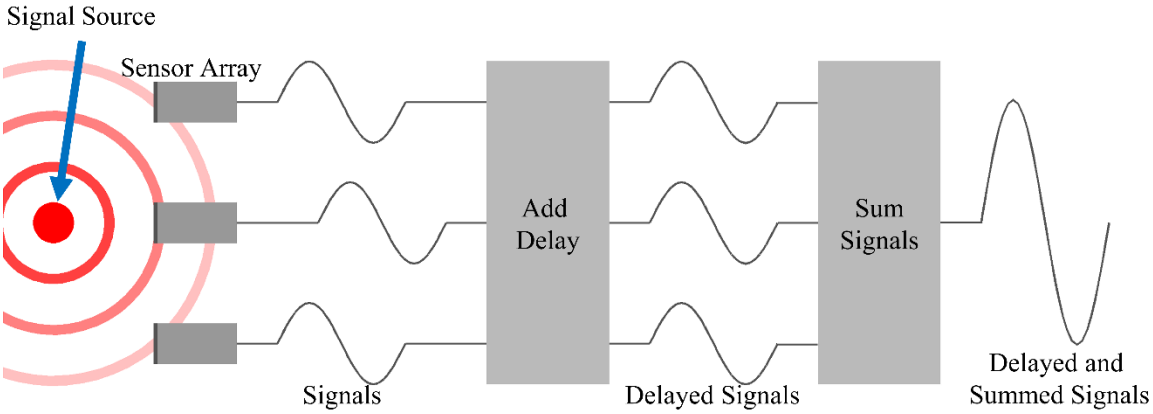

Figure 3.2. Schematic of Delay-And-Sum signal processing. The OA signals from the source (red) are detected by an array of sensors. A delay is added to each signal depending on the distance between the sensor and the point of interest on the imaging plane. Here the point of interest is at the signal source. Then the delayed signals are summed. This process is repeated for every point on the imaging plane, and the amplitude of the DAS signals is recorded in an array with their positions within the array corresponding to their positions on the imaging plane.

The delay is based off the distance between the sensor and the point of interest as well as the speed of sound within the medium. In 2-dimensions, defining the location of the transducer as $\vec{s} = [x_s, y_s]$, the location of the acoustic source as $\vec{a} = [x_a, y_a]$, and the speed of sound within the medium as c, the delay d_s can be calculated using Equation 3.18.

$$d_s = \frac{\sqrt{(x_a - x_s)^2 + (y_a - y_s)^2}}{c} \tag{3.18}$$

After the delay is applied, the signals detected by the transducers are then summed. The result is that signals originating from the point of interest constructively interfere with each other. Using an array made of S transducers, each with a temporally recorded signal w_s, the output of the DAS algorithm is:

$$DAS = \sum_{s=0}^{S-1} w_s(t - d_s) \tag{3.19}$$

Here, DAS is the amplitude of the DAS signal from the point on the imaging plane being investigated, t is time, and d_s is the delay for a particular signal.

The quality of images made using DAS can be improved by using the signal coherence factor (CF) [8, 10]. Signals originating outside of where the DAS beamformer is focused are not rejected in a simple DAS algorithm and can contribute to image artifacts. CF weighing can be used to alleviate this problem. The CF ranges from 0 to 1, depending on the coherence of the delayed signals, which is shown in Figure 3.3. The coherence between two signals accounts for how in phase the signals are. When the signals are perfectly coherent, their phases are matched, and the value is one. The CF is defined as:

$$CF = \frac{\left|\sum_{s=0}^{S-1} w_s(t-d_s)\right|^2}{\sum_{s=0}^{S-1}|w_s(t-d_s)|^2} \tag{3.20}$$

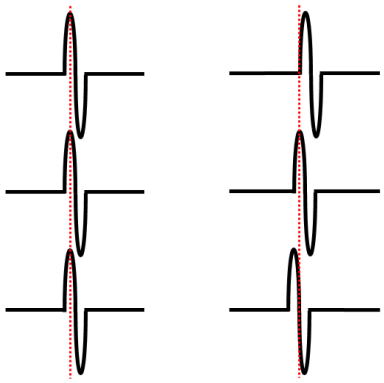

Figure 3.3. [Left] The delayed signals are properly focused on the source, here to CF would be 1. [Right] The delayed signals are not properly focused on the source, here the CF would be <1.

This value of the summed signals at each point on the imaging plane is simply multiplied by the CF evaluated at that point.

3.4 Image Analysis

Optoacoustic imaging systems can be evaluated by analyzing the images they produce. There are several methods to do this, which are described in Section 2, and here, we will

use two of these methods: measuring the resolution of the system and determining the contrast to noise ratio for a deep burn tissue phantom. The methods used to determine these characteristics are described in the following sub-sections.

3.4.1 Resolution

The resolution of an imaging system can be determined by either imaging a point source, or by subtracting the know dimensions of the imaged structure from the dimensions determined via imaging [5, 11]. For imaging a point source, the dimensions of the point source must be at least several times smaller than the theoretical maximum resolution of the imaging system. Due to imperfections, inherent in any system, the point source will appear blurred in the image, and the distribution of the intensity in the image can be analyzed (Figure 3.4). The intensity of the image along the direction in which in resolution is being tested (i.e. axial, lateral) is taken, resulting in a curve called the point spread function (PSF). The full-width at half-maximum (FWHM) of the PSF is taken to be the resolution.

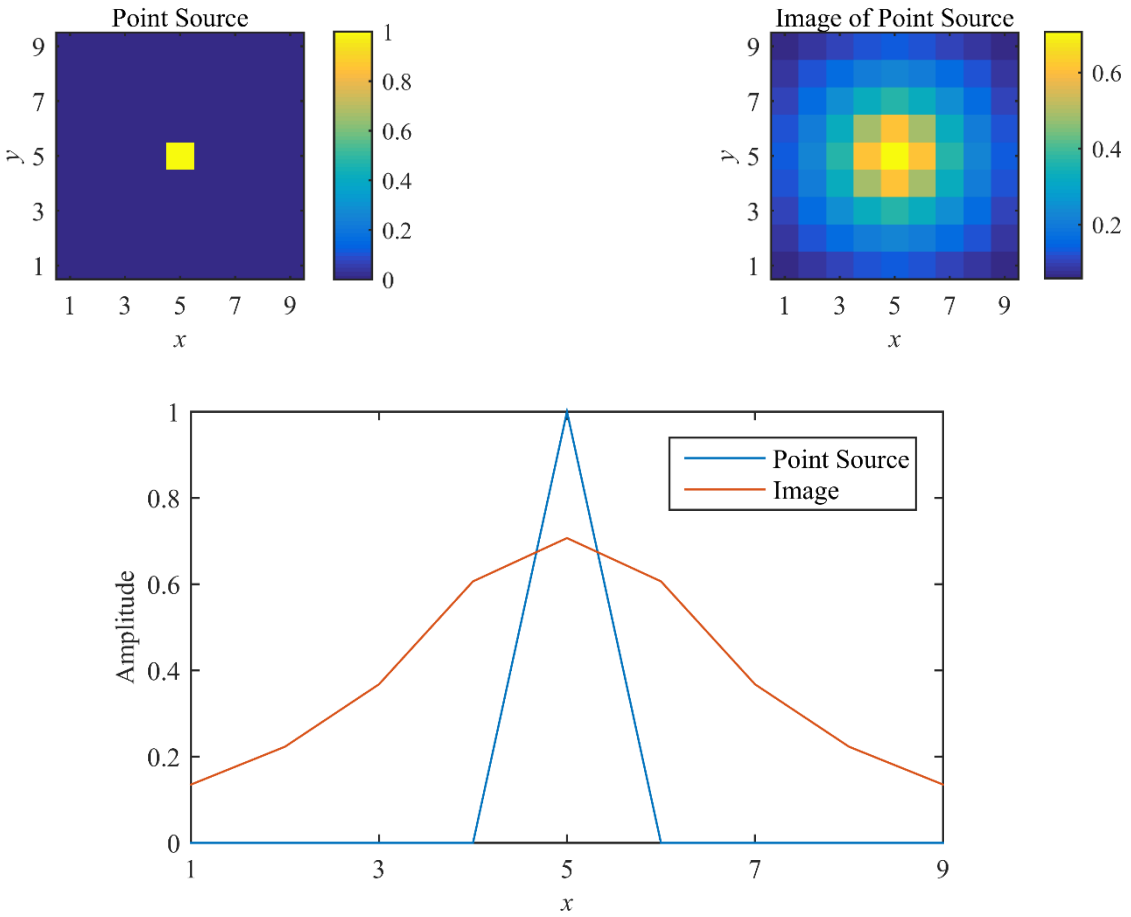

Figure 3.4. **[Top Left]** A point source within a 2D image plane. **[Top Right]** An image made from the point source. Due to imperfections of this example imaging system, the point source is blurred. **[Bottom]** The PSF of both the point source and the image made of the point source along the *x* axis. The FWHM of the image PSF can be taken as the resolution.

An alternative method can be used if the dimensions of the source object are comparable to the theoretical maximum resolution of the imaging platform [11]. This method begins quite similarly to the one previously described, using the intensity of the image along the direction in which in resolution is being tested (Figure 3.5). Then, the width of the peak is measured, and the measured length of the object is subtracted to calculate the resolution.

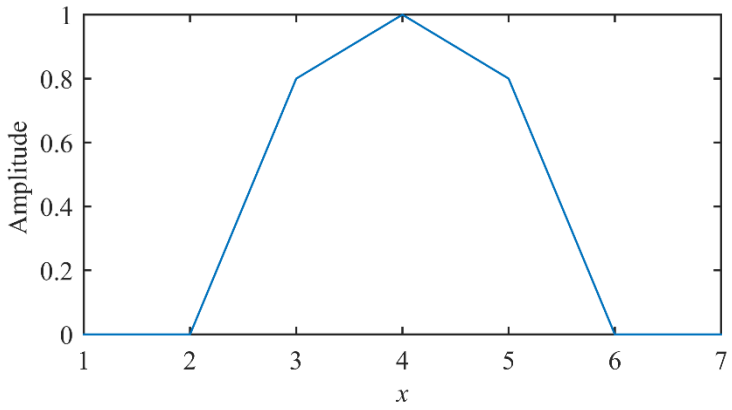

Figure 3.5. Here, the intensity of the images structure is taken along the *x* axis. Because the dimensions of the imaged structure are comparable to the resolution of the system, the size of the actual structure can be subtracted from the size determined by the image to determine the resolution. Here, the width at the base of the peak is 4. If we know the actual size of the structure to be 3, the solution of the system is 1. Units are arbitrary.

3.4.2 Contrast to Noise Ratio

The clarity of an image is commonly evaluated using the contrast to noise ratio (CRN) [5]. This can be defined using Equation 3.21.

$$CNR = {\Delta I}/{\sigma_I} \tag{3.21}$$

Here, ΔI represents the intensity in the region of interest minus any background intensity, and σ_I is the standard deviation of the background intensity.

3.4 Summary

Here, we have described the technical aspects related to the project. Waveguides are used because the can be engineered to selectively contain to release light at an interface. By selecting appropriate materials for the waveguide bulk and cladding, it is possible to produce a waveguide that will confine light until it is in contact with the sample of interest.

Once light is delivered to the sample, and both thermal and stress confinement conditions are met, OA waves are generated. This is based on of the transient heating of absorbers which leads to thermal expansion and finally the generation of an OA wave.

This OA wave can be detected and recorded using an array of sensors. The recorded signals then can be used to generate an image using DAS image formation techniques. DAS image formation focuses the array to different point on the imaging plane by applying appropriate delays to the individual signals and then summing the results. This causes signals originating from the focal point to constructively interfere, and the amplitude of this is recorded.

The generated image is then analyzed to evaluate the imaging platform used to gather the data. Analysis includes determine the resolution of the imaging system as well as the CRN. Resolution is the measure of how finely the platform can resolve structures. CNR is an indication of the contrast of the region of interest (ROI), with high CNRs indicating that the ROI is easy to identify.

3.5 Bibliography

[1] N. Sultanova, S. Kasarova, I. Nikolov, Dispersion Properties of Optical Polymers, Proceedings of the International School and Conference on Photonics, PHOTONICA09, ACTA PHYSICA POLONICA A, 2009, pp. 585-587.

[2] P.B. Johnson, R.W. Christy, Optical Constants of the Noble Metals, Physical Review B 6(12) (1972) 4370-4379.

[3] D. Huafeng, Q.L. Jun, A.W. William, J.K. Peter, H. Xin-Hua, Refractive indices of human skin tissues at eight wavelengths and estimated dispersion relations between 300 and 1600 nm, Physics in Medicine & Biology 51(6) (2006) 1479.

[4] P.J.D. Whiteside, Photonic Ablation via Quantum Tunneling Biological Engineering University of Missouri, Columbia, Columbia, Missouri, 2015, p. 153.

[5] L.V. Wang, H. Wu, Biomedical Optics: Principles and Imaging, Wiley2007.

[6] L.V. Wang, Tutorial on Photoacoustic Microscopy and Computed Tomography, IEEE Journal of Selected Topics in Quantum Electronics 14(1) (2008) 171-179.

[7] Y. Zhou, J. Yao, L.V. Wang, Tutorial on photoacoustic tomography, J. of Biomedical Optics 21(6) (2016) 14.

[8] S. Park, A.B. Karpiouk, S.R. Aglyamov, S.Y. Emelianov, Adaptive beamforming for photoacoustic imaging, Opt. Lett. 33(12) (2008) 1291-1293.

[9] J. Grythe, Beamforming algorithms - beamformers, Squarehead Technology AS 2016.

[10] C.K. Liao, M.L. Li, P.C. Li, Optoacoustic imaging with synthetic aperture focusing and coherence weighting, Opt. Lett. 29(21) (2004) 2506-2508.

[11] K. Geng, W. Xueding, S. George, V.W. Lihong, Multiple-bandwidth photoacoustic tomography, Physics in Medicine & Biology 49(7) (2004) 1329.

Chapter 4

Development and Characterization of a Handheld, Waveguide-Mediated, Optoacoustic Imaging Probe

In this chapter, we discuss the design of all components, programs, and algorithms used in this study, including the tissue phantoms, waveguides, electrical components, optical systems, the hand-held probe, and testing setups used. Then, we present the programs and algorithms used for data acquisition, image formation, and the simulation of photon transport in skin tissue to evaluate the illumination of a transducer from the side. Lastly, we present the data acquired during the course of this investigation.

4.1 Research Methodology

Visual inspection, the current standard to assessing burn wound severity, lacks accuracy, with only 2/3 burns being correctly diagnosed [1]. This is partly because it is a qualitative method. Therefore, more quantitative methods must be explored in order to improve burn assessment accuracy. One promising method is OAI, which has been recently been explored for burn wound depth analysis in animal models [2, 3]. This method determines burn wound depth by visualizing the outer boundary of the burn, which is characterized by inflammation and hyperperfusion. In the images, contrast is based on light absorption by hemoglobin in blood, making it possible to identify the boundary layer.

While OAI has great potential in assisting burn wound diagnosis, some technical challenges remain such as light delivery. In hand-held OAI, opaque piezoelectric transducers are used as sensors, complicating light delivery to the target tissue. While multiple techniques have been used to work around this, limitations remain. In this work we use optical waveguides to deliver light the tissue phantoms directly beneath a sensor array, improving performance. Using this technique, it is possible to develop a compact, hand-held OACT platform that is well suited for imaging burn wounds.

For this study, the presented OACT platform is evaluated using two separate testing setups. This was done to evaluate both the theoretically optimal imaging characteristics of the waveguide-transducer pair and the realized imaging characteristics of the presented hand-held platform (Figures 4.1 and 4.2). One setup used simple forward mode OACT (not hand-held), where the laser energy is delivered on the opposite side of the tissue phantom as the transducer array. In the second setup, the hand-held device was used, where light was delivered to the same side of the tissue phantom as the transducer array (backward mode).

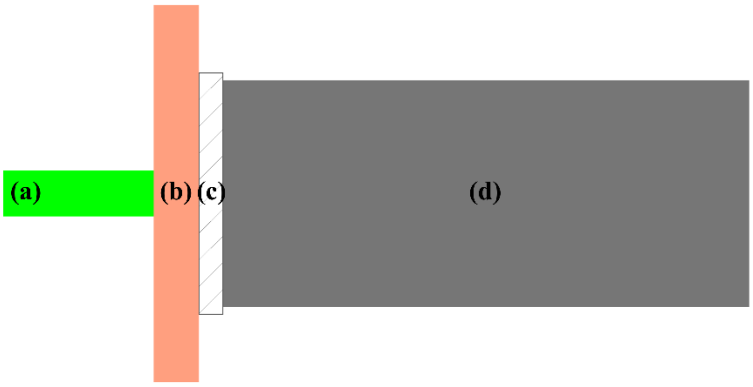

Figure 4.1. Schematic showing the forward mode imaging setup used in this study. Here, a laser **(a)** is fired toward a tissue phantom **(b)**. The transducer **(d)** is placed on the opposite side of the tissue phantom as the incident laser light. Here, a piece of the material the waveguide was made out of its placed between the tissue phantom and the transducer to simulate the presence of a waveguide **(c)**.

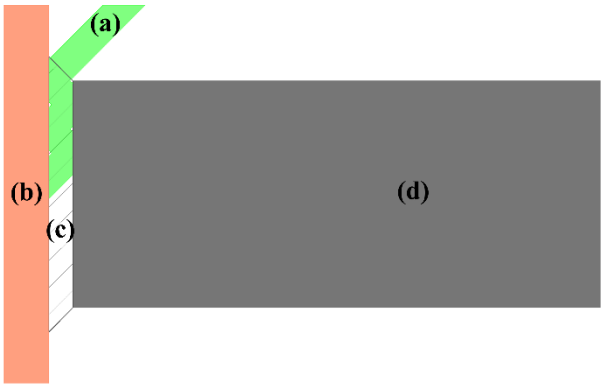

Figure 4.2. A basic schematic of how the transducer **(d)**, tissue **(b)**, and waveguide **(c)** are orientated during testing with the hand-held platform. Here, the laser light **(a)** is coupled into the waveguide, which contains the light until it is underneath the transducer. At this point, the light is allowed to couple out of the waveguide and into the tissue.

This was done because high energies could not be delivered to the probe, owing to a limit in the amount of energy capable of being transferred via the optical fiber that was used to deliver light to the probe. Future designs should incorporate optical fibers that can carry enough energy to deliver up to 20 mJ/cm^2 to the sample surface. The forward mode setup was designed to evaluate the possible imaging capabilities of the device should the optical system be able to deliver more energy to the waveguide. This setup was used to evaluate the setup's lateral and axial resolution as well as to demonstrate imaging of a burn wound tissue phantom. In the hand-held setup a tissue phantom that contained little absorption in the bulk material and a strongly absorbing OA target was used. This allowed for imaging at reduced laser energies.

In all tests, the laser used was a Quantel Brilliant Nd:YAG laser that had a pulse length of 5 ns, was operated at a wavelength of 532 nm, and output vertically polarized light in a circular Gaussian beam. All 3D printed parts were made using a printer in-house (FlashForge Creator Pro) using acrylonitrile butadiene styrene (3D ABS-1kg1.75-WHT, Hatchbox).

4.1.1 Tissue Phantom Design and Fabrication

Three different tissue phantoms types were used in this study. The first was used to determine the lateral and axial resolution of the system, the second to demonstrate imaging of a burn wound tissue phantom, and the third was used to demonstrate the imaging capabilities of the hand-held probe. All phantoms were made using a modified protocol that had been previously reported; detailed protocols for manufacturing each tissue phantom can be found in the Appendix A [4]. Each phantom was made of DI water, methanol (A452SK, Sigma Aldrich), and gelatin (G-2500, Sigma Aldrich). When optical scattering was desired, Intralipid 20% fat emulsion (0338-1519-09, Fresenius Kabi) was included. The optical absorption coefficients of the phantoms were dependent on the concentration of gelatin and Direct Red 81 dye (DR-81, 195251, Sigma Aldrich). Gelatin provided ‘background’ absorption, while DR-81 was used to increase the optical absorption coefficient of the phantoms when needed.

4.1.1.1 Characterization of Optical Properties

The optical absorption coefficient for gelatin was first estimated by analysis of previously published results [5]. Using the published data, the molar absorption coefficient was determined for light with a wavelength of 532 nm (Table 4.1). It was found that the molar absorption coefficient was not constant over varying concentrations of gelatin at the same wavelength.

Table 4.1. Effect of gelatin concentration on molar absorption coefficient, λ = 532 nm

% w/v [g/mL]	mM	μ_a (cm^{-1})	ε_a ($1/(cm^{-1}M)$)
4%	0.533	0.056	45.593
5%	0.667	0.067	43.639
6%	0.800	0.075	40.708
8%	1.07	0.092	37.451
10%	1.33	0.109	35.497
12%	1.60	0.128	34.737

To predict the resulting molar absorption coefficient from the concentration data, the molar absorption coefficient was plotted against concentration (Figure 4.3); linear fitting was found to provide a good fit to the data (R^2 value of the fitting was 0.999) using Equation 4.1 (units in cm^{-1}) below. Here, M is the molarity of the solution.

$$\mu_a = 66.079 \cdot M + 0.0218 \tag{4.1}$$

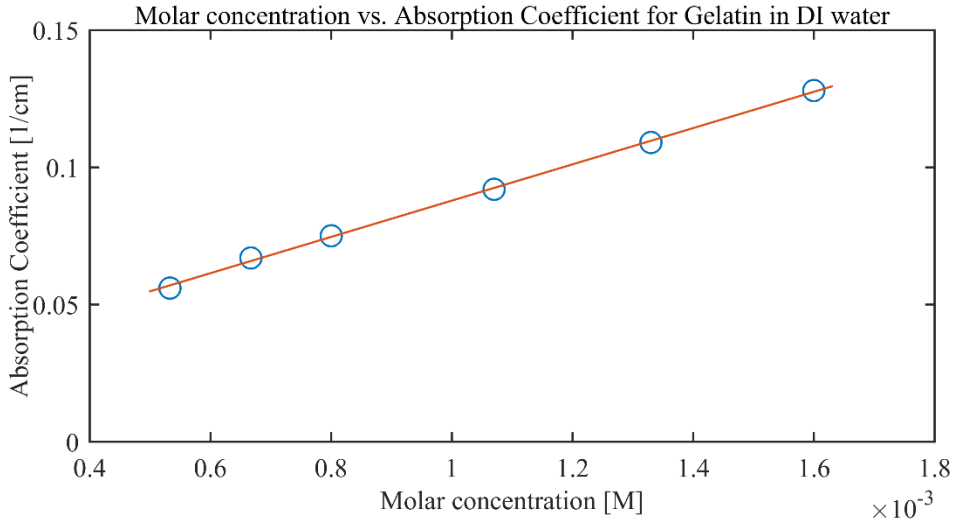

Figure 4.3. Molar concentration vs. Absorption Coefficient for gelatin in DI water at a wavelength of 532 nm. This graph shows how the absorption coefficient of gelatin in water changes with molar concentration. This method was used instead of the more common molar absorption coefficient, because this changed with varying concentrations. This absorption was taken into account when designing the tissue phantoms used in this study. Data taken from Ref. [5]. R^2 of the fitted curve is 0.999.

The preceding analysis was used to estimate the optical absorption of gelatin within the tissue phantoms. All tissue phantoms used contained 24% w/v gelatin, which, using the equation above, was predicted to have an absorption coefficient of 0.233 cm^{-1}. To test this, a solution of 24% w/v of gelatin in DI water was made and was analyzed using UV-VIS spectroscopy (UV-2401PC, Shimadzu). As shown in Figure 4.4, below, the sample had an absorption coefficient of 0.224 cm^{-1} when the wavelength 532 nm, which is within 5% of the expected value arising from Equation 4.1.

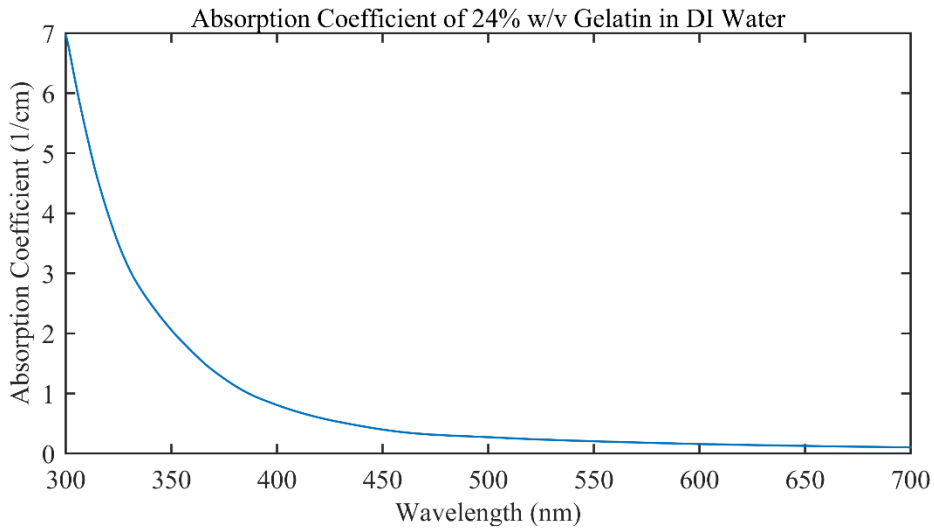

Figure 4.4. The absorption coefficient of a tissue phantom made with 24% w/v gelatin in DI water as a function of wavelength. As can be seen from the graph, the absorption coefficient at 532 nm is ~0.233 cm^{-1}, as expected.

The molar absorption coefficient of the DR-81 used was also confirmed using a solution of 7.4 μM DR-81 in DI water that was analyzed via UV-VIS spectroscopy (Figure 4.5). The molar absorption coefficient of the dye used at 532 nm was determined to be 39200 1/(cm M).

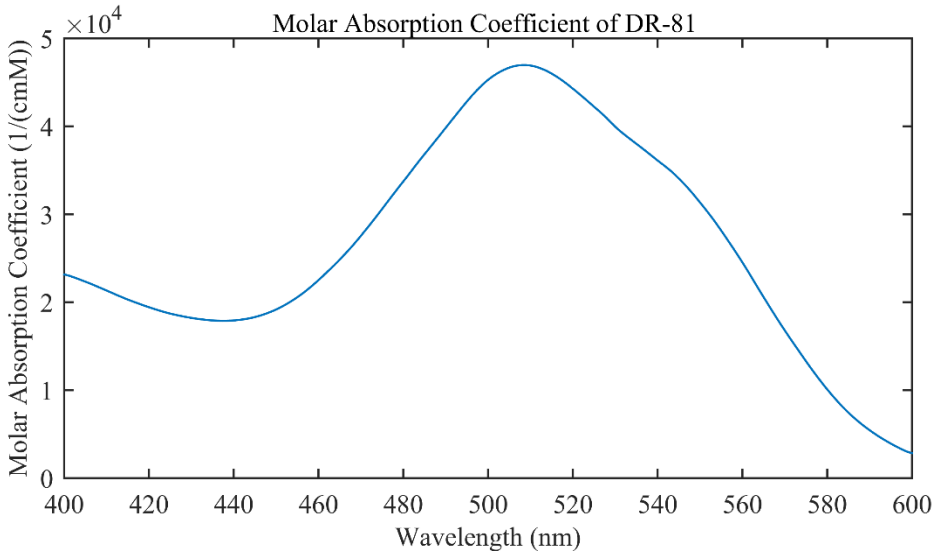

Figure 4.5. Molar absorption coefficient of Direct-Red 81 dye measured using UV-VIS spectroscopy.

4.1.1.2 Testing Tissue Phantom Speed of Sound

The speed of sound of the tissue phantom was tested. An accurate measurement of the speed of sound was essential, as this value was used in the image forming algorithm. To do this, a tissue phantom containing no dye was cast into a rectangular 3D printed mold that incorporated a transducer and optoacoustic target (Figures 4.6 and 4.7). The transducer had a central frequency of 15 MHz (V316-SU, Olympus). The transducer was connected to a digital oscilloscope (5442B, Pico Technologies) via a BNC cable. A 50 Ω feedthrough terminator (TA051, Pico Technology) was used at the connection between the BNC cable and the oscilloscope to reduce electrical noise. The target was made by creating a hole in the wall of the mold opposite the transducer, covering the hole in cellophane, and marking the cellophane with a black permanent marker. An optoacoustic signal was made by firing the laser at the target and then the time it took for the optoacoustic signal to reach the transducer was recorded. Data acquisition was initiated when the laser was fired. This was accomplished by using the output signal from the Q-switch synchro of the laser system,

which sent a high digital signal every time the laser was fired, and using this to trigger data acquisition by the oscilloscope. The trigger on the oscilloscope was set to 300 mV. To reduce the amount of noise in the received signal, 32 waveforms were taken and then averaged. The distance between the optoacoustic target and the transducer was 20.15 mm. The results of the test can be seen in Figure 4.8. The measured speed of sound was 1615 m/s.

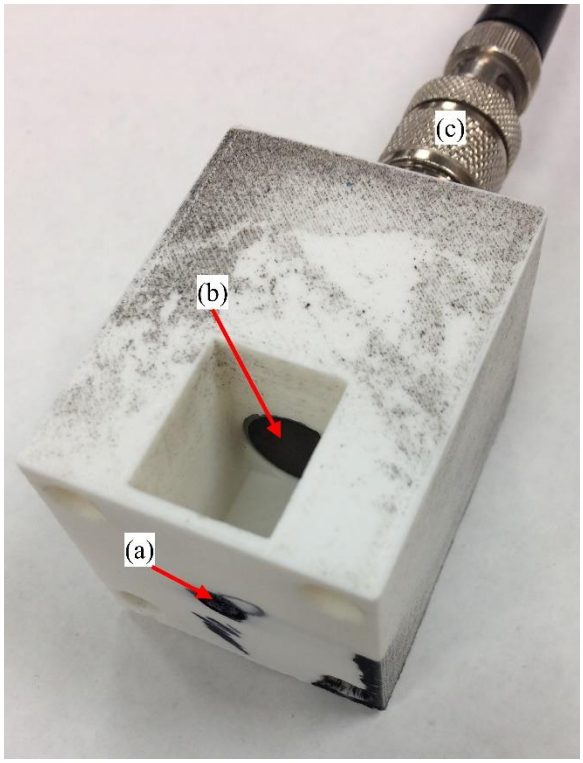

Figure 4.6. The mold used for testing the speed of sound of the tissue phantom. To test the speed of sound the laser was directed at the optoacoustic target, labeled **(a)**. This consisted of a piece of cellophane with black permanent marker on it. The transducer, **(b)**, detected the optoacoustic signal from the target. The BNC cable, labeled **(c)**, was connected to the digital oscilloscope for signal acquisition.

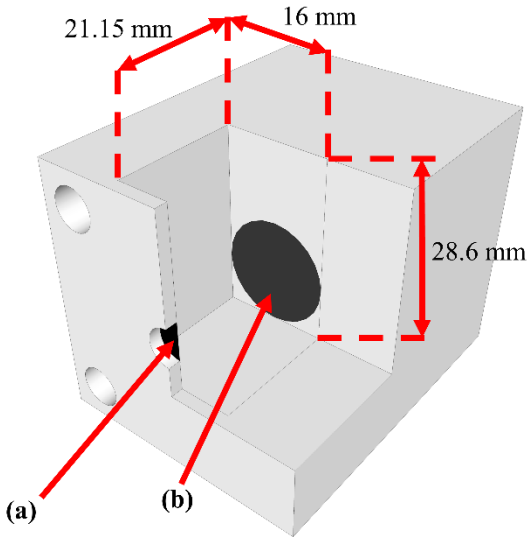

Figure 4.7. A partial cut-away schematic of the mold used for testing the speed of sound of the tissue phantom. **(a)** is the optoacoustic target, **(b)** is the face of the transducer. The dimensions of the mold are also labeled. During testing, the laser is shot at the optoacoustic target, generating an optoacoustic wave. This wave then propagates through the tissue phantom and is detected by the transducer.

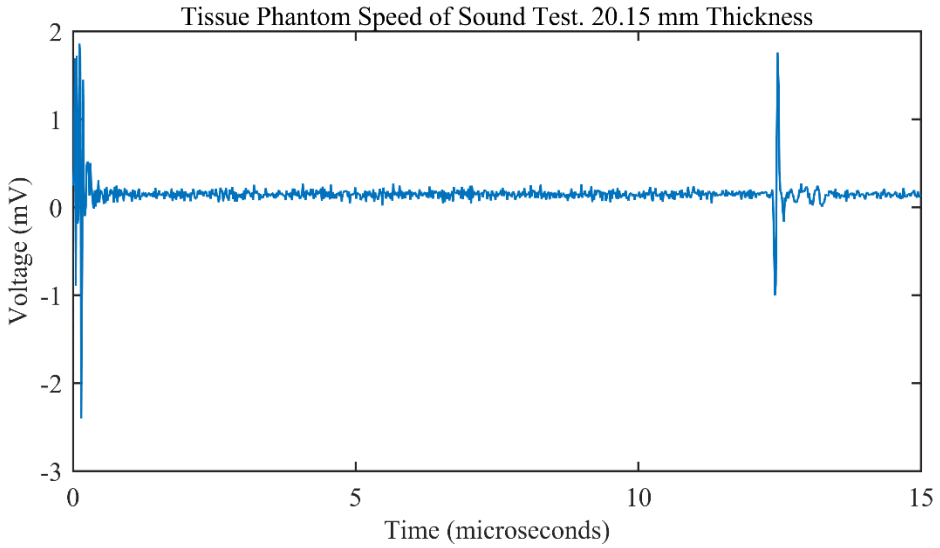

Figure 4.8. Results of the speed of sound test for the tissue phantom. 32 separate wave forms were collected and then averaged. The optoacoustic wave arrived at the transducer at 12.5 microseconds. From this the speed of sound is calculated to be 1615 m/s.

4.1.1.3 Phantom for Determining Axial and Lateral Resolution

The first type of phantom was designed to evaluate the resolution of the waveguide-transducer pair. The evaluation was performed using forward mode OACT; this

methodology allowed us to increase the signal produced by the optoacoustic target, making it easier to generate a clear image and confidently determine the resolution. Only one phantom was made, and it consisted of a tissue phantom that was absent of light-scattering or absorbing elements in the bulk and contained a human hair as an optoacoustic target. This hair was measured by optical microscopy to have a diameter of 66 μm (Figure 4.9). This was several times smaller than the maximum theoretical lateral resolution of the platform (161 μm), and comparable to the maximum theoretical lateral resolution (58 μm), as determined using the equations described in Chapter 2. Methods to determine the axial and lateral resolution and described in Chapter 3. The materials used to make the bulk phantom are found in Table 4.2. A cross-sectional schematic is found in Figure 4.10. The phantom was made using a 3D printed mold (Figure 4.11), and the hair was attached to the top of the mold using colored label tape. The mold 25 mm wide, 25 mm long, and 1 mm deep. The tissue phantom solution was then poured around the hair, filling the mold. Enough solution was added so that the hair was submerged (the solution stayed within the boundaries of the mold via surface tension).

Table 4.2. Materials used to make the bulk of the hair tissue phantom

Material	Concentration
DI water	78.5 (%v/v)
Methanol	15.3 (%v/v)
Gelatin	24 (%w/v)

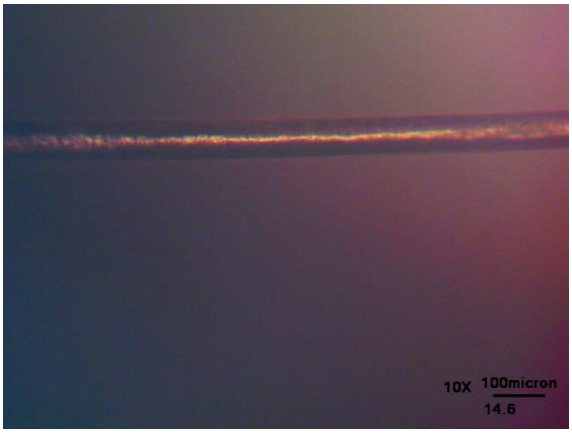

Figure 4.9. Image of hair used in resolution phantom captured using optical microscopy. The hair had a diameter of 66 μm.

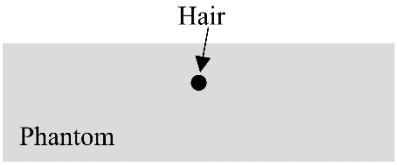

Figure 4.10. Schematic of the tissue phantom used for determining the resolution of the transducer waveguide pair. The hair was placed below the surface and had a diameter of 66 micron.

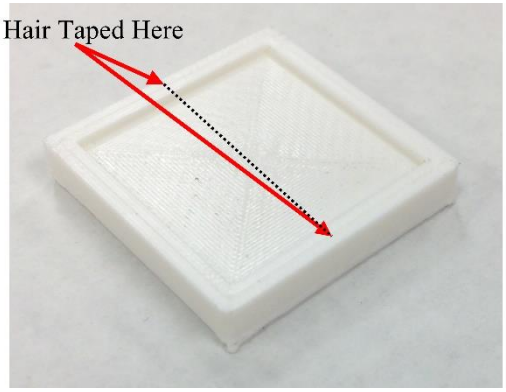

Figure 4.11. Photo of the mold used to make the tissue phantom that was used for determining the resolution of the imaging platform. Hair was taped across the mold prior the addition of the tissue phantom solution.

4.1.1.4 Phantom for Testing the Hand-Held Device

In order to demonstrate the imaging capabilities of the hand-held platform, two tissue phantoms without any absorbers or scatters in the bulk were used. They both contained a piece of black electrical tape that served as an optoacoustic target. This design was chosen

because only a relatively small amount of laser energy could be passed to the hand-held device. These phantoms were made using the materials in Table 4.2. A schematic of one the tissue phantoms is found in Figure 4.12. The phantoms were made by placing electrical tape within the mold (Figure 4.13), and then pouring the liquid phantom solution around it. Between phantoms, the electrical tape was placed at slightly different depths. These were 0.99 mm and 1.22 mm. This was done to explore if the image accuracy changed with absorber depth.

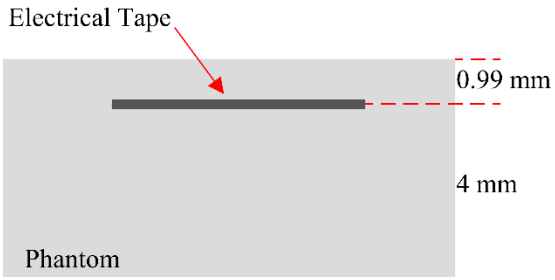

Figure 4.12. Schematic of one of the phantoms used to demonstrate the imaging capabilities of the hand-held device. The bulk contains no optical absorbers of scatters. In all phantoms, the distance from the electrical tape to the bottom of the mold was maintained at 4 mm.

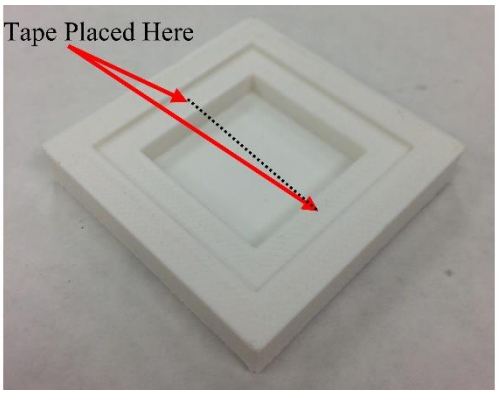

Figure 4.13. Photo of the mold used to create the tissue phantom used for evaluating the hand-held device. Electrical tape was placed across the mold.

4.1.1.5 Burn Wound Phantom

The last kind of tissue phantom that was used in the study was made to determine the

imaging capabilities of the transducer-waveguide pair for imaging a burn wound. One phantom was made, and it consisted of two different layers that were fabricated separately. The top was made of a tissue phantom that mimicked the dermis, and the bottom layer was made of a tissue phantom that mimicked the hyperemic zone that forms around burn wounds [2, 3]. As previously described, this zone is characterized by increased blood perfusion, which has been visualized using OAI. To design a phantom that accurately mimicked this hyperemic zone, data was drawn from a previous study that successfully imaged burns in swine models [3]. The authors of this study noted that the hyperemic bowl gave a signal ten times stronger than normal tissue, with the strongest signals coming from the epidermis. The authors also noted that they used pigs with low melanin content, so the tissue could be approximated as human tissue with low melanin content. For the wavelength used in the study, 584 nm, the optical absorption coefficient of epidermal tissue was 8.14 cm^{-1} [6]. For the hyperemic region in the epidermis, the optical absorption coefficient, which scales linearly with the strength of the optoacoustic signal, was ~81.4 cm^{-1}. This is equivalent to increasing to blood volume fraction to 40%. From this value, we made the generalization that all tissue in hyperemic region has a similar blood volume fraction.

The optical absorption coefficient of dermis, the tissue which the phantoms will mimic, is 0.45 cm^{-1} for light with a wavelength of 532 nm, the wavelength used in our study [6]. To approximate the optical absorption coefficient of hyperemic dermis the blood volume fraction of the tissue is increased to 40%, resulting in an absorption coefficient of 89.6 cm^{-1}. The materials used to make these phantoms can be found in Table 4.3. The healthy and hyperemic phantoms were both 2.18 mm thick. This allowed for forward OAI

to estimate backward mode OAI, as both the path length of the light and optoacoustic signals was the same. This allowed for the results to be used to evaluate if an image could be made in backwards mode imaging. Both portions of the phantom were made by casting them in identical molds (Figure 4.14).

Table 4.3. Materials used to make the healthy and hyperemic dermis tissue phantoms.

Material	Concentration	
	Healthy	Hyperemic
DI water	50 (%v/v)	50 (%v/v)
Methanol	15.3 (%v/v)	15.3 (%v/v)
Gelatin	24 (%w/v)	24 (%w/v)
Intralipid 20%	28.5 (%v/v)	28.5 (%v/v)
Dye	2.4 [μM]	990 [μM]

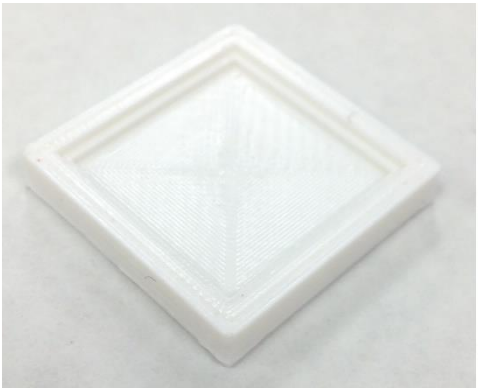

Figure 4. 14. Picture of one of the molds used to make the burn wound tissue phantom. The mold is ~2 mm deep.

4.1.2 Waveguide Design and Fabrication

The waveguide was made of poly(methyl methacrylate) (PMMA) sputter-coated with silver (Figure 4.15). This was made by first cutting a 22.4 mm by 15 mm section from a

1.6 mm thick sheet of PMMA (ACRYCLR0.060FM24X48, ePlastics), which was then finished by milling. The 15 mm sides were then beveled at a 45-degree angle, forming the entrance and exit apertures, through which light may freely enter and exit the waveguide. The entrance and exit apertures of the waveguide are then polished with 1,000 (B01M17A2R1, e-Rookie), 5,000 (B01MCR0J11, e-Rookie), and 12,000 (3S9027, Micro-Surface Finishing Products) grit sandpaper to reach an optical quality finish. Prior to sputter coating, the waveguide was cleaned with DI water and isopropanol (BP2632, Fisher Scientific) in a sonicator (150D, VWR Scientific) bath for 10 minutes each. The waveguide was coated in silver using a sputter coater (EMS 150TES, Quorum Technologies) and a custom-made target (Refining Systems Inc.). The silver target was 99.95% pure, had a diameter of 57 mm and a thickness of 0.5 mm. Sputter coating was done using the following settings:

- Current: 50 mA
- Sputtering time: 391 seconds

The silver coating acts as a cladding layer, keeping the light confined inside the waveguide until it either reaches the ‘active area’ or the exit aperture. The active area of the waveguide is a section devoid of silver directly underneath the area where the center of the transducer is placed. Here, light can exit the waveguide and enter the tissue phantom when they are in contact. The entrance and exit aperture, as well as the active area, were kept free of silver during the sputter coating process by covering these areas with Kapton tape. The thickness of the deposited silver layer was estimated to 300 nm.

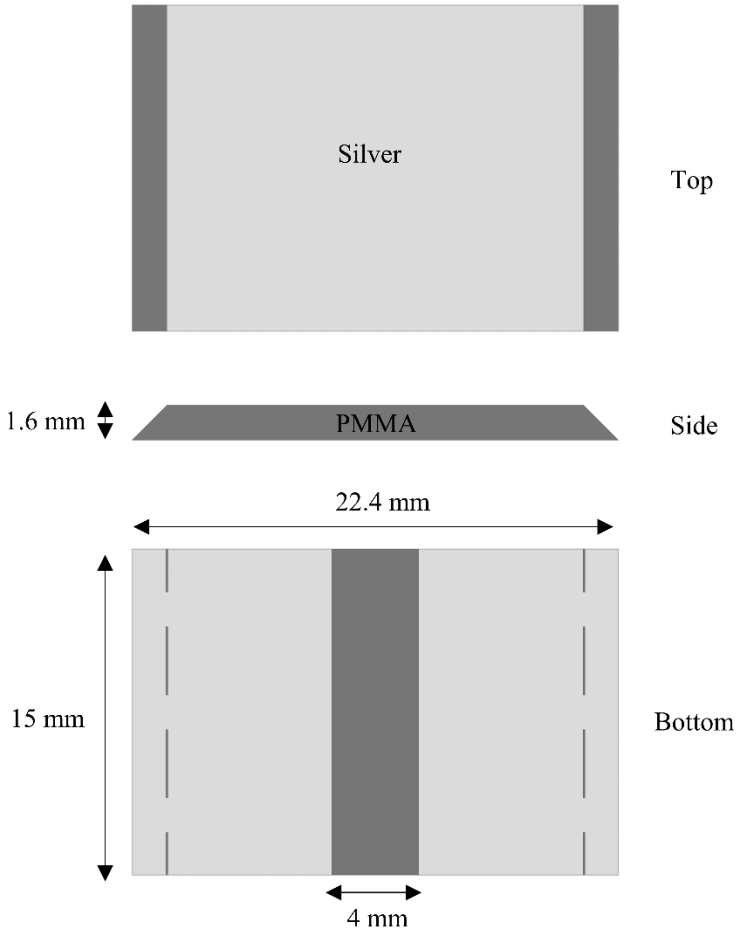

Figure 4.15. Schematic of waveguide used. A 15 mm X 22.4 mm piece of PMMA, which is 1.6 mm thick, is beveled at two ends at 45°. The entrance aperture, exit aperture, and active area are tapped off and the waveguide is coated in a layer of silver. The active area, on the bottom of the waveguide, is devoid of silver to enable coupling of light into the sample under study.

4.1.2.1 Testing PMMA Speed of Sound

The speed of sound of the PMMA was characterized. This was done because the speed of sound is used in the image formation algorithm, so accurate measurements are needed to ensure accurate image construction. To do this, 14 pieces of PMMA were stacked together. Ultrasound gel (03-08, Parker Laboratories) was used to facilitate acoustic coupling between the individual pieces. A piece of electrical tape was attached to one end of the stack to serve as an optoacoustic target. An ultrasound transducer (V320-SU, Olympus)

was placed on the opposite side of the stack and was used to record the optoacoustic signal. The transducer was connected to a digital oscilloscope (5442B, Pico Technologies) via a BNC cable. A 50 Ω feedthrough terminator (TA051, Pico Technology) was used at the connection between the BNC cable and the oscilloscope to reduce electrical noise. Data acquisition was triggered when the laser was fired by using the digital output of the laser system. This was accomplished by using the signal from the Q-switch synchro of the laser to trigger data acquisition by the oscilloscope. The trigger on the oscilloscope was set to 300 mV. To reduce the amount of noise in the received signal, 32 samples were taken and then averaged. The results of the test can be seen in Figure 4.16. The measured speed of sound was 2647 m/s.

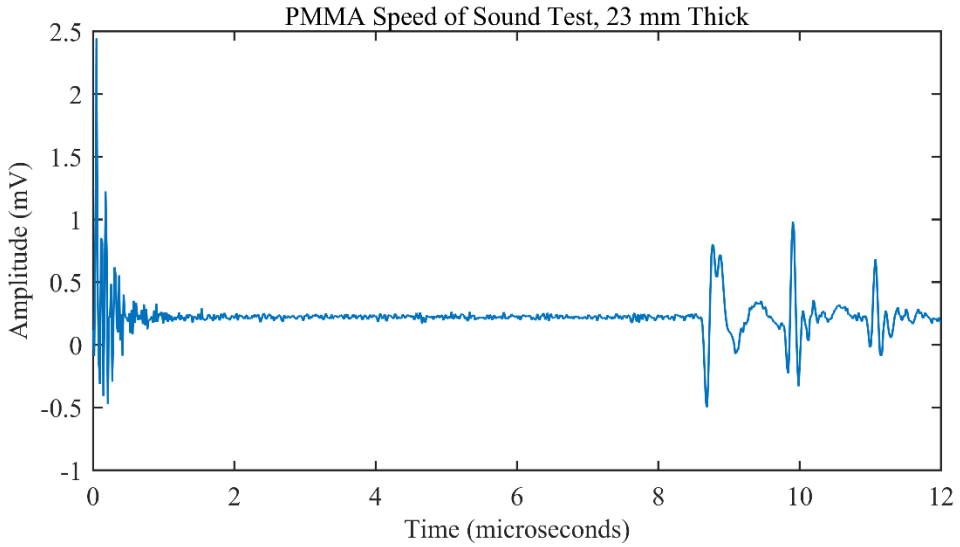

Figure 4.16. Results of the speed of sound test for PMMA. The first signal, originating from the electrical tape, arrived at 8.69 microseconds.

4.1.3 Ultrasound Transducer and Multiplexer

The transducer array used in the device was custom made by Imasonic (France). It had 32 elements, a total length of 6.35 mm and a height of 6 mm. Each element was 0.15 mm wide and the elements were spaced 0.05 mm apart. The transducer array had a central frequency

of 12.4 MHz, and was acoustic impedance matched with PMMA to facilitate coupling between the waveguide and the array. A picture of the transducer is found in Figure 4.17. A more detailed schematic is found in Figure 4.18.

Figure 4.17. A photo of the transducer used in this study. The positions of the first and last transducer elements are marked. The linear array of transducer elements can be seen on the bottom.

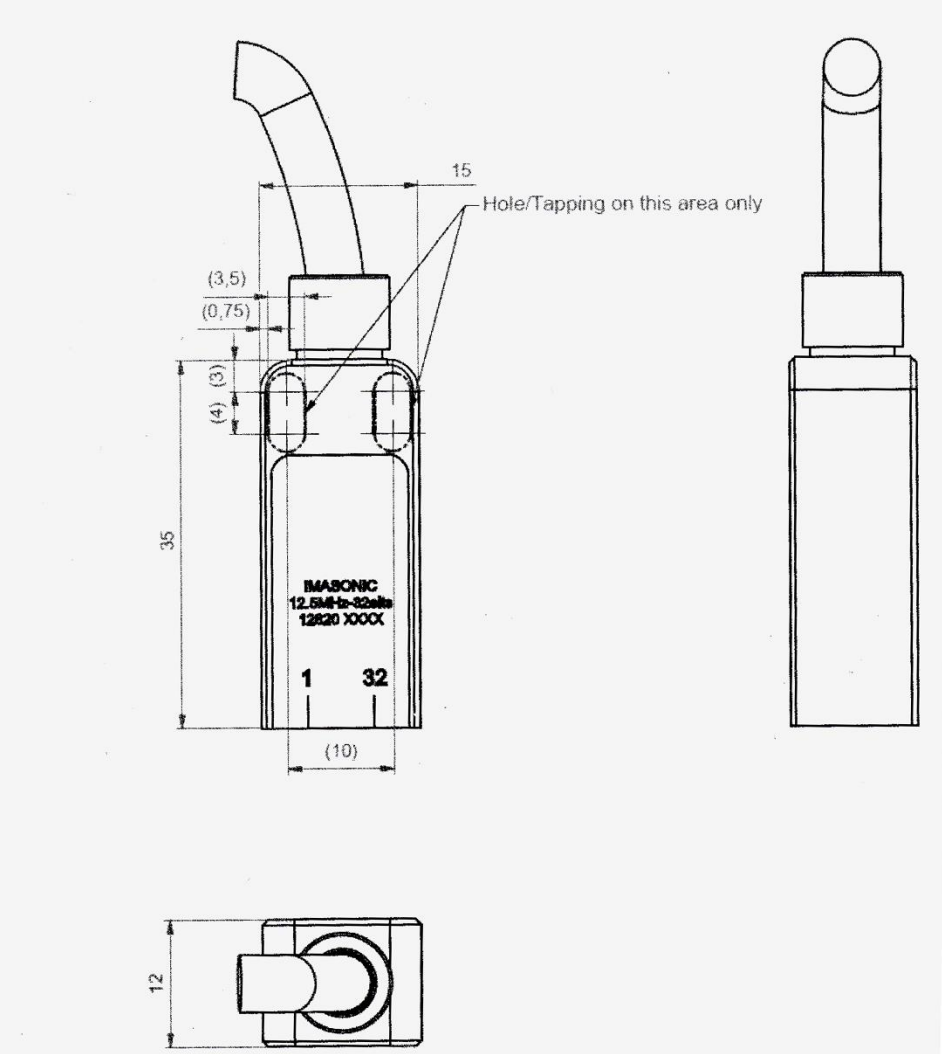

Figure 4.18. A schematic of the transducer used in this study. Units are in millimeters. The transducer array consisted of 32 individual sensing elements arranging linearly, and had a central frequency of 12.4 MHz. The housing was made of stainless steel. A wire extended from the rear of the array, which carried the signals detected by the elements. From Ref. [7].

A digital oscilloscope (5442B, Pico Technology) with four input channels was used for data collection. In order to handle all 32 signals received by the transducer array, a multiplexer was designed and built in-house. This multiplexer contained four multiplexer boards. Each board contained eight inputs, and each input led to an operational amplifier (op-amp) (AD8099, Analog Devices) that allowed for analog amplification of the received signals. Multiplexer chips were used to manage which op-amp was sampled. (MAX4051

ESE 1432, Maxim Integrated). Each board contained two multiplexer chips. One multiplexer chip managed the eight signals coming from the op-amps, and the other selectively enabled the op-amp being sampled. These multiplexer chips were controlled using an Arduino Mega (A000067, Arduino), which passed three digital high-low signals to the multiplexer chips. Using different combinations of high-low voltages, the op-amp being sampled could be controlled. The code for controlling the Arduino can be found in Appendix B.

Each board was connected to a BNC cable, which delivered the signals to the oscilloscope. A 50 Ω feedthrough terminator (TA051, Pico Technology) was attached to each BNC input on the oscilloscope to reduce electrical noise. Each board was tested to evaluate its performance. More information about the multiplexer boards can be found in Appendix B.

4.1.4 Hand-Held Device Design

4.1.4.1 Optical System

The first section of the optical train received light from the laser and focused it into an optical fiber (MHP550L02, Thorlabs), which would then deliver the light to the hand-held device. The lens used to focus the beam (LA1708, Thorlabs) had a focal length of 200 mm. Between the lens and the optical fiber was a polarizing beam splitter cube (CM1-PBS25-532-HP, Thorlabs) and zero-order half-wave plate (WPH05M-532, Thorlabs). This allowed for some light to be directed away from the optical fiber and measured using an energy meter (ES120C, Thorlabs), and the amount that was directed toward the energy meter was controlled by altering the position of the wave-plate. The fiber optic was connected to the optical system via a kinematic mount. This was made using a mount that

allowed for translation along the axis of the optical system (SM1X, Thorlabs), and mount that allowed for translation the in the lateral directions (LM1XY, Thorlabs). Light was coupled into the optical fiber with at least 80% efficiency. A schematic of the first section of the optical train can be seen in Figure 4.19.

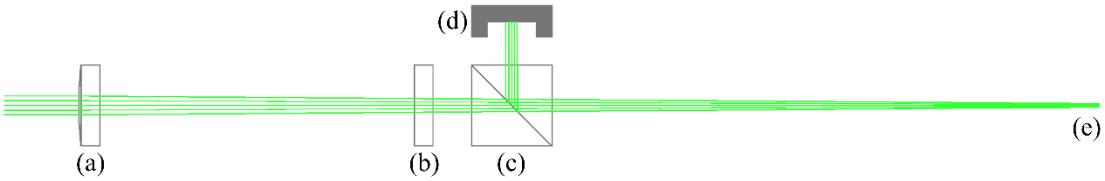

Figure 4.19. Schematic of the optical system used to couple laser light into the optical fiber. The optical system contained a 200 mm focal lens **(a)**, a zero-order half-wave plate **(b)**, a polarizing beam splitter cube **(c)**, an energy meter **(d)**, and an optical fiber **(e)**.

The optical system within the device was designed to be compact so that it could be integrated with a hand-held device. For the initial prototype, it was decided that an optical cage system should be used, as opposed to 3D printing the lens housing within the device, to provide a rigid structure for lens placement as well as the ability to rapidly test different lens configurations. The optical system consisted of an optical fiber collimation package (F220SMA-532, Thorlabs), which collimated the light input into the optical system by the optical fiber. After the light was collimated, it was compressed on one axis using a 100 mm focal length plano-convex cylindrical lens (48-356, Edmund Optics) and further focused using a 60 mm focal length plano-convex lens (32-855, Edmund Optics) to combat beam divergence. Then it was directed toward the waveguide by a silver mirror (ME05-P01, Thorlabs), which was mounted in a 3-axis kinematic mount (KSO5K/M, Thorlabs) that allowed for fine-tuning of light coupling into the waveguide. The spot size of the beam at the entrance of the waveguide was an ellipse with a long axis of 4 mm and a short axis of 2 mm. The spot size on the active area of the waveguide was a circle with a

radius of approximately 2 mm. A schematic of the system can be seen in Figure 4.20.

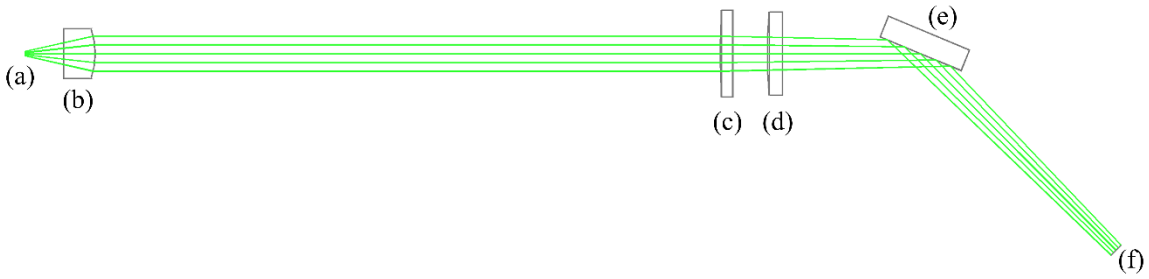

Figure 4.20. Schematic of the optical system in the handpiece. This consisted of an optical fiber **(a)**, a fiber collimating lens **(b)**, a plano-convex cylindrical lens **(c)**, a plano-convex lens **(d)**, and a mirror **(e)**. The entrance of optical waveguide is also marked **(f)**.

4.1.4.2 Hand-Held Device

The hand-held device was designed in collaboration with clinicians at the University of Missouri Hospital Burn and Wound Center. The device was designed around the optical train, and made to be ergonomic and intuitive to use. A rendering of the device can be seen in Figure 4.21. The device consisted of 4 pieces 3D printed separately. The parts included the housing, the handle, the housing cap, and the waveguide cap. The housing contained the optical system, which slid into an opening at the rear of the housing. The housing cap was placed over this opening, and attached with screws to the housing to keep the optical system securely in place. The handle was press-fit into a slot on the bottom of the housing. The waveguide cap, which held the waveguide, was attached using screws. The waveguide was mounted within the waveguide cap using super glue (15109, Pacer Technology) and the any gaps between the waveguide cap and the edges of the waveguide were filled with white silicon (GE281, General Electric). The transducer was placed in a cavity directly behind the waveguide.

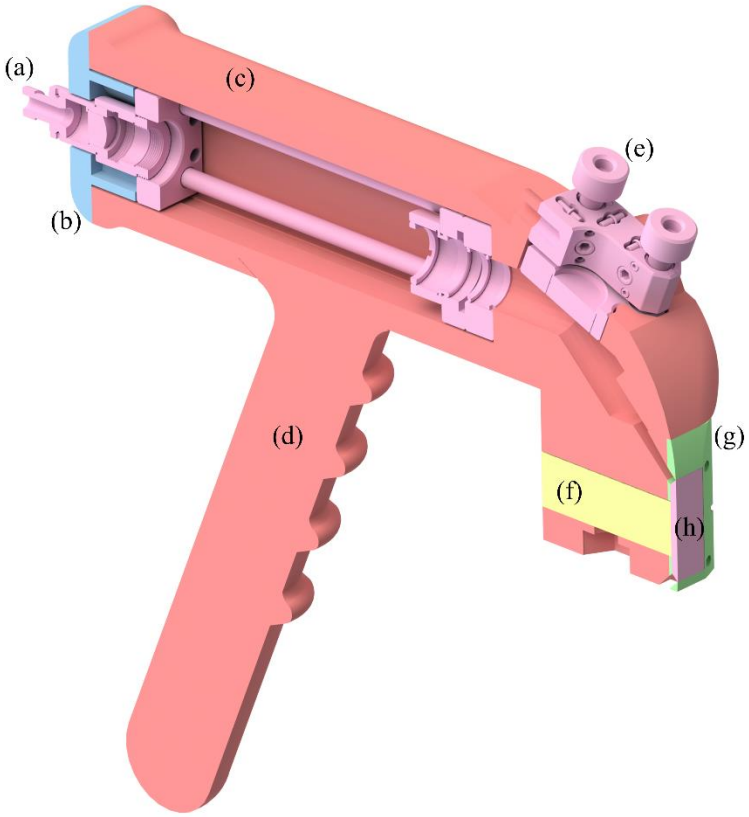

Figure 4.21. A cross-sectional view of the assembled hand-held device. The optical fiber connected to the optical system (highlighted in pink) at **(a)**. The optical system was kept in place by the housing cap **(b)**, which screwed into the housing. The housing (highlighted in red) consisted of two parts 3D printed separately: the main housing **(c)** and the handle **(d)**. The mirror was placed in a kinematic mount **(e)**, and held in place by screws. The transducer **(f)**, highlighted in yellow, slid into a cavity behind the waveguide **(h)**, which was held in the waveguide cap **(g)** (highlighted in green).

4.1.5 Testing Setups

4.1.5.1 Setup for Imaging the Hair Phantom and Burn Wound Phantom

A schematic of the setup for imaging the tissue phantom containing the hair, used for determining the resolution, can be seen in Figure 4.22. The setup for imaging the burn wound phantom is similar, and can be seen in Figure 4.23. In each setup, the light output by the laser, which had a diameter of 3 mm, was directed toward the sample. The sample was positioned on a supporting surface, and a piece of PMMA coated in 300 nm silver was

placed on the opposite side of the sample as the incident laser light. The PMMA was coated using the same method as the waveguide. This prevented optoacoustic waves from being produced due to light absorption by the transducer array, which was placed on the opposite side of the PMMA as the sample. Acoustic coupling between the sample and the PMMA was facilitated by ultrasound gel (03-08, Parker Laboratories) acoustically matched to tissue. In the burn wound tissue phantom, acoustic coupling between the two pieces of the tissue phantom was accomplished using the same ultrasound gel. Acoustic coupling between the transducer and the PMMA was facilitated by high acoustic impedance ultrasound coupling gel (Echo Z Plus MV-04, ECHO Ultrasonics). The energy density at the surface of the sample was measured using an energy meter, and the average of 100 pulses was measured. The energy density used to image the hair phantom was 90.4 mJ/cm^2, and the energy density used to image the burn wound phantom was 18.4 mJ/cm^2.

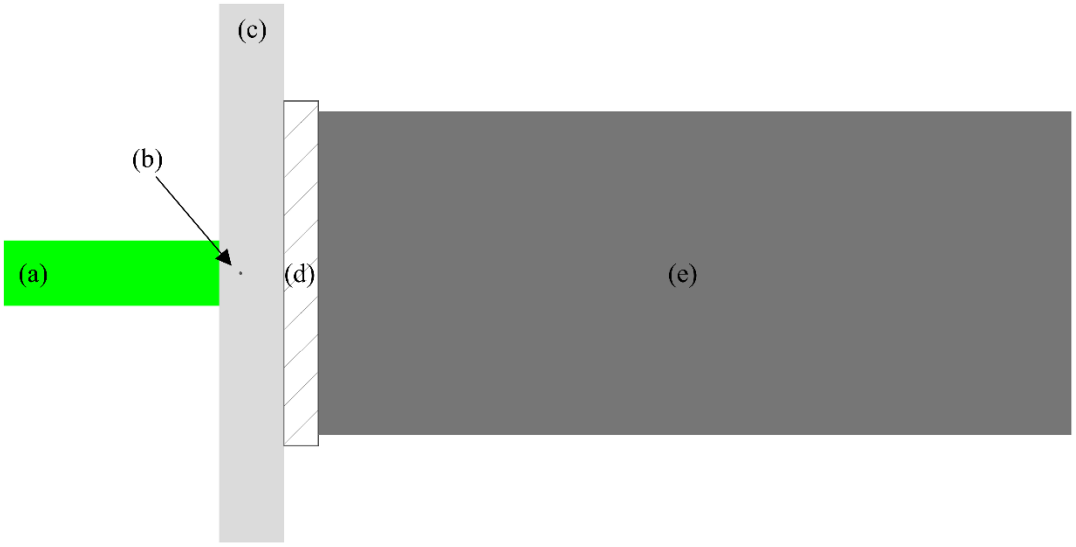

Figure 4.22. Schematic of the setup used for imaging the tissue phantom for determining lateral and axial resolution of the imaging platform. The laser light **(a)** is directed toward the phantom **(c)** which contains the hair **(b)**. Between the phantom and the transducer **(e)** is a piece of PMMA **(d)** coated in silver, which both simulates the presence of a waveguide and stops light being absorbed by the face of the transducer.

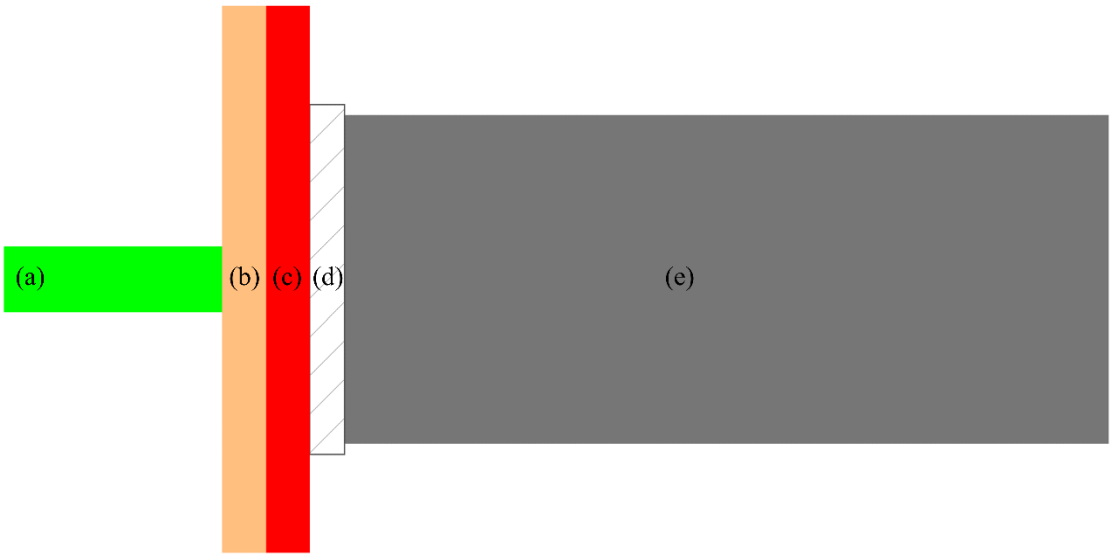

Figure 4.23. Schematic of the setup used for imaging the burn wound tissue phantom. The laser light **(a)** is directed toward the phantom. The phantom is made of two separate pieces, the dermis **(b)** and the hyperemic layer **(c)**. Between the phantom and the transducer **(e)** is a piece of PMMA **(d)** coated in silver, which both simulates the presence of a waveguide and stops light being absorbed by the face of the transducer.

4.1.5.2 Setup for Demonstrating Hand-Held Device

A picture of the setup used to demonstrate the imaging capabilities of the hand-held device is found in Figure 4.24, and a schematic is found in Figure 4.25. In the setup, light from the laser was coupled into the optical fiber and delivered to the hand-held device which was held in place by a clamp. During testing, high acoustic impedance ultrasound coupling gel (Echo Z Plus MV-04, ECHO Ultrasonics) was used to facilitate acoustic coupling between the waveguide and the transducer. The device was pressed against the tissue phantom, and acoustic coupling between the waveguide and the tissue phantom was facilitated using ultrasound gel (03-08, Parker Laboratories). The energy delivered to the waveguide, measured as the average of 100 pulses, was measured for both phantoms. For the phantom with a target depth of 0.99, the energy was 79 μJ, which resulted in an

approximate energy density on the surface of the phantom of 0.63 mJ/cm^2. For the phantom with a target of 1.22 mm, the energy was 67 μJ, which resulted in an approximate energy density on the surface of the sample of 0.53 mJ/cm^2.

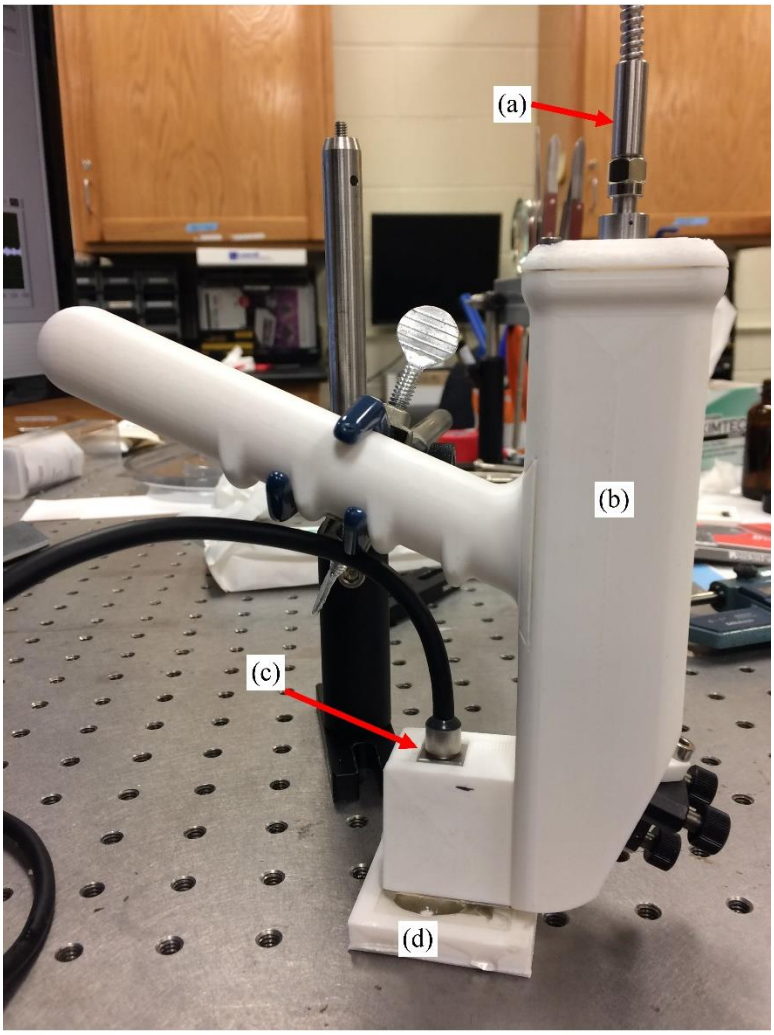

Figure 4.24. Picture of the testing setup used to demonstrate the imaging capabilities of the hand-held platform. The optical fiber **(a)** delivered light to the probe **(b)** which was held in place by a clamp. The transducer can be seen **(c)**. The device is pressed against the tissue phantom, which is contained in a mold **(d)**.

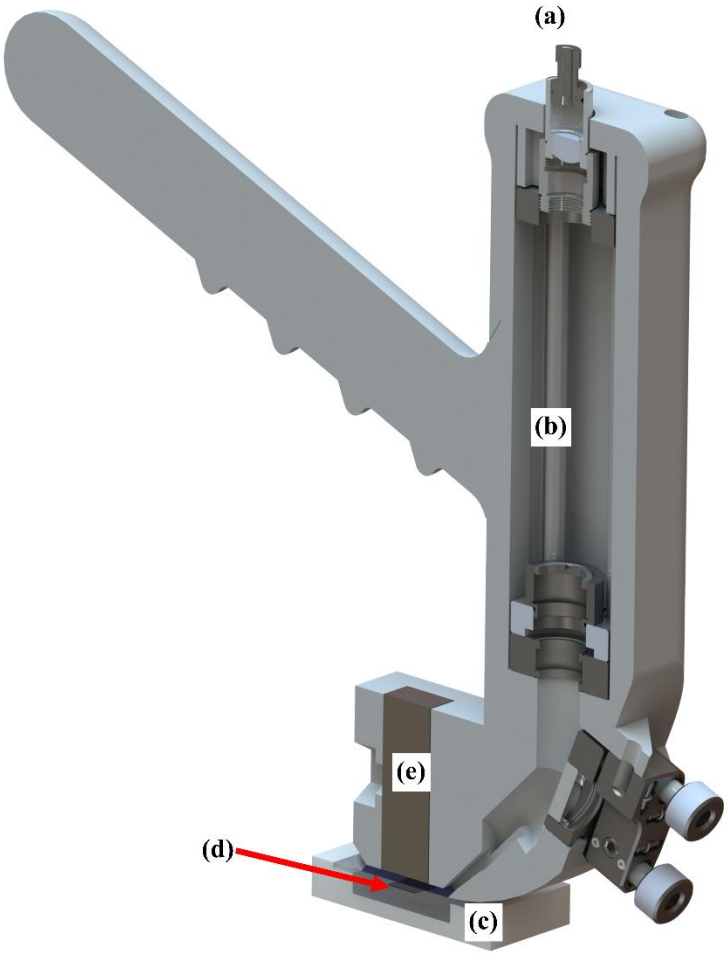

Figure 4.25. A schematic of the setup used to evaluate the performance of the hand-held imaging platform. The optical fiber is attached at **(a)**, which delivers light to the optical train, which is labeled **(b)**. This delivers light to the tissue phantom in a mold, labeled **(c)**. The tissue phantom contains a piece of electrical tape, which is labeled **(d)**. The light absorbed by the electrical tape generates and optoacoustic signal, which is detected by a transducer, labeled **(e)**.

4.1.6 LabVIEW Program for Automated Data Collection

During imaging, all components of the system were controlled using a LabVIEW program made in house. The LabVIEW program also normalized the data to any discrepancies between the amplifications provided by different op-amps as well as data filtering. Data

was high-pass filtered using a build-in filter function in LabVIEW. The filter was set as a second-order Butterworth filter with a low cutoff frequency of 50 kHz. The system could be set to sample every element of the transducer several times so that signal averaging could be accomplished. Here, sampling every element once is referred to as a scan. For each test, 32 scans were recorded.

The program was connected to the laser system using an RS232 cable, through which the Q-switch delay was controlled, as was the flashlamp and laser firing operations. The program was connected to the Arduino via a USB serial connection, through which commands were sent to switch DC voltage output pins to high or low, which in turn controlled op-amp selection during signal acquisition. The program was connected to the oscilloscope via a USB connection. Through this connection, many aspects of signal acquisition were controlled, those of importance are listed here:

- Pre-trigger samples: 100
- Post-trigger samples: 1400
- Trigger threshold: 120 mV
- Trigger direction: Rising
- Input channel range: 500 mV
- Resolution: 14-bit

The operation of this program will be described here, and more additional information about the program can be found in the Appendix B. Operation begins with first setting the Q-switch of the laser and firing the flashlamp to warm the laser system up. The system then proceeds to gather data using the following steps:

1. Select the transducer elements to be sampled by directing the Arduino to select the

appropriate op-amps

2. Fire the laser once
3. Wait from the signal from the Q-switch synchro to reach the trigger threshold
4. Record 1500 samples from each input of the oscilloscope
5. Normalize and filter the data
6. Display the data for inspection by the user
7. Save the data to a .csv file
8. Repeat steps 1-7 until all elements of the transducer have been sampled
9. Repeat steps 1-8 until all scans have been completed

The loop took ~56 s to complete.

4.1.7 Delay-And-Sum Imaging Forming Algorithm

Images were made using a MATLAB program developed in house that utilizes a Delay-and-Sum (DAS) image forming algorithm, described previously in Section 3.3. Two image forming algorithms were used. One was used when the resulting image was to be used for determining the axial and lateral resolution of the hand-held device. In this algorithm, the resolution of the image (physical size of each pixel on the imaging plane) was set to be much finer than the theoretical maximum resolution of the system (here, a pixel size of 2.5 μm was used). This allowed for the actual spatial resolution of the system to be determined. In the second algorithm, the resolution of the image was set so that the size of each pixel was at least half of the spatial resolution each direction (lateral and axial) to satisfy the Nyquist criterion.

In each program, the data from a user-selected .csv file was loaded, and the signals from each transducer element were read and averaged. The resulting averaged signals were

then passed to the DAS image forming algorithm. The output of the algorithm was an array of numbers, whose magnitude corresponded with the amplitude of the optoacoustic signal originating from the area on the imaging plane corresponding with the position the number in the array. An example of this can be seen in Figure 4.26. All algorithms used can be found in Appendix C.

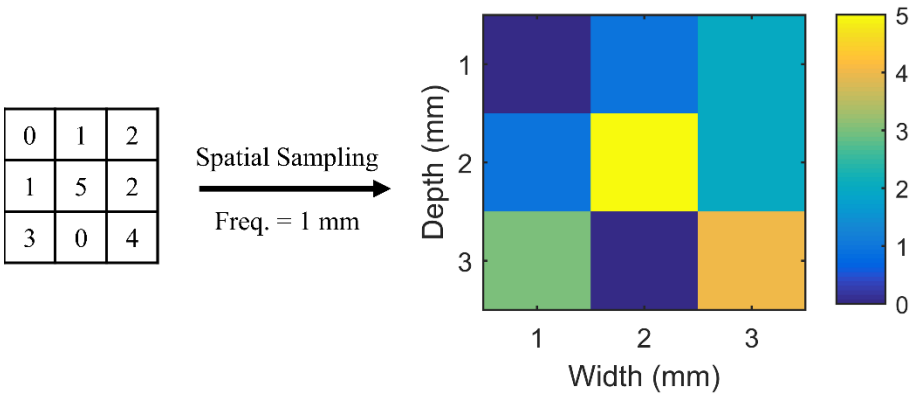

Figure 4.26. Example of how the array produced by the image forming algorithm is turned into a usable image. The array of numbers output by the algorithm can be seen on the left. The values within the array represent the amplitude (here in arbitrary units) of the optoacoustic signal originating for the space associated with each position in the array. We know the spatial sampling frequency is 1 mm in both directions, so we can constructer an image, seen on the right.

4.1.8 Monte Carlo Simulations

To demonstrate the necessity of direct illumination of the target issue, as opposed to illuminating the transducer array from the side, Monte Carlo simulations of photon transport in skin tissue were performed. This was done using an open-source Monte Carlo simulation package (Release 5: MCML 1.2.2 & CONV 1.1) [8, 9]. The simulated tissue contained three separate layers: the epidermis, the dermis, and the hypodermis (subcutaneous tissue). The values assigned to the layers were taken from literature [4, 6,

10, 11]. The wavelength of light used in the simulations was 556 nm, which was assumed to be a good approximation of the light used in this study (532 nm).

Three separate simulations were run, each with a different incidence angle of the light upon the tissue to investigate the effects of using oblique illumination. These angles were 0°, 30°, and 60°. In the simulation, the tissue is discretized, and photons are introduced to the center of a cylindrically symmetrical model tissue at the top of the tissue (Figure 4.27). The simulation tracked photon propagation, included scattering, absorption, reflection, and refraction. The results of the simulations indicated where light was absorbed in the tissue, which corresponded to the locations from which the optoacoustic signals originated. The output of the simulation was a 2D grid, representing where photons were absorbed along one slice of the cylindrical tissue. The file used to initiate the simulation can be found in Appendix D.

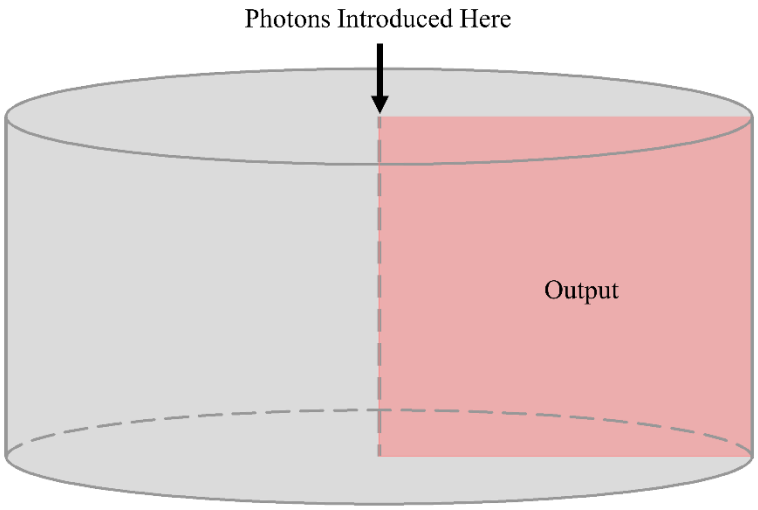

Figure 4.27. Schematic of the simulation space showing where photons are introduced to the tissue and where the output data is taken from.

For analysis, it was assumed that the light was introduced at the side of a transducer, meaning that any light that was absorbed in the area beyond the first column of elements within the tissue was considered absorbed within the acoustic detection column of the transducer (Figure 4.28). The acoustic detection column is directly under the transducer, where it is most sensitive.

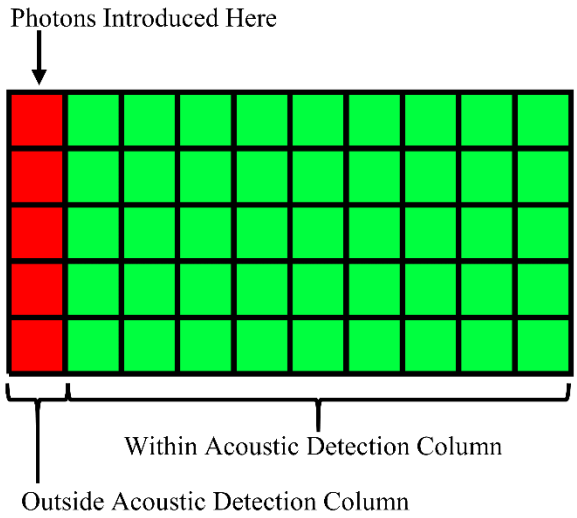

Figure 4.28. Schematic of the simulated tissue, also showing how the results are analyzed. The tissue is discretized, shown by the grid. Photons are introduced to the tissue at the top, left-most element. The results of the simulation are where photons were absorbed, indicated where optoacoustic signals would originate from. It was considered that the light was introduced at the side of a transducer, and any photons absorbed by elements to the left of the first column were considered to be absorbed within the acoustic detection column. If the light was not absorbed here, it was considered be outside of the detection column.

4.2 Results and Data Analysis

This section presents the results of the tests previously described. The first portion covers the results of the phantom used to determine the lateral and axial resolution. The second covers the demonstration of the hand-held imaging device. The next portion covers the results of imaging the burn wound tissue phantom. The last portion covers the results of the Monte Carlo simulations.

4.2.1 Characterization of Resolution

The optoacoustic image made using the setup previously described for the hair tissue phantom can be seen in Figure 4.29. Because the diameter of the hair is several times smaller than the maximum lateral resolution of the system (161 μm), it can be treated like a point source.

The point spread function (PSF) of the hair was taken from the image and used to determine the lateral resolution of the system [12]. To do this, a Gaussian curve was fit to the measured PSF, and the full-width at half-max (FWHM) of the point spread function was taken to be lateral resolution (Figure 4.30). The measured lateral resolution was 550 microns.

The axial resolution could not be determined by treating the hair as a point source, however, because the diameter of the hair was about equal to the theoretical maximum axial resolution of the system, which was 58 μm. Instead, an alternative method was used that subtracted the measured diameter of the hair from the width of the hair in the image, which was described in the Chapter 3 [13]. The intensity of the imaged hair along in the axial direction was evaluated (Figure 4.31). The base of the peak was determined to have a width of 143 μm, which resulted in an axial resolution of 77 μm.

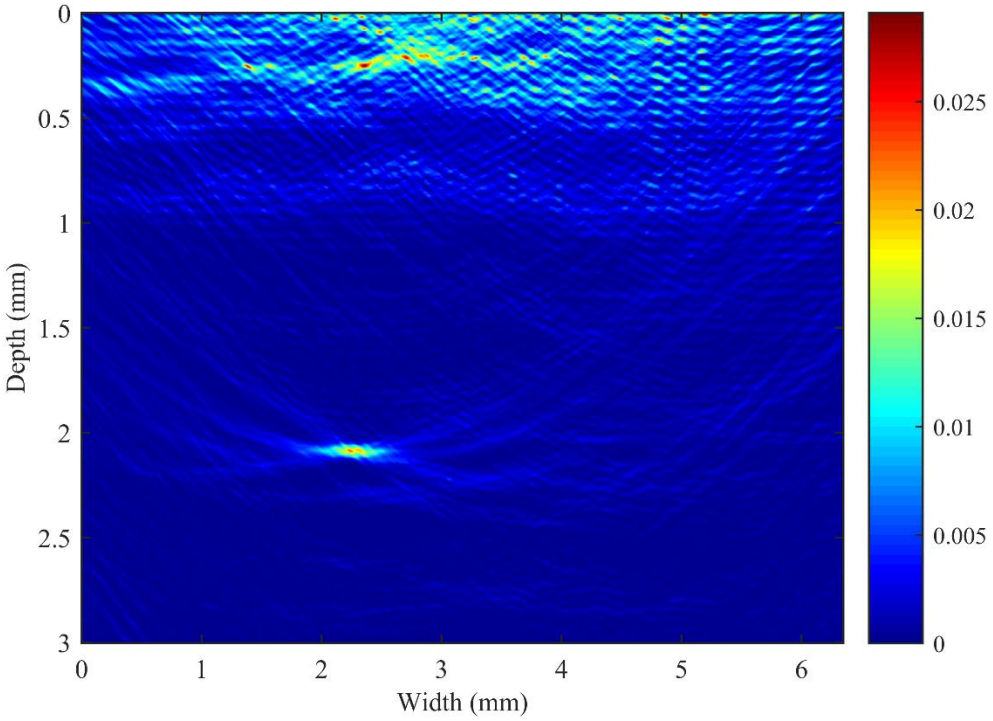

Figure 4.29. Image of hair phantom. The hair can be seen at a depth of ~2.1 mm. Some noise can be seen at the top of the image. This is due to the relatively small signal coming from the hair. The amplitude in the figure is in arbitrary units.

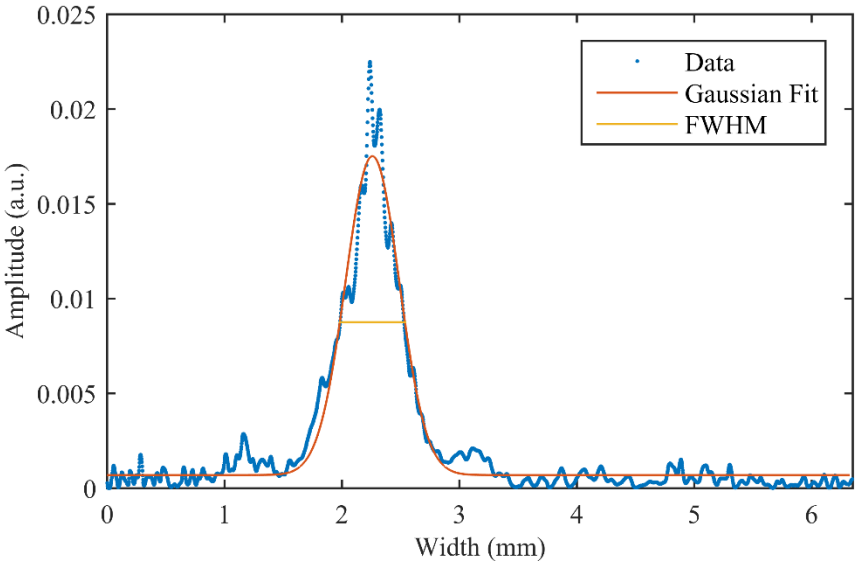

Figure 4.30. PSF of the hair imaged in the lateral direction. The FWHM of the PFS is 550 microns.

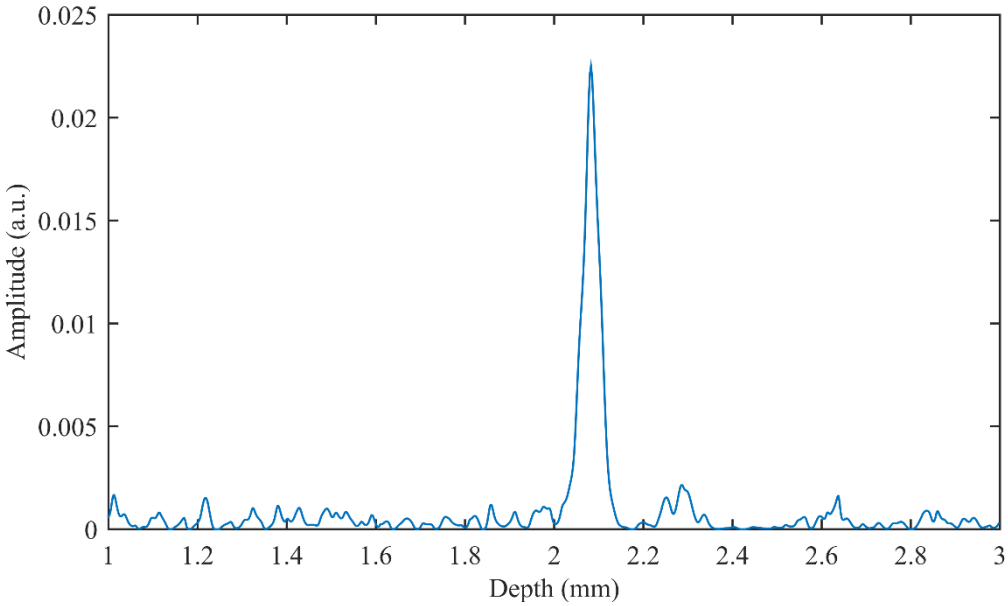

Figure 4.31. The intensity of the image hair along the axial direction. The width at the base of the peak is 143 μm, resulting in an axial resolution of 77 μm.

4.2.2 Demonstration of Hand-Held Device

The images made from the electrical tape phantoms are found in Figures 4.32 and 4.33. The spatial sampling of the imaging algorithm was at least half that of the resolution of the imaging system to satisfy the Nyquist criterion. This was done to evaluate how fast the algorithm could produce an image that was to resolve all features the system was able to detect. Image processing required ~17 seconds. The measured depths (made using a micro-caliper (293-761-30, Mitutoyo)), of the electrical tape phantoms compared with the depths determined by their images are found in Table 4.4.

Table 4.4 Comparison the measured depths of the electrical tape targets and their depths determined using the hand-held platform.

Measured Depth	Depths in Image
0.99 mm	1.2 mm
1.22 mm	1.44 mm

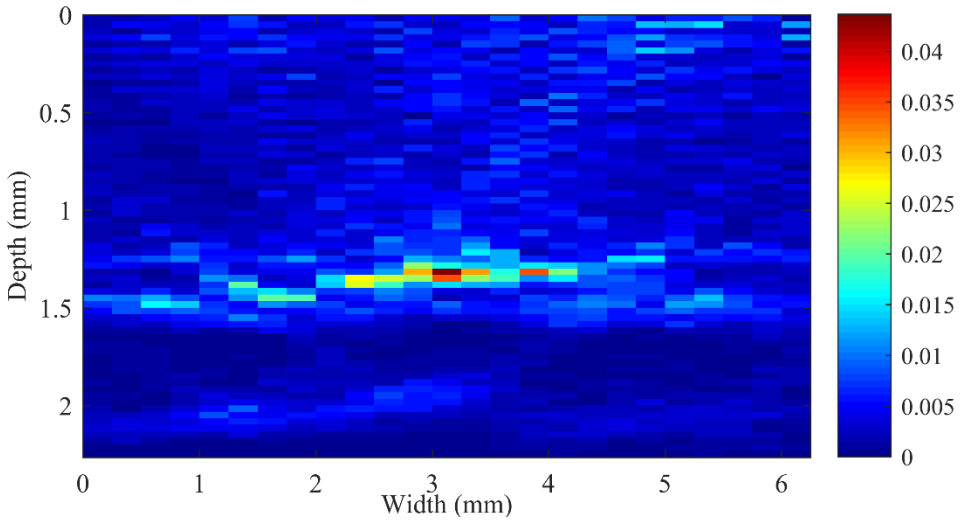

Figure 4.32. The image of the electrical tape phantom that was imaged using the hand-held device where the electrical tape was 0.99 mm deep. The depth determined by the image was 1.2 mm.

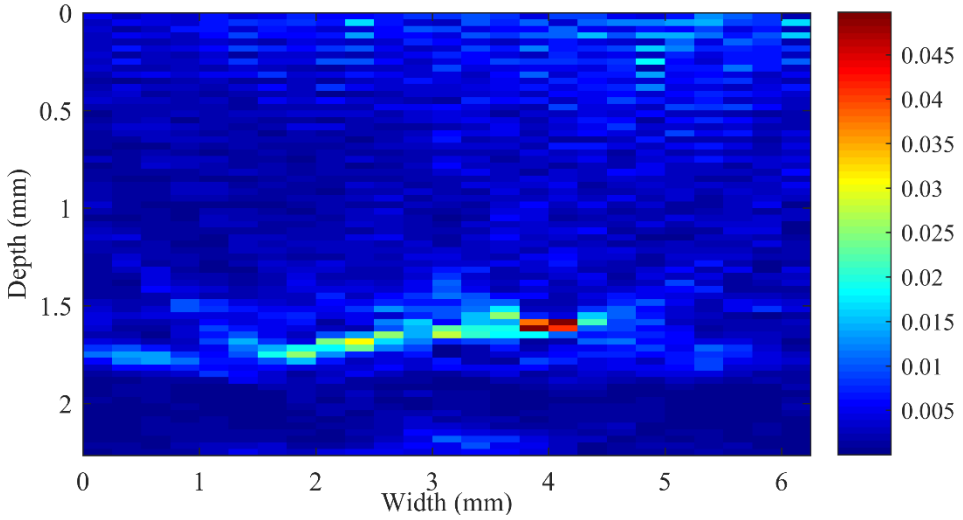

Figure 4.33. The image of the electrical tape phantom that was imaged using the hand-held device where the electrical tape was 1.22 mm deep. The depth determined by the image was 1.44 mm.

4.2.3 Imaging of Burn Wound Tissue Phantom

The image of the burn wound tissue phantom is found in Figure 4.34. Image formation required ~27 seconds. The depth of the burn wound phantom, as determined by the image, was 2.54 mm. The measured depth (made using a micro-caliper (293-761-30, Mitutoyo)),

was 2.18 mm. The contrast-to-noise (CNR) ratio of the image was 7.7. Here, the noise within the image was taken to be all signals within a depth of 2.1 mm. The region of interest was defined as an area 0.09 mm deep (3 pixels) and 0.75 mm wide (3 pixels) centered around the point of greatest intensity.

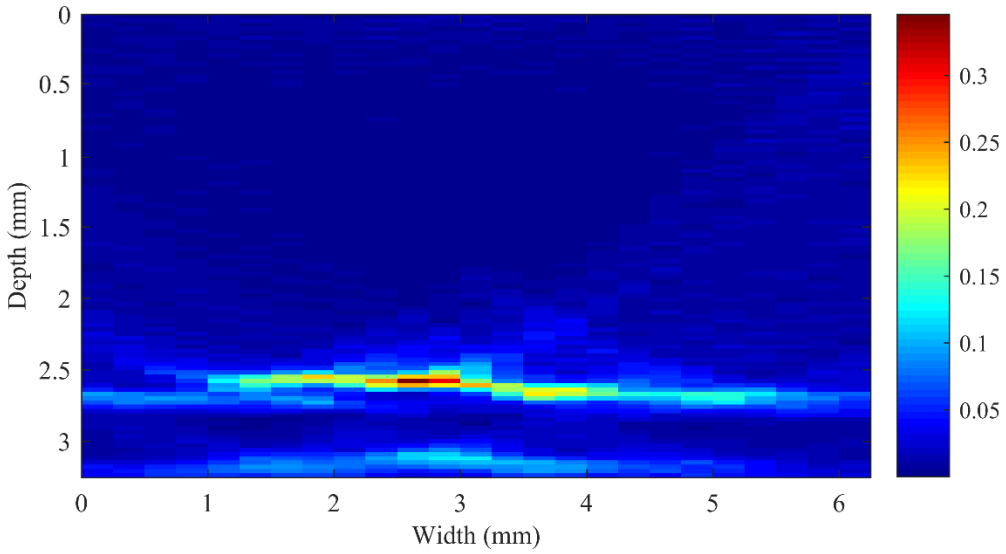

Figure 4.34. The image of the burn wound tissue phantom. The measured depth was 2.18 mm, and the depth determined by the image was 2.54 mm.

4.2.4 Results of Monte Carlo Simulations

The results of the Monte Carlo simulations for light with an incidence angle for 0°, 30°, and 60° can be seen in Figures 4.35, 4.36, and 4.37, respectively. The amount of light absorbed within the acoustic detection column for an incidence angle of 0°, 30°, and 60° was 12%, 27%, and 16%, respectively.

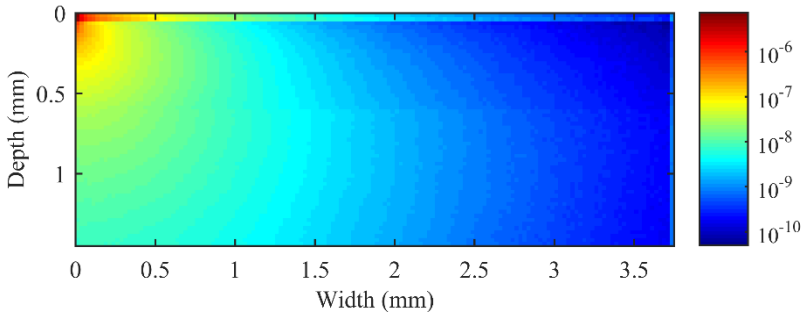

Figure 4.35. Absorption within the synthetic tissue for light with an incidence angle of 0°. Values are in percent of total light absorbed. Light was introduced to the tissue at the top left corner. 12% of the light was absorbed within the transducer detection column.

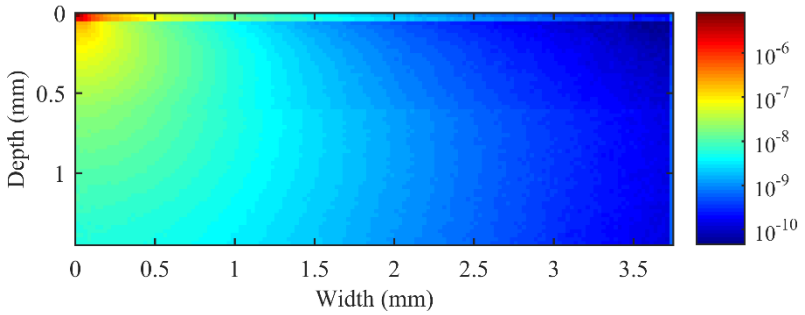

Figure 4.36. Absorption within the synthetic tissue for light with an incidence angle of 30°. Values are in percent of total light absorbed. Light was introduced to the tissue at the top left corner. 27% of the light was absorbed within the transducer detection column.

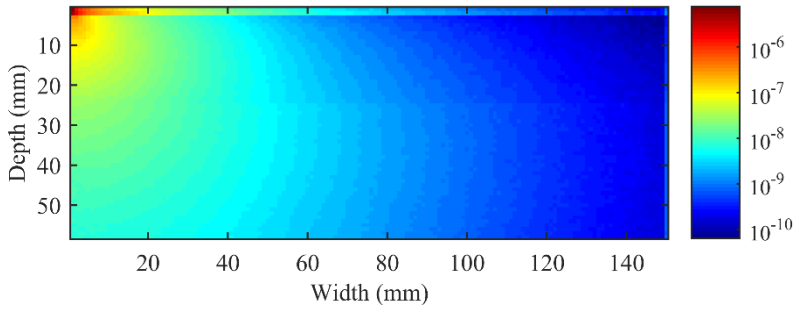

Figure 4.37. Absorption within the synthetic tissue for light with an incidence angle of 60°. Values are in percent of total light absorbed. Light was introduced to the tissue at the top left corner. 16% of the light was absorbed within the transducer detection column.

4.2.5 Summary

Using the data presented we were able to characterize key aspects of the imaging platform. This was done using the analysis techniques outline the Chapter 3. Of interest to this study was the resolution of the images that the waveguide-transducer could produce.

This information was taken from the hair tissue phantom. The performance of the hand-held platform was also assessed using the electrical tape tissue phantoms. Images of optoacoustic targets at different depths were collected and analyzed. This was to explore if the accuracy of the imaging platform changed with respect to depth. Last, it was of interest if the waveguide-transducer pair could image a burn wound tissue phantom.

Bibliography

[1] S. Monstrey, H. Hoeksema, J. Verbelen, A. Pirayesh, P. Blondeel, Assessment of burn depth and burn wound healing potential, Burns 34(6) (2008) 761-769.

[2] T. Ida, H. Iwazaki, Y. Kawaguchi, S. Kawauchi, T. Ohkura, K. Iwaya, H. Tsuda, D. Saitoh, S. Sato, T. Iwai, Burn depth assessments by photoacoustic imaging and laser Doppler imaging, Wound Repair and Regeneration 24(2) (2015) 349-355.

[3] H.F. Zhang, K. Maslov, G. Stoica, L.V. Wang, Imaging acute thermal burns by photoacoustic microscopy, J. of Biomedical Optics, SPIE, 2006, p. 5.

[4] A.I. Chen, M.L. Balter, M.I. Chen, D. Gross, S.K. Alam, T.J. Maguire, M.L. Yarmush, Multilayered tissue mimicking skin and vessel phantoms with tunable mechanical, optical, and acoustic properties, Medical Physics 43(6) (2016) 3117-3131.

[5] J.R. Cook, R.R. Bouchard, S.Y. Emelianov, Tissue-mimicking phantoms for photoacoustic and ultrasonic imaging, Biomedical Optics Express 2(11) (2011) 3193-3206.

[6] L.J. Steven, Optical properties of biological tissues: a review, Physics in Medicine & Biology 58(11) (2013) R37.

[7] IMASONIC, Measurment Reprot, 12.5 MHz 32 Elements Array (Report No. 12820 1001), France, 2016.

[8] L. Wang, S.L. Jacques, L. Zheng, Conv—convolution for responses to a finite diameter photon beam incident on multi-layered tissues, Computer Methods and Programs in Biomedicine 54(3) (1997) 141-150.

[9] L. Wang, S.L. Jacques, L. Zheng, MCML—Monte Carlo modeling of light transport in multi-layered tissues, Computer Methods and Programs in Biomedicine 47(2) (1995) 131-146.

[10] D. Huafeng, Q.L. Jun, A.W. William, J.K. Peter, H. Xin-Hua, Refractive indices of human skin tissues at eight wavelengths and estimated dispersion relations between 300 and 1600 nm, Physics in Medicine & Biology 51(6) (2006) 1479.

[11] H.-C. Lee, Introduction to Color Imaging Science, Cambridge University Press2005.

[12] L.V. Wang, H. Wu, Biomedical Optics: Principles and Imaging, Wiley2007.

[13] K. Geng, W. Xueding, S. George, V.W. Lihong, Multiple-bandwidth photoacoustic tomography, Physics in Medicine & Biology 49(7) (2004) 1329.

Chapter 5

Discussion and Conclusions

This chapter discusses the results of data analysis and the conclusions that can be inferred from them. Finally, we present our short-term goals and long-term milestones that need to be addressed for proper clinical translation of this platform.

5.1 Discussion of Results

5.1.1 Axial and Lateral Resolution

The spatial resolution of any medical imaging platform is an important metric in evaluating clinical viability. It is a measure of how fine a structure the platform can image, and in burn depth profiling, this translates into to the precision with which the platform can determine wound depth. The resolution achieved by the forward-mode imaging described in Chapter 4 is accepted as a good measurement of the resolution of the presented hand-held platform because all acoustically relevant components are in play the same way they are in the hand-held platform. For instance, the piece of PMMA used to simulate the presence of the waveguide is cut from the same material from which the waveguides were made. Although the piece of PMMA used is coated only on one side with silver, and the waveguide is coated on both sides, this is not expected to alter acoustic propagation because the thicknesses of the silver layers are much smaller than the central acoustic wavelength of the ultrasound transducer (thickness of silver layer: 300 nm, 12.4 MHz wavelength in silver: 0.29 mm) [1].

Using the equations described in Chapter 2, the maximum theoretical axial and lateral resolutions of the system are 58 μm and 161 μm, respectfully. The realized axial and

lateral resolutions of the platform are 77 μm and 550 μm, respectfully. Although the realized lateral resolution is not close to the maximum theoretical resolutions, these results are satisfactory for an initial prototype.

5.1.2 Demonstration of the Hand-held Platform

The demonstration of the hand-held platform in imaging a strongly optically absorbing structure (electrical tape) within an optically non-absorbing and non-scattering tissue phantom was used because only relatively low levels of laser energy could be delivered to the waveguide. This was due the small amount of energy that could be passed through the optical fiber which delivered light to the hand-held probe, limiting the energy that could be delivered to the waveguide. While these tissue phantoms do not mimic the optical environment of human skin tissue, they do allow for the imaging capabilities of the platform to be demonstrated. Similar tissue phantoms are often used in initial demonstrations of new OAI platforms [2, 3].

The images produced showed the viability of the presented hand-held platform in imaging structures within 1.22 mm of the tissue surface. The shallow depths chosen for the optoacoustic targets were chosen because of the non-scattering nature of the tissue phantoms. This caused light entering the phantom from the waveguide to continue traveling at an angle in the phantom. As depth increased, the point at which the laser beam meets the optoacoustic target moves farther away from the imaging plane, which may decrease image quality. This would not be an issue when imaging actual skin tissue because light entering the tissue would become highly scattered within the epidermis, mitigating this effect. The depths of the targets determined using the platform were different from the depths directly measured. The causes of this, and a potential solution, are discussed in Section 5.1.5.

5.1.3 Imaging of Burn Wound Tissue Phantom

Because only a small amount of laser energy could be passed through the hand-held probe, the viability of the waveguide-transducer pair for burn wound imaging was assessed using forward mode OAI. The results of this indicated that the platform was able to differentiate between dermis tissue and the hyperemic bowl at depths up to 2.18 mm. This penetration depth is suitable to image up partial thickness burns, which are the most challenging to correctly diagnose [4].

5.1.4 Monte Carlo Simulations

The use of opaque piezoelectric ultrasound transducers presents complications in light delivery to the target tissue, and one of the first methods of overcoming this was illuminating the sensor or sensor array from the side. This method relies on optical scattering within the tissue to deliver light to the tissue underneath the sensor(s), where sensitivity is greatest. The results of the Monte Carlo simulations indicate that this solution is far from optimal. Three incidence angles of light were explored (0°, 30°, and 60°), and the results indicate that only a fraction of the light delivered to the side of a sensor would actually make it to the target tissue. This highlights the need to use spacers between the sensor(s) and the tissue, which allows for direct illumination. Conventional spacers simply offset the sensor(s) from the tissue and illuminate the tissue at an oblique angle. But the introduction of this spacer, typically several millimeters, degrades image quality. Waveguides, such as the one used in this study, can greatly decrease the distance between the tissue and the sensors(s), improving image quality while still directly delivering light to the target tissue.

5.1.5 Current Limitations

The current limitations of the presented platform are (1) imaging speed, (2) resolution, (3) imaging depth, and (4) discrepancies between the depth of the imaged object in the image and its actual depth. The current system is able produce an image with a width of 6.25 mm and depth of 3.24 mm with a data acquisition time of ~56 seconds and image formation time of ~27 seconds. In the study, the data acquisition and image formation programs were not interfaced, which may add to the total time to make an image if continuous imaging is implemented. One way to speed this up is to reduce the number of averages needed per image, as the current number of averages used in 32. There is currently some significant electrical noise within the image acquisition circuit, and reducing this could greatly reduce the number of averages required. Noise reduction, unfortunately, is a complicated field of study, and much work would need to be done in this area to improve the platform.

While the resolution of the platform is satisfactory in a proof-of-concept study such as this one, the clinical viability would be improved if the resolution was increased. The DAS image forming algorithm chosen for this study was picked because it is well-documented and easy to implement. However, other image forming algorithms exist, and these should be explored to see if the resolution of the image could be improved [5]. It should be noted that these algorithms could also be explored as a means to increase image formation speed.

Currently, only a relatively small amount of energy can be delivered to the hand-held probe due to limitations in the optical energy the optical fiber used can handle. This results in an energy density on the surface of the tissue of ~1 mJ/cm^2, which is much less than the 20 mJ/cm^2 that has been deemed safe for this kind of application [6]. This limits the platform's application to tissue phantoms that do not optically resemble skin because

the imaging depth of the platform for tissue phantoms that do is unsatisfactorily shallow. This study demonstrated that the waveguide-transducer pair is capable of imaging burns if the energy density on the tissue surface is ~18 mJ/cm^2, so it is crucial that this energy density be achieved in an imaging probe meant for further studies. In order to facilitate this, a new optical fiber will need to be used, such as a Thorlabs M93L01 optical fiber, which has a much larger core diameter than the fiber currently used. This would make it possible the new fiber to pass more energy through it, thus achieving appropriate imaging depths in tissue that optically mimic actual burns. Unfortunately, this will necessitate redesigning the optical train within the probe, but this step is essential for clinical translation of the technology.

Throughout image analysis it was noted that there were discrepancies between the depth of the optoacoustic target measured using imaging and the actual depth measured using micro-calipers. A table of the measured depths of the targets and the depths of the targets in the images are shown in Table 5.1. These discrepancies scaled linearly with the depth of the optoacoustic target, and are shown in Figure 5.1 (R^2 of linear fit was 0.9996). The relationship can be described using Equation 5.1. Here, D_i is the depth of the object in the image, and D_a is the actual depth of the object.

$$D_a = 0.856D_i - 0.026 \tag{5.1}$$

Table 5.1 Comparison the measured depths of the optoacoustic targets in the tissue phantoms used in this study alongside their depths determined using the imaging platform.

Tissue Phantom Type	Measured Depth	Depths in Image
Electrical Tape	0.99 mm	1.2 mm
Electrical Tape	1.22 mm	1.44 mm
Burn Wound	2.18 mm	2.54 mm

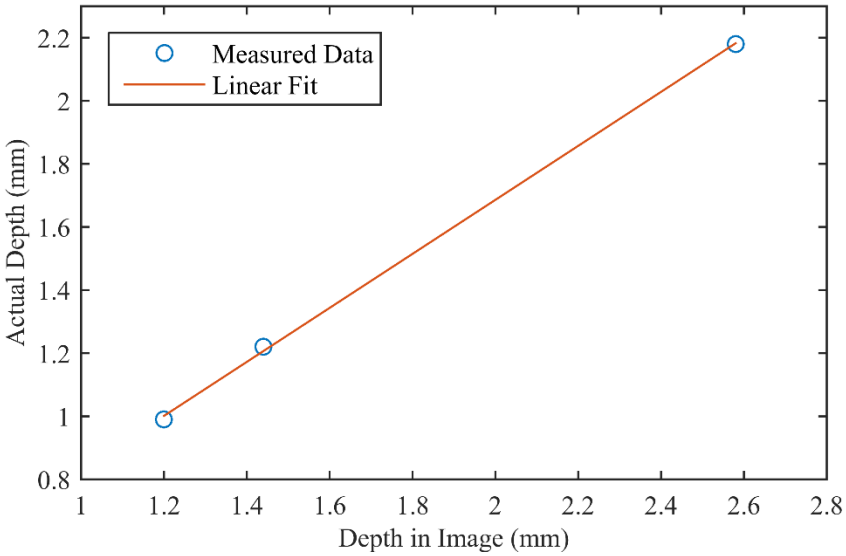

Figure 5.1. Graph showing how the depths of the optoacoustic targets in the images differed from the actual, measured depths. This was fit to a linear curve, which was described in Eq. 5.1. The R^2 value of linear fit was 0.9996.

This indicates that the imaging forming algorithm simply needs to be calibrated, and the data presented here could be used for this purpose. It is therefore proposed that a calibration factor could be implemented into the image forming algorithm to correct this issue.

5.2 Conclusions

This study has demonstrated WM-OACT as a viable form for OAI. Furthermore, it has also demonstrated that the general design of the hand-held platform presented could be viable in burn wound imaging if the energy delivered to the probe is increased. In contrast with other OACT methods that employ a spacer between the tissue and the sensor(s), this method uses a waveguide that confines light and then selectively couples light into the tissue phantom as a specific point. The advantage of this is that the thickness of the spacer can be greatly decreased, thus improving image quality.

In addition to the short-term improvements to the platform that were described in

the previous section, there are still several steps that need to be taken before this platform is ready for clinical testing. These can be thought of as long-term milestones, to be attempted after all short-term issues have been addressed. The first would be to demonstrate *in vivo* imaging of burn wounds. This would ideally involve a murine model, which is the typical choice when first demonstrating an OAI platform for imaging burn wounds *in vivo* [7-9]. This is because they are relatively cheap and easy to handle, but their skin is thinner than human skin and does not undergo the same healing process [10]. Because of this, murine models could act as a 'canary in the coal mine' test for this technology before it is advanced to more realistic models. Should the murine models prove successful, the next milestone would be imaging burns in swine, whose skin closely mimics that of humans on both the anatomical and functional level [10]. Should the platform demonstrate satisfactory imaging capabilities in swine models, pre-clinical trials could be considered.

During the development of this platform, the team, at times, reached out to other research groups that had published work demonstrating OAI in the past. During one of these communications, a member of one of these teams, Dr. Taiichiro Ida, described some issues his team had in translating a platform that had successfully imaged murine burn models into the clinic (The full communication can be seen in Appendix E). The platform his team developed was similar to the platform presented in this study in that it used single-wavelength OACT to image burn wounds. He explained that burns in some patients showed inflammation throughout the burn volume, complicating single-wavelength analysis and compromising the platforms ability to identify the zone of hyperemia. He further explained that multiwavelength imaging could be used to discriminate the zone of

coagulation and stasis from the zone of hyperemia.

Spectral analysis in OAI is not new, but to the authors' knowledge it has not been applied to imaging burn wounds. It is also well documented that oxygenated hemoglobin and deoxygenated hemoglobin have different optical absorption spectra, and therefor can be spectrally resolved using MSOT. Due to low blood flow in the zone of stasis, it is plausible that the hemoglobin loses a significant portion of its oxygen in this region, and therefore could be visualized using MSOT. It has also been reported that the absorption spectra of thermally coagulated blood differs greatly from that of heathy blood [11]. Therefore, it should be possible to differentiate between the zone of coagulation and other parts of the tissue based on coagulated blood's unique absorption spectrum. This adds yet another layer to MSOT analysis of burn wounds: it could differentiate between properly oxygenated blood the in the zone of hyperemia, oxygen-deficient blood in the zone of stasis, and thermally coagulated blood in the zone of coagulation. Because of the concerns raised about inflammation throughout the burn volume confounding single-wavelength measurements of burn wound depth, any future platform should seriously consider multi-spectra techniques for optoacoustic burn wound analysis.

5.3 Bibliography

[1] Section 14, Geophysics, Astronomy, and Acoustics; Speed of Sound in Various Media, in: D.R. Lide (Ed.), CRC Handbook of Chemistry and Physics, CRC Press, Boca Raton, Florida, 2003.

[2] K.J. Francis, B. Chinni, S.S. Channappayya, R. Pachamuthu, V.S. Dogra, N. Rao, Characterization of lens based photoacoustic imaging system, Photoacoustics 8 (2017) 37-47.

[3] P.K. Upputuri, M. Pramanik, Performance characterization of low-cost, high-speed, portable pulsed laser diode photoacoustic tomography (PLD-PAT) system, Biomedical Optics Express 6(10) (2015) 4118-4129.

[4] H.F. Zhang, K. Maslov, G. Stoica, L.V. Wang, Imaging acute thermal burns by photoacoustic microscopy, J. of Biomedical Optics, SPIE, 2006, p. 5.

[5] A. Rosenthal, V. Ntziachristos, D. Razansky, Acoustic Inversion in Optoacoustic Tomography: A Review, Current Medical Imaging Reviews 9(4) (2013) 318-336.

[6] Y. Zhou, S.V. Tripathi, I. Rosman, J. Ma, P. Hai, G.P. Linette, M.L. Council, R.C. Fields, L.V. Wang, L.A. Cornelius, Noninvasive Determination of Melanoma Depth using a Handheld Photoacoustic Probe, Journal of Investigative Dermatology 137(6) (2017) 1370-1372.

[7] T. Ida, H. Iwazaki, Y. Kawaguchi, S. Kawauchi, T. Ohkura, K. Iwaya, H. Tsuda, D. Saitoh, S. Sato, T. Iwai, Burn depth assessments by photoacoustic imaging and laser Doppler imaging, Wound Repair and Regeneration 24(2) (2015) 349-355.

[8] T. Ida, Y. Kawaguchi, S. Kawauchi, K. Iwaya, H. Tsuda, D. Saitoh, S. Sato, T. Iwai, Real-time photoacoustic imaging system for burn diagnosis, J. of Biomedical Optics, SPIE, 2014, p. 7.

[9] M.Y.S.S.H.A.D.S.Y.O.M. Obara, Measurement of burn depths in rats using multiwavelength photoacoustic depth profiling, J. of Biomedical Optics 10(6) (2005).

[10] H. Ye, S. De, Thermal injury of skin and subcutaneous tissues: A review of experimental approaches and numerical models, Burns 43(5) (2017) 909-932.

[11] J.T. Robert, H.H. Scott, A.V. John, Photoacoustic discrimination of viable and thermally coagulated blood using a two-wavelength method for burn injury monitoring, Physics in Medicine & Biology 52(7) (2007) 1815.

Appendix A

Tissue Phantom Protocols

This appendix is to show exactly how the tissue phantoms used in this study were fabricated. These protocols were adapted from previously published literature describing tissue phantoms for ultrasound and optoacoustics [1, 2]. As previously described in Chapter 4, the optical absorption and speed of sound of the phantoms were characterized. Unfortunately, the team did not have access to equipment that could characterize the optical scattering properties of the tissue.

A.1 Materials for Fabricating Tissue Phantoms

Below are tables containing information about the materials used to make each tissue phantom.

Table A.1 Materials used to fabricate hair tissue phantom

Material	Source	Amount
DI Water		3.925 mL
Methanol	A452SK, Sigma Aldrich	0.765 mL
Gelatin	G-2500, Sigma Aldrich	1.2 g

Table A.2 Materials used to fabricate electrical tape tissue phantom

Material	Source	Amount
DI Water		11.775 mL
Methanol	A452SK, Sigma Aldrich	2.295 mL
Gelatin	G-2500, Sigma Aldrich	3.6 g

Table A.3 Materials used to fabricate dermis tissue phantom

Material	Source	Amount
Direct Red 81, $4.8 \cdot 10^{-6}$ M	195251, Sigma Aldrich	2.5mL
Methanol	A452SK, Sigma Aldrich	0.765mL
Intralipid, 20%	0338-1519-09, Fresenius Kabi	1.425mL
Gelatin	G-2500, Sigma Aldrich	1.2g

Table A.4 Materials used to fabricate hyperemic tissue phantom

Material	Source	Amount
Direct Red 81, $1.98 \cdot 10^{-3}$ M	195251, Sigma Aldrich	2.5mL
Methanol	A452SK, Sigma Aldrich	0.765mL
Intralipid, 20%	0338-1519-09, Fresenius Kabi	1.425mL
Gelatin	G-2500, Sigma Aldrich	1.2g

A.2 Materials for Fabricating Tissue Phantoms

Below is the procedure used to fabricate the tissue phantoms

1. Mix liquids in beaker. Bring to 55^{o}C, applying *light* mixing with stir bar (~60 rpm for small volumes).

- Stir bar should be rotating at absolute minimum speed. Stirring is needed in the procedure, should be kept to a minimum to keep the solution from becoming aerated.
- The solution should be covered to minimize fluid loss.
- An aluminum foil barrier should be made around the beaker to minimize heat loss due to air flow.

2. Keeping the stir bar rotation speed at a minimum, add the gelatin.

- Heat is your best friend when working the gelatin into the solution. Don't get impatient and increase the stir bar rotation speed. You will regret it later.
- Keep solution temperature between 50-60^{o}C

3. While the gelatin is being worked into the solution, bring a hot water bath to a boil. This needs to fit inside the vacuum desiccator.

- The hot water bath will keep the solution warm while in the desiccator. Otherwise, the solution may coagulate as gas is escaping. This creates a porous, and useless, phantom.

4. Place water bath in the vacuum desiccator, and place the beaker of solution in the bath. Place under vacuum for 10 minutes.

For hair tissue phantoms:

5. Remove beaker from vacuum desiccator, pour into mold. Place mold in sealable bag containing wet paper towels within 4°C fridge to mitigate evaporative fluid loss. Use as soon as the phantom fluid is cool.

For other tissue phantoms:

5. Remove beaker from vacuum desiccator, pour into mold. Place cover plate over mold to remove excess fluid and hold until the fluid starts to set. Place mold in sealable bag containing wet paper towels within 4°C fridge to mitigate evaporative fluid loss. Use as

soon as the phantom fluid is cool.

A.5 Bibliography

[1] A.I. Chen, M.L. Balter, M.I. Chen, D. Gross, S.K. Alam, T.J. Maguire, M.L. Yarmush, Multilayered tissue mimicking skin and vessel phantoms with tunable mechanical, optical, and acoustic properties, Medical Physics 43(6) (2016) 3117-3131.

[2] J.R. Cook, R.R. Bouchard, S.Y. Emelianov, Tissue-mimicking phantoms for photoacoustic and ultrasonic imaging, Biomedical Optics Express 2(11) (2011) 3193-3206.

Appendix B

Platform Control

As described in Chapter 4, data acquisition was automated using a LabVIEW program. The program operated by firing the laser and recording signals received from the transducer elements that made up that transducer array. A multiplexer board was used to manage the 32 individual channels coming from the transducer and selectively pass them to a 4-channel digital oscilloscope. This was accomplished using 4 multiplexer boards. In brief, each multiplexer board contained eight op-amps and two multiplexer chips. Each op-amp was connected to one channel from the transducer. One multiplexer was used to selectively enable the op-amp to be sampled, and the other selectively passed to signal from the enabled op-amp on toward to oscilloscope to be recorded. Which op-amp the multiplexer chips selected was controlled by passing three digital high-low signals to them, with each combination (i.e. low-low-high or high-low-high) associated with a different op amp. This was accomplished using an Arduino Mega, and the code to control the Arduino can be found in Appendix B.1. The designs for the multiplexer boards can be seen in Appendix B.2, and the schematic for the LabVIEW program can be found in Appendix B.3.

B.1 Code for Controlling Arduino

Below is the code used by the Arduino to control the multiplexer chips. The code takes an input value (from 1 to 8) and passes three digital signals to the four multiplexer boards, resulting in 12 total digital outputs.

```
/*******************************
```

```
bPAT multiplexer index controller

Control the indexed multiplexer
output channel according to values
ready via serial communication

Mason Schellenberg
09-27-2017
v1.1

Input command starts with '<'
Index number = 1,2,3,...9
End command with '>'

Index = 9 yields a confirmation response to
confirm that communications are active.
E.g.:

Outputs    Responses
<1>        COM_0 selected
<8>        COM_7 selected
<9>        Comm. active

Sketch controls outputs of pins 2, 7, 12
Baud rate is 115,200

*********************************/

#define ADDAa 23
#define ADDBa 25
#define ADDCa 27
#define ADDAb 29
#define ADDBb 31
#define ADDCb 33
#define ADDAc 35
#define ADDBc 37
#define ADDCc 39
#define ADDAd 41
#define ADDBd 43
#define ADDCd 45

String pH1 = "";
char c;
int ndx = 0;

void setup() {
  // initialize the digital pin as an output.
  pinMode(ADDAa, OUTPUT);
  pinMode(ADDBa, OUTPUT);
  pinMode(ADDCa, OUTPUT);
  pinMode(ADDAb, OUTPUT);
  pinMode(ADDBb, OUTPUT);
  pinMode(ADDCb, OUTPUT);
  pinMode(ADDAc, OUTPUT);
  pinMode(ADDBc, OUTPUT);
```

```
  pinMode(ADDCc, OUTPUT);
  pinMode(ADDAd, OUTPUT);
  pinMode(ADDBd, OUTPUT);
  pinMode(ADDCd, OUTPUT);
  Serial.begin(115200);
}

void loop()
{
  // put your main code here, to run repeatedly:
   pH1 = "";

  ReceiveDataPacket();

  ndx = satoi(pH1);

  if (ndx == 1){
        digitalWrite(ADDAa,LOW);
        digitalWrite(ADDBa,LOW);
        digitalWrite(ADDCa,LOW);
        digitalWrite(ADDAb,LOW);
        digitalWrite(ADDBb,LOW);
        digitalWrite(ADDCb,LOW);
        digitalWrite(ADDAc,LOW);
        digitalWrite(ADDBc,LOW);
        digitalWrite(ADDCc,LOW);
        digitalWrite(ADDAd,LOW);
        digitalWrite(ADDBd,LOW);
        digitalWrite(ADDCd,LOW);
        Serial.println("COM_0 selected");
  } else if (ndx == 2){
        digitalWrite(ADDAa,HIGH);
        digitalWrite(ADDBa,LOW);
        digitalWrite(ADDCa,LOW);
        digitalWrite(ADDAb,HIGH);
        digitalWrite(ADDBb,LOW);
        digitalWrite(ADDCb,LOW);
        digitalWrite(ADDAc,HIGH);
        digitalWrite(ADDBc,LOW);
        digitalWrite(ADDCc,LOW);
        digitalWrite(ADDAd,HIGH);
        digitalWrite(ADDBd,LOW);
        digitalWrite(ADDCd,LOW);
        Serial.println("COM_1 selected");
  } else if (ndx == 3){
        digitalWrite(ADDAa,LOW);
        digitalWrite(ADDBa,HIGH);
        digitalWrite(ADDCa,LOW);
        digitalWrite(ADDAb,LOW);
        digitalWrite(ADDBb,HIGH);
        digitalWrite(ADDCb,LOW);
        digitalWrite(ADDAc,LOW);
        digitalWrite(ADDBc,HIGH);
        digitalWrite(ADDCc,LOW);
        digitalWrite(ADDAd,LOW);
        digitalWrite(ADDBd,HIGH);
```

```
        digitalWrite(ADDCd,LOW);
        Serial.println("COM_2 selected");
    } else if (ndx == 5){
        digitalWrite(ADDAa,LOW);
        digitalWrite(ADDBa,LOW);
        digitalWrite(ADDCa,HIGH);
        digitalWrite(ADDAb,LOW);
        digitalWrite(ADDBb,LOW);
        digitalWrite(ADDCb,HIGH);
        digitalWrite(ADDAc,LOW);
        digitalWrite(ADDBc,LOW);
        digitalWrite(ADDCc,HIGH);
        digitalWrite(ADDAd,LOW);
        digitalWrite(ADDBd,LOW);
        digitalWrite(ADDCd,HIGH);
        Serial.println("COM_4 selected");
    } else if (ndx == 4){
        digitalWrite(ADDAa,HIGH);
        digitalWrite(ADDBa,HIGH);
        digitalWrite(ADDCa,LOW);
        digitalWrite(ADDAb,HIGH);
        digitalWrite(ADDBb,HIGH);
        digitalWrite(ADDCb,LOW);
        digitalWrite(ADDAc,HIGH);
        digitalWrite(ADDBc,HIGH);
        digitalWrite(ADDCc,LOW);
        digitalWrite(ADDAd,HIGH);
        digitalWrite(ADDBd,HIGH);
        digitalWrite(ADDCd,LOW);
        Serial.println("COM_3 selected");
    } else if (ndx == 7){
        digitalWrite(ADDAa,LOW);
        digitalWrite(ADDBa,HIGH);
        digitalWrite(ADDCa,HIGH);
        digitalWrite(ADDAb,LOW);
        digitalWrite(ADDBb,HIGH);
        digitalWrite(ADDCb,HIGH);
        digitalWrite(ADDAc,LOW);
        digitalWrite(ADDBc,HIGH);
        digitalWrite(ADDCc,HIGH);
        digitalWrite(ADDAd,LOW);
        digitalWrite(ADDBd,HIGH);
        digitalWrite(ADDCd,HIGH);
        Serial.println("COM_6 selected");
    } else if (ndx == 6){
        digitalWrite(ADDAa,HIGH);
        digitalWrite(ADDBa,LOW);
        digitalWrite(ADDCa,HIGH);
        digitalWrite(ADDAb,HIGH);
        digitalWrite(ADDBb,LOW);
        digitalWrite(ADDCb,HIGH);
        digitalWrite(ADDAc,HIGH);
        digitalWrite(ADDBc,LOW);
        digitalWrite(ADDCc,HIGH);
        digitalWrite(ADDAd,HIGH);
        digitalWrite(ADDBd,LOW);
```

```
        digitalWrite(ADDCd,HIGH);
        Serial.println("COM_5 selected");;
  } else if (ndx == 8){
        digitalWrite(ADDAa,HIGH);
        digitalWrite(ADDBa,HIGH);
        digitalWrite(ADDCa,HIGH);
        digitalWrite(ADDAb,HIGH);
        digitalWrite(ADDBb,HIGH);
        digitalWrite(ADDCb,HIGH);
        digitalWrite(ADDAc,HIGH);
        digitalWrite(ADDBc,HIGH);
        digitalWrite(ADDCc,HIGH);
        digitalWrite(ADDAd,HIGH);
        digitalWrite(ADDBd,HIGH);
        digitalWrite(ADDCd,HIGH);
        Serial.println("COM_7 selected");
  } else if (ndx == 9){
     Serial.println("Comm. Active");
  }
}

/*************************************
**************************************
ReceiveDataPacket Function
**************************/
void ReceiveDataPacket() {
  while (Serial.available() > 0) {
    c = Serial.read();
    if (c == '<') {
      while (c != '>') {
          if (Serial.available() > 0) {
            c = Serial.read();

            if (c != '>') {
              pH1 += c;
            }
            }

    }
      // Uncomment the next two commands to confirm communications
      //Serial.print("Received string: ");
      //Serial.println( pH1 );
  }
  }
}




/*************************************
satoi - convert string to int
****************************/
int satoi( String str ) {
  int r = 0;
  int len = str.length();
```

```
  for (int i=0; i<len; i++) {
    // check if this is a number
    if (str[i] < 0x3a && str[i] > 0x2f) {
      // str[i] is an ASCII number
      r = r*10;
      r+= (str[i]-0x30);
    } else {
      i = len; // exit
      r = -1;
      break;
    }
  }
  return r;
}
```

B.2 Multiplexer Board Design

This section is to provide a detailed description of how the multiplexer boards were made. Each was the same, and consisted of these general components:

- Power. Supplied +/- 5V and ground and powered all op-amps and multiplexer chips.
- Arduino inputs. Connected digital signals from Arduino to multiplexer chips.
- Signal inputs. Total of eight signals received from the transducer, each leading to one op-amp.
- Eight op-amps, which amplified the signals from the transducer
- Two multiplexer chips, which controlled which op-amp was selected to be connected to the digital oscilloscope.
- One BNC output connection, connected to one of the multiplexers, which carried the signal to the digital oscilloscope.

An analog filter was designed into the board (highlighted in grey), but was not incorporated due to noise. Instead, a wire was placed between the two connections labeled

'Jumper'. It short circuited the filter component and passed the signal straight to the BNC connection. A schematic of the multiplexer board can be seen in Figure B.1.

A list of the sources for the components is found here:

- C1, 100 pF: CL05C101JC51PNC, Samsung Electro-Mechanics
- C2, 100 nF: GRM155R62A104KE14D, Murata Electronics North America
- R1, 499 Ω: RC1206FR-07499RL, Yageo
- R2, 49.9 Ω: RC1206FR-0749R9L, Yageo
- R3, 1 kΩ: RC1206FR-071KL, Yageo
- R4, 26.1 Ω: RC1206FR-0726R1L, Yageo
- Op-amp: AD8099ARDZ-REEL7, Analog Devices Inc.
- Multiplexer chip: MAX4051ESE+, Maxim Integrated

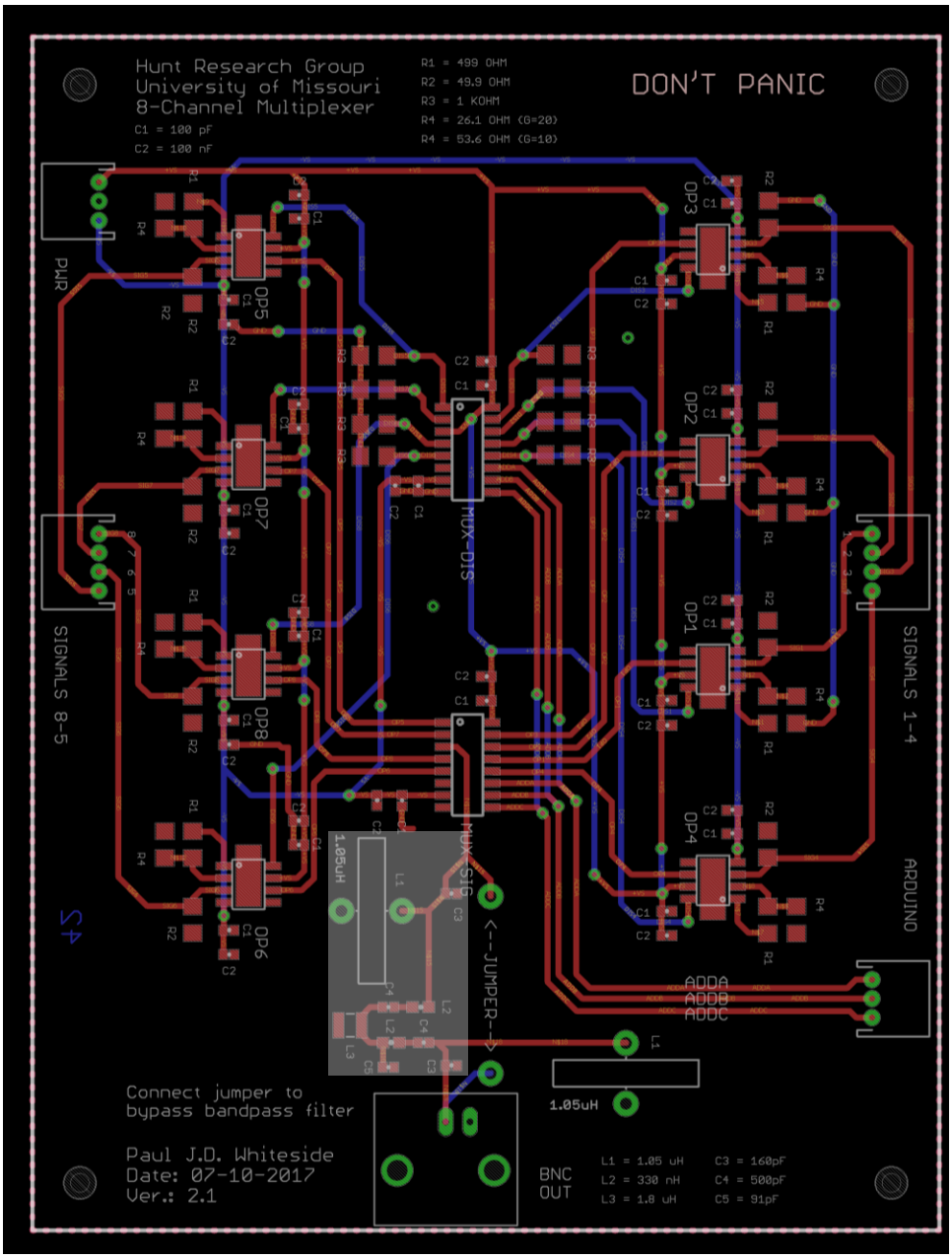

Figure B.1. Schematic of the multiplexer board. Red lines are connections printed on the top of the board, blue lines are connections on the bottom, and green are through holes. The +/- 5V power supply connection is marked 'PWR'. The three channels coming from the Arduino are labeled 'ADDA','ADDB', and 'ADDC'. Op-amps are labeled 'OP#', with # being the designated # of the op-amp. The multiplexer chip that enables op-amps is labeled 'MUX-DIS', and the multiplexer that passes the signal to the BNC connection is labeled 'MUX-SIG'. The connection for the BNC output is labeled 'BNC OUT'.

B.3 LabVIEW Control Program

This section is to provide some context to how the LabVIEW program controlled data acquisition and processing. The primary block diagram from the LabVIEW program can be seen in Figure B.2. This block shows how data from the oscilloscope was collected, processed, and saved. As described previously in Chapter 4, the program began with (1) selecting the first set of op-amps and (2) firing the laser. These constitute the first two frames of the block sequence with the one shown in B.2. After data is collected, the next set of op-amps are selected, the laser is fired, and data is collected again. This repeats until all op-amps are sampled. If multiple scans are needed, the entire process will run again until all scans are completed.

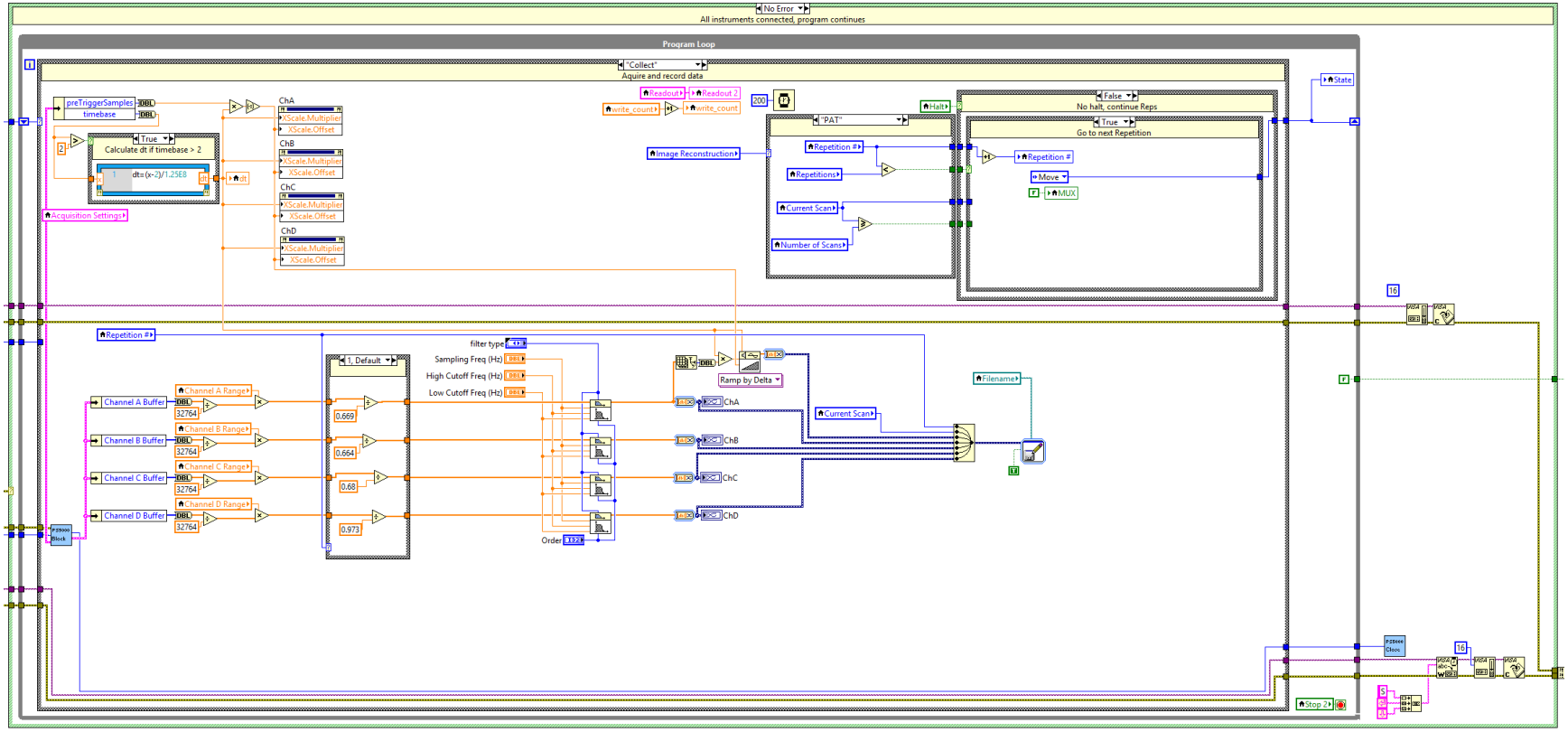

Figure B.2. A block diagram showing how data is collected from the oscilloscope, processed, and then saved. First, once the trigger threshold has been reached, a total of 1500 samples are taken at predetermined, regular time intervals. Because the data collected is raw integer values from the analog-to-digital conversion, they are multiplied by some scaling factor. The signals are then multiplied again to scale to discrepancies between how the signals were amplified by the op-amps. The signals are then filtered, graphed, and saved to a file along with information that identifies the particular set of data with a particular scan and group of op-amps. Also saves is the predetermined time intervals. After this, the program alters the variable which controls op-amps selection and scan identification, which are used in subsequent frames.

Appendix C

Image Formation Algorithms

This appendix is meant to detail how MATLAB algorithms are used to generate images from collected optoacoustic signals using DAS image formation techniques. For image function, the user specifies a file, with a predetermined structure, that has 32 signals from each transducer element. The time trace is also read. The signals are then organized and averaged. Finally, the data is transferred to the DAS algorithm which produces the image in the form of an array. This array is the output of the function.

C.1 Algorithm for Hair Tissue Phantom

```
function [Img] = CFDAS_Rec_PMMA_20180405

%============================================================
% User Inputs
%============================================================

Width = 6.35e-3;                                % [m]
Depth = 4.8e-3;                                 % [m]
element_width = 0.15e-3;                        % [m]
element_spacing = 0.05e-3;                      % [m]
c_tissue = 1615;                                % [m/s] (MWS-2-147)
c_PMMA = 2647;                                  % [m/s]
Resolution = 0.0025e-3;

dx = Resolution;                                % Resolution on x axis [m]
dy = dx;                                        % Resolution on y axis [m]

PMMA_Depth = 1.8e-3;                            % [m]

%============================================================
% Load and Sort Data
%============================================================

% Loads data detected by sensor

data = csvread(uigetfile,1,1);
```

```
Rep_Tok = find(data(:,1));
% Scan_Tok = find(data(:,2));
Scans = data(Rep_Tok(end),2);
% Time = cell(length(Rep_Tok),1);

Time = data(1:Rep_Tok(2)-1,3);

for k = 0:Scans-1
   count = 1;
   for i = 1:8
      if k == Scans-1 && i == 8
         Trans{i,1} = data(Rep_Tok(end):end,4);
         Trans{i+8,1} = data(Rep_Tok(end):end,5);
         Trans{i+16,1} = data(Rep_Tok(end):end,6);
         Trans{i+24,1} = data(Rep_Tok(end):end,7);
      else
         Trans{i,1} = data(Rep_Tok(i+8*k):Rep_Tok(i+8*k+1),4);
         Trans{i+8,1} = data(Rep_Tok(i+8*k):Rep_Tok(i+8*k+1),5);
         Trans{i+16,1} = data(Rep_Tok(i+8*k):Rep_Tok(i+8*k+1),6);
         Trans{i+24,1} = data(Rep_Tok(i+8*k):Rep_Tok(i+8*k+1),7);
      end
      count = count + 1;
   end
   Scan{k+1,1} = Trans;
   clear Trans

end

Scan_32 = Scan{32};
for i = 1:4
   clear Tok2
   Tok2 = Scan_32{8*i};
   Tok2 = vertcat(Tok2,0);
   Scan_32{i*8} = Tok2;
end
Scan{32} = Scan_32;

%============================================================
% Average Data
%============================================================

for i = 1:32 % for each transducer element
   Element_Sum = 0; % initalize
   for k = 1:Scans
      clear Tok1 Tok2
      Tok1 = Scan{k};
      Tok2 = Tok1{i}; % is one element off at i = 8, k = 32. Why?
      Element_Sum = Element_Sum + Tok2;
   end
```

```
   Element_Sum(Element_Sum<0) = 0;
   Element_Sum = Element_Sum(1:end-1); % to fit time array
   Average{i,1} = Element_Sum./Scans;
   clear Element_Sum
end

Transducer = Average;

number_elements = length(Transducer);
element_position = zeros(number_elements,1);
for i = 1:number_elements
   element_position(i,1) = (i-1)*(element_width+element_spacing) ...
      + element_width/2;
end

%============================================================
% DAS
% Focus each face to a point using delay, sum responses.
%============================================================

Img = zeros(round(Depth/dy),round(Width/dx));

for i = 1:round(Width/dx)
   for j = 719:round(Depth/dy)
      Signals = 0;

      for k = 1:number_elements %%%
         Distance_total = sqrt( ((i*dx-dx/2)-(element_position(k,1)))^2 ...
            + (j*dy-dy/2)^2);
         Angle = 90 - atand(abs((i*dx-dx/2)-(element_position(k,1))) ...
            / abs((j*dy-dy/2)));
         Distance_PMMA = abs(PMMA_Depth / sind(Angle));
         if Distance_total <= Distance_PMMA
            Distance_PMMA = Distance_total;
            Distance_tissue = 0;
         else
            Distance_tissue = Distance_total - Distance_PMMA;
         end
         Delay = Distance_PMMA / c_PMMA + Distance_tissue / c_tissue;
         scan = Transducer{k};
         Signals(k,1) = interp1(Time,scan,Delay,'spline');
      end
      Sum = sum(Signals);
      Signals_Sq = Signals.^2;
      CF = Sum^2 / (number_elements * sum(Signals_Sq));  %%%
      Img(j,i) = Sum * CF;                                % CF-DAS Image

   end
end
```

```
% positivity condition
Img(Img<0) = 0;
Img = Img(719:end,:);


end
```

C.2 Algorithm for Electrical Tape Tissue Phantom

```
% ============================================================
% User Inputs
% ============================================================

Width = 6.35e-3;                                    % [m]
Depth = 3.8e-3;                                     % [m]
element_width = 0.15e-3;                            % [m]
element_spacing = 0.05e-3;                          % [m]
c_tissue = 1615;                                    % [m/s] (MWS-2-147)
c_PMMA = 2647;                                      % [m/s]
% Resolution = 0.05e-3;

dx = 250e-6;                        % Nyquist criterion for lateral resolution of 550um
dy = 30e-6;                 % Nyquist criterion for axial resolution of 77um

PMMA_Depth = 1.8e-3;                                % [m]

% ============================================================
% Load and Sort Data
% ============================================================

% Loads data detected by sensor

data = csvread(uigetfile,1,1);
Rep_Tok = find(data(:,1));
% Scan_Tok = find(data(:,2));
Scans = data(Rep_Tok(end),2);
% Time = cell(length(Rep_Tok),1);

Time = data(1:Rep_Tok(2)-1,3);

for k = 0:Scans-1
   count = 1;
   for i = 1:8
      if k == Scans-1 && i == 8
         Trans{i,1} = data(Rep_Tok(end):end,4);
         Trans{i+8,1} = data(Rep_Tok(end):end,5);
         Trans{i+16,1} = data(Rep_Tok(end):end,6);
```

```
        Trans{i+24,1} = data(Rep_Tok(end):end,7);
      else
        Trans{i,1} = data(Rep_Tok(i+8*k):Rep_Tok(i+8*k+1),4);
        Trans{i+8,1} = data(Rep_Tok(i+8*k):Rep_Tok(i+8*k+1),5);
        Trans{i+16,1} = data(Rep_Tok(i+8*k):Rep_Tok(i+8*k+1),6);
        Trans{i+24,1} = data(Rep_Tok(i+8*k):Rep_Tok(i+8*k+1),7);
      end
      count = count + 1;
   end
   Scan{k+1,1} = Trans;
   clear Trans

end

Scan_32 = Scan{32};
for i = 1:4
   clear Tok2
   Tok2 = Scan_32{8*i};
   Tok2 = vertcat(Tok2,0);
   Scan_32{i*8} = Tok2;
end
Scan{32} = Scan_32;

% ============================================================
% Average Data
%============================================================

for i = 1:32 % for each transducer element
   Element_Sum = 0; % initalize
   for k = 1:Scans
      clear Tok1 Tok2
      Tok1 = Scan{k};
      Tok2 = Tok1{i}; % is one element off at i = 8, k = 32. Why?
      Element_Sum = Element_Sum + Tok2;
   end
   Element_Sum(Element_Sum<0) = 0;
   Element_Sum = Element_Sum(1:end-1); % to fit time array
   Average{i,1} = Element_Sum./Scans;
   clear Element_Sum
end

Transducer = Average;

number_elements = length(Transducer);
element_position = zeros(number_elements,1);
for i = 1:number_elements
   element_position(i,1) = (i-1)*(element_width+element_spacing) ...
      + element_width/2;
end
```

```
%============================================================
% DAS
% Focus each face to a point using delay, sum responses.
%============================================================
tic

Img = zeros(round(Depth/dy),round(Width/dx));

for i = 1:round(Width/dx)
   for j = 60:round(Depth/dy)
      Signals = 0;

      for k = 1:number_elements %%%
         Distance_total = sqrt( ((i*dx-dx/2)-(element_position(k,1)))^2 ...
            + (j*dy-dy/2)^2);
         Angle = 90 - atand(abs((i*dx-dx/2)-(element_position(k,1))) ...
            / abs((j*dy-dy/2)));
         Distance_PMMA = abs(PMMA_Depth / sind(Angle));
         if Distance_total <= Distance_PMMA
            Distance_PMMA = Distance_total;
            Distance_tissue = 0;
         else
            Distance_tissue = Distance_total - Distance_PMMA;
         end
         Delay = Distance_PMMA / c_PMMA + Distance_tissue / c_tissue;
         scan = Transducer{k};
         Signals(k,1) = interp1(Time,scan,Delay,'spline');
      end
      Sum = sum(Signals);
      Signals_Sq = Signals.^2;
      CF = Sum^2 / (number_elements * sum(Signals_Sq));  %%%
      Img(j,i) = Sum * CF;                                % CF-DAS Image

   end
end

% positivity condition
Img = Img(60:end,:);

toc

end
```

C.3 Algorithm for Burn Wound Tissue Phantom

```
% ============================================================
% User Inputs
```

```
% ============================================================

Width = 6.35e-3;                                    % [m]
Depth = 5e-3;                                       % [m]
element_width = 0.15e-3;                            % [m]
element_spacing = 0.05e-3;                          % [m]
c_tissue = 1615;                                    % [m/s] (MWS-2-147)
c_PMMA = 2647;                                      % [m/s]
% Resolution = 0.05e-3;

dx = 250e-6;                    % Nyquist criterion for lateral resolution of 550um
dy = 30e-6;                     % Nyquist criterion for axial resolution of 77um

PMMA_Depth = 1.8e-3;                        % [m]

% ============================================================
% Load and Sort Data
% ============================================================

% Loads data detected by sensor

data = csvread(uigetfile,1,1);
Rep_Tok = find(data(:,1));
% Scan_Tok = find(data(:,2));
Scans = data(Rep_Tok(end),2);
% Time = cell(length(Rep_Tok),1);

Time = data(1:Rep_Tok(2)-1,3);

for k = 0:Scans-1
   count = 1;
   for i = 1:8
      if k == Scans-1 && i == 8
         Trans{i,1} = data(Rep_Tok(end):end,4);
         Trans{i+8,1} = data(Rep_Tok(end):end,5);
         Trans{i+16,1} = data(Rep_Tok(end):end,6);
         Trans{i+24,1} = data(Rep_Tok(end):end,7);
      else
         Trans{i,1} = data(Rep_Tok(i+8*k):Rep_Tok(i+8*k+1),4);
         Trans{i+8,1} = data(Rep_Tok(i+8*k):Rep_Tok(i+8*k+1),5);
         Trans{i+16,1} = data(Rep_Tok(i+8*k):Rep_Tok(i+8*k+1),6);
         Trans{i+24,1} = data(Rep_Tok(i+8*k):Rep_Tok(i+8*k+1),7);
      end
      count = count + 1;
   end
   Scan{k+1,1} = Trans;
   clear Trans

end
```

```
Scan_32 = Scan{32};
for i = 1:4
   clear Tok2
   Tok2 = Scan_32{8*i};
   Tok2 = vertcat(Tok2,0);
   Scan_32{i*8} = Tok2;
end
Scan{32} = Scan_32;

% ============================================================
% Average Data
% ============================================================


for i = 1:32 % for each transducer element
   Element_Sum = 0; % initalize
   for k = 1:Scans
      clear Tok1 Tok2
      Tok1 = Scan{k};
      Tok2 = Tok1{i}; % is one element off at i = 8, k = 32. Why?
      Element_Sum = Element_Sum + Tok2;
   end
   Element_Sum(Element_Sum<0) = 0;
   Element_Sum = Element_Sum(1:end-1); % to fit time array
   Average{i,1} = Element_Sum./Scans;
   clear Element_Sum
end

Transducer = Average;

number_elements = length(Transducer);
element_position = zeros(number_elements,1);
for i = 1:number_elements
   element_position(i,1) = (i-1)*(element_width+element_spacing) ...
      + element_width/2;
end

% ============================================================
% DAS
% Focus each face to a point using delay, sum responses.
% ============================================================
tic

Img = zeros(round(Depth/dy),round(Width/dx));

for i = 1:round(Width/dx)
   for j = 60:round(Depth/dy)
      Signals = 0;
```

```
      for k = 1:number_elements %%%
         Distance_total = sqrt( ((i*dx-dx/2)-(element_position(k,1)))^2 ...
            + (j*dy-dy/2)^2);
         Angle = 90 - atand(abs((i*dx-dx/2)-(element_position(k,1))) ...
            / abs((j*dy-dy/2)));
         Distance_PMMA = abs(PMMA_Depth / sind(Angle));
         if Distance_total <= Distance_PMMA
            Distance_PMMA = Distance_total;
            Distance_tissue = 0;
         else
            Distance_tissue = Distance_total - Distance_PMMA;
         end
         Delay = Distance_PMMA / c_PMMA + Distance_tissue / c_tissue;
         scan = Transducer{k};
         Signals(k,1) = interp1(Time,scan,Delay,'spline');
      end
      Sum = sum(Signals);
      Signals_Sq = Signals.^2;
      CF = Sum^2 / (number_elements * sum(Signals_Sq));  %%%
      Img(j,i) = Sum * CF;                                    % CF-DAS Image

   end
end

% positivity condition
Img = Img(60:end,:);

toc

end
```

Appendix D

Monte Carlo Photon Transport Simulations

This appendix is meant to provide detailed information about the file used for the Monte Carlo simulations for photon transport in generic skin tissue. The simulations software used was developed by another group [1, 2]. The original software code only simulated a direct incidence angle, so the software was altered to simulate oblique angles at 30° and 60°. These three simulation codes were then used to simulate light transport in skin tissue. The code used to describe the tissue within the simulation can be seen in the following section. The optical properties were chosen for light with a wavelength of 556 nm [3-6]. The results of the simulations were then passed to a post-processing program which extracted light absorption data with respect to distance from the center of the simulated cylinder of tissue and depth within the tissue. Afterwards, these results were plotted and further analyzed it MATLAB.

D.1 Code Describing Generic Skin Tissue

```
####
# Simulation of light transport in human skin at 556 nm, assumed to be good approximation # of 532nm.
# Refractive index of hypodermis assumed to be that of subcut. fat.
####

1.0                                     # file version
1                                       # number of runs

### Specify data for run 1
Skin1.mco       A                       # output filename, ASCII/Binary
1000000                         # No. of photons
50E-4   50E-4                           # dz, dr [cm]
59      150     30                      # No. of dz, dr & da.
```

```
3                                                   # No. of layers
# n     mua     mus     g       d                   # One line for each layer,
1.0                                                 # n for medium above.
1.44    53.64   303.63  0.8     0.01                # Epidermis
1.39    1.56    197.75  0.8     0.11                # Dermis
1.46    1.67    85.65   0.8     0.175               # Hypodermis
1.0                                                 # n for medium below.
```

D.2 Bibliograpgy

[1] L. Wang, S.L. Jacques, L. Zheng, Conv—convolution for responses to a finite diameter photon beam incident on multi-layered tissues, Computer Methods and Programs in Biomedicine 54(3) (1997) 141-150.

[2] L. Wang, S.L. Jacques, L. Zheng, MCML—Monte Carlo modeling of light transport in multi-layered tissues, Computer Methods and Programs in Biomedicine 47(2) (1995) 131-146.

[3] A.I. Chen, M.L. Balter, M.I. Chen, D. Gross, S.K. Alam, T.J. Maguire, M.L. Yarmush, Multilayered tissue mimicking skin and vessel phantoms with tunable mechanical, optical, and acoustic properties, Medical Physics 43(6) (2016) 3117-3131.

[4] L.J. Steven, Optical properties of biological tissues: a review, Physics in Medicine & Biology 58(11) (2013) R37.

[5] D. Huafeng, Q.L. Jun, A.W. William, J.K. Peter, H. Xin-Hua, Refractive indices of human skin tissues at eight wavelengths and estimated dispersion relations between 300 and 1600 nm, Physics in Medicine & Biology 51(6) (2006) 1479.

[6] H.-C. Lee, Introduction to Color Imaging Science, Cambridge University Press2005.

Appendix E

Communication with Dr. Taiichiro Ida

During the course of completing the project, the team reached out to several other groups that were conducting research in similar areas. One of the groups had recently published a paper demonstrating a hand-held platform for burn would imaging [1]. The team had some questions about the level of contrast that was achieved in the images, and the corresponding author, Dr. Ida, was contacted. This lead to a brief but informative conversation about his groups struggles in translating their platform, which had performed excellently in murine models, to human trials. One of the main issues, he said, was that in some burns the entire wound volume would become inflamed, complicating single-wavelength burn wound imaging. Because of this, he noted that multispectral burn wound imaging needs to be explored to see if it can differentiate between the different burn wound zones. This is a sentiment that the team had discussed previously, and further highlights the necessity of the technique. While multispectral OAI is well established it has not been applied to burn wounds. Below is the communication the team had with Dr. Ida, in full.

From: Schellenberg, Mason W. (MU-Student)
<mason.schellenberg@mail.missouri.edu>
Sent: Saturday, March 3, 2018 3:01 AM
To: Ida, Taiichiro <Taiichiro.Ida@advantest.com>
Subject: Question about manuscript Titled 'Burn depth assessments by photoacoustic imaging and laser Doppler imaging'

Dear Dr. Ida,

My name is Mason Schellenberg and I am a graduate student working with photoacoustic tomography. I am interested in the data you and your team published in

an article entitled 'Burn depth assessments by photoacoustic imaging and laser Doppler imaging', published in Wound Repair and Regeneration in 2016. Specifically, I am wondering the ratio of the signals from the blood vessels under the burn (used to determine burn depth) to the surrounding tissue (shown in Figure 3). Thank you for reading.

Sincerely,
Mason Schellenberg

From: Ida, Taiichiro <taiichiro.ida@advantest.com>
Sent: Wednesday, March 7, 2018 3:36:11 AM
To: Schellenberg, Mason W. (MU-Student)
Subject: RE: Question about manuscript Titled 'Burn depth assessments by photoacoustic imaging and laser Doppler imaging'

Dear Mr. Mason Schellenberg,

Thank you for your email. Is your question that the amplitude of PA signals originating from blood vessels under the injured tissue are not same among PA images (c1 to c7)? I think that the PA amplitude of c1 and c2 were strong due to inflammation. In DDB and DB models (c4 to c7) some blood vessels were enlarged due to thermal damage and PA amplitude became strong. If you have any quetisons, do not hesitate to ask me.

Best regards,
Taiichiro Ida

From: Schellenberg, Mason W. (MU-Student)
<mason.schellenberg@mail.missouri.edu>
Sent: Wednesday, March 7, 2018 11:13 PM
To: Ida, Taiichiro <Taiichiro.Ida@advantest.com>
Subject: RE: Question about manuscript Titled 'Burn depth assessments by photoacoustic imaging and laser Doppler imaging'

Dear Dr. Ida,

Thank you for the reply. I understand that the strong signals you mentioned are due to

inflammation and hyperperfusion. Perhaps I did not state my inital question clearly. I am wondering how much stronger the PA signal from the inflammed area was than from the surrounding tissue. By surrounding tissue I mean areas just above or below the zone of hyperemia. If I need to explain myself more, do not hesitate to ask.

Sincerely,
Mason Schellenberg

From: Ida, Taiichiro <taiichiro.ida@advantest.com>
Sent: Saturday, March 10, 2018 6:03:58 AM
To: Schellenberg, Mason W. (MU-Student)
Subject: RE: Question about manuscript Titled 'Burn depth assessments by photoacoustic imaging and laser Doppler imaging'

Dear Mr. Mason Schellenberg,

I understood your meaning. The signals which I used to determine burn depth is originating from hyperemia. The area above the zone of hyperemia is the zone of stasis in which blood occlusion is occurred. So the PA signals from the area above hyperemia can not be observed. Below the zone of hyperemia the inflammation is occurred due to the thermal damage. I think it would be possible to divide PA signals into hyperemia and inflammation by using high frequency ultrasound sensor and multi wavelength PA imaging. In my paper the axial resolution is several hundred micro meter. I think the resolution is not enough to distinguish hyperemia and inflammation clearly. Did you develop new photoacoustic tomographic system? If you have published paper about your system, please send me. I am interested in your research.

Best regards,
Taiichiro Ida

From: Schellenberg, Mason W. (MU-Student)
<mason.schellenberg@mail.missouri.edu>
Sent: Sunday, March 11, 2018 3:03 AM
To: Ida, Taiichiro <Taiichiro.Ida@advantest.com>
Subject: Re: Question about manuscript Titled 'Burn depth assessments by photoacoustic imaging and laser Doppler imaging'

Dear Dr. Taiichiro Ida,

I am currently developing a PAT system. I am having trouble testing the device, which is why I have reached out to you. I am using a tissue phantom which has two layers. The first layer simulates normal dermis (to approximate the zone of stasis), and the bottom layer simulates dermis but with an increased absorption coefficient to the effect of mimicking the zone of hyperemia and inflammation. The ratio of the optical absorption coefficients between the two layers is 1:20, based off of a page in 'Photoacoustic Imaging and Spectroscopy' (edited LV Wang, published by CRC Press, page 276). I am having trouble detecting any signal, and I am simply wondering if I am using the correct contrast (1:20 ratio). This is why I have asked about any ratio you may have observed.

Sincerely,
Mason Schellenberg

From: Ida, Taiichiro <taiichiro.ida@advantest.com>
Sent: Thursday, March 15, 2018 4:10:38 PM
To: Schellenberg, Mason W. (MU-Student)
Subject: RE: Question about manuscript Titled 'Burn depth assessments by photoacoustic imaging and laser Doppler imaging'

Dear Mr. Mason Schellenberg,
I'm sorry for delaying my reply. Your concern is the PA ratio between the skin surface and hyperemia. I checked Wang's paper and understood the amplitude of PA signal from surface is about 20 times smaller than PA amplitude of hyperemia, as you mentioned. I think the PA signal of skin surface depends on the condition of skin. I had experience of clinical trial. If it looks white in the surface skin of burn patient, the PA signals was same as Wang's paper. (the surface signal is smaller than hyperemia) But the colors of some burn patient were red due to terrible inflammation, the PA signals originating from skin surface is much higher than hyperemia. In my paper I used rat burn model. Rat does not have melanin but the pigment at skin surface was observed, so the PA signal of skin surface is stronger than PA signals from the below zone of stasis. I think the PA ratio is not important for burn diagnosis but the measuring the burn depth correctly is important. Regarding as my system it was difficult to diagnose the burn patient with terrible skin surface condition. If the PA signal of skin surface was strong, the extended PA signal was observed. It was difficult to distinguish the PA

signals between form skin surface and hyperemia. I hope your system would be used for diagnosing any burn patient. If you have any questions, do not hesitate to ask me.

Best regards,
Taiichiro Ida

From Schellenberg, Mason W. (MU-Student)
<mason.schellenberg@mail.missouri.edu>
Sent: Thursday, March 15, 2018 8:07 PM
To: Ida, Taiichiro <taiichiro.ida@advantest.com>
Subject: RE: Question about manuscript Titled 'Burn depth assessments by photoacoustic imaging and laser Doppler imaging'

Dear Dr. Ida,

Thank you for this insight, it is valuable. This is not something I had considered because I have not begun working
with live tissue. Do you have any papers you could recommend to me so I could learn more about this?

Sincerely,
Mason Schellenberg

E.1 Bibliography

[1] T. Ida, H. Iwazaki, Y. Kawaguchi, S. Kawauchi, T. Ohkura, K. Iwaya, H. Tsuda, D. Saitoh, S. Sato, T. Iwai, Burn depth assessments by photoacoustic imaging and laser Doppler imaging, Wound Repair and Regeneration 24(2) (2015) 349-355.